TARGETING GLUTAMINE METABOLISM AND CD47-SIRP ALPHA SIGNALING REPROGRAMS IMMUNOSUPPRESSIVE TUMOR-ASSOCIATED MACROPHAGES RESULTING IN IMPROVED ANTI-TUMOR IMMUNITY

by
Monali Praharaj

A dissertation submitted to Johns Hopkins University in conformity with the requirements for the degree of Doctor of Philosophy

Baltimore, Maryland
March 2023

Abstract

Immune checkpoint blockade therapies have shown little or limited success in urologic cancers due to their immunologically cold nature, and this is especially true for metastatic castration-resistant prostate cancers (mCRPC). In several cases of primary, and metastatic cancers, tumor cell mass (up to ~30-50%) is comprised of M2 tumor-associated macrophages (M2-TAMs). The increased abundance of immunosuppressive M2-TAMs in diverse primary and metastatic tumors has been correlated with worse prognosis. Additionally, M2-TAMs in the tumor microenvironment (TME) of mCRPC interact with enriched reactive stroma and promote tumor growth and metastasis. The sparsity of effective interventions in urologic cancers, especially for late-stage disease, coupled with a myeloid-rich and poor lymphocyte infiltrated TME, provides the rationale for novel myeloid-targeting immunotherapies.

In Chapter 1, we have identified increased glutamine metabolism in TAMs in mCRPC patients. Targeting glutamine metabolism in rodent models of urologic cancers validated the role of myeloid cell glutamine metabolism in tumor growth. We demonstrate that profoundly reprogrammed TAMs and tumor-associated monocytes (TIMs) can mediate direct anti-tumor responses in myeloid-rich tumors with low T-cell infiltration. Additionally, for the first time, we report that glutamine antagonism in TAMs increases tumor cell phagocytosis and alters glycolysis, TCA cycle, and purine metabolism. Moreover, we also show that drug-induced glutamine inhibition in TAMs could increase inflammatory and proliferative pathways.

In Chapter 2, we identified the therapeutic benefit of targeting the CD47-SIRPα axis in urologic cancers. We demonstrate increased CD47-SIRPα signaling in prostate adenocarcinoma and renal cell carcinoma patient samples and increased concomitant Calreticulin (“eat me”) signaling. We show that targeting CD47-SIRPα causes increased

phagocytosis of prostate cancer cells by TAMs using co-culture of peripheral blood mononuclear cell (PBMC)-derived macrophages and prostate cancer cells. Additionally, we show that *in vivo* blockade of this axis strongly suppresses tumor growth and improves survival in animals. Finally, we also elucidate significant reprogramming of TAMs and increased proliferation of CD8 T cells in the absence of a CD47-SIRPα signaling.

Overall, our studies demonstrate therapeutic glutamine metabolic inhibition and blockade of CD47-SIRPα leads to extensive remodeling of TAMs consistent with improved anti-tumor responses in urologic tumors.

Thesis Advisors:

Drew Pardoll, M.D., Ph.D.

Jelani Zarif, Ph.D., M.S.

Thesis Committee Members:

Karen Sfanos, Ph.D., M.S. (designated reader)

Robert Leone, M.D.

Irving L. Weissman, M.D.

Acknowledgements

I would like to thank my mentors Dr. Drew Pardoll and Dr. Jelani Zarif, for their timely guidance, all the opportunities they have provided, and for having confidence in me all through the way. Additionally, Jelani has been the most warm and supportive mentor which has really helped me grow a lot personally, and for that I am truly thankful. I am very grateful for an incredibly supportive lab environment with some truly amazing people that I have had the opportunity to work with namely- Thomas Nirschl, Fan Shen, Debebe Theodres, Xiaoxu Wang, Alex Lee and Kenneth Adusei. Additionally, I also have had the opportunity to train and guide some amazing students like Me'Shiah Bell, Rahwa Yehdego, Alex Lee, Jonathan Skidmore and Kara Lombardo. Not only have I enjoyed working with each of them but also learnt a lot to be patient and how to be able help and nurture their scientific thinking in addition to skills. Additionally, I would like to thank my lab administrators Anna Smith and Chynna Powell Petrus who have been an amazing support throughout in lab.

I would like to thank Leone lab, Pearce lab, Denmeade lab, and the Pardoll lab members for always being there to lend a helping hand to sharing regents. I would like to thank all the collaborators for guiding us on how to go through with specific optimizations and experiments to actual fruitful discussions which have led to my increased scientific acumen. It includes Liang Zhao, Robert Leone, Laura Sena, Liz Thompson, Ada Tam, Lee Blosser, Linda Orzolek, Alyza Skaist, Liz Engle, and Amanda Wong. I would especially like to thank Dr. Barabara Slusher, Dr. Rana Rais, and Jesse Alt from their group for coordinating getting JHU083 (the pro-drug used for chapter 1) and working with me along the way.

I'd also like to thank my thesis committee members- Dr. Karen Sfanos, Dr. Robert Leone, and Dr. Irvine Weissman. Karen has been a wonderful listener and guide. I have always

found help with her whenever I needed it. Additionally, her critical review and comments have been paramount for this thesis. Bob has been just an incredible hub of knowledge and an amazing mentor to discuss through a lot of confusing data and has intellectually satisfying conversations about the field of immunometabolism. All three of them have been incredible, always driving my scientific curiosity with interesting questions while reminding and encouraging me to remember the key questions and keeping me grounded. Additionally, I would like to especially thank my former committee member Dr. Jonathan Powell. His comments and suggestions through the years and still immense interest in the work have been incredibly insightful.

Next, I would like to thank my program Director Dr. Lee martin for giving me the opportunity to be part of the program and always being there for me whenever I needed him. I have never seen anyone else as invested in my overall well-being and happiness of students and I have learnt a lot from him. He has been a true guide through some really tough interpersonal decisions and choices and always been extremely supportive through the process with the same. I couldn't be more grateful for this. Also, I'd like to thank Stacey Morgan without whom I would be lost and overwhelmed through the program. She has been truly amazing, and I am truly thankful to have her as our program coordinator. I'd also like to thank my cohort and just incredible fellow pathobiology students. Many have been a source of constant support and motivation through classes, oral examinations, and research work.

Finally, I would like to thank my family- my parents and my sister. My sister and mother are the core pillars, so I have learnt to be humble, hardworking, and always be kind to everyone and empathetic. They have been the source of constant support through this journey, without which I would not be able to complete it. Next, I would like to thank my brother-in-law, who has been a constant support without even asking. Additionally, I would like to thank all my incredible friends and extended family for all of their love and support.

Last but certainly not least, I'd would like to thank my partner Alok Singh. Alok is an incredible human being and scientist who has helped me have the most intellectually stimulating conversations and sharing the same passions I do which has always kept me going. Moreover, he has just the humblest person I have ever met which has pulled me through navigating some really challenging times.

Finally, this work was only possible due to supported grants- NCI K22CA237623, Allegheny Health Network and Bloomberg Philanthropies. The authors have no financial conflicts.

Table of Contents

List of Tables

List of Figures

List of Abbreviations

AD: Androgen deprivation

ADT: Adoptive transfer

AKT: Ak strain transforming

APCs: Antigen-presenting cells

BPTES: bis-2-(5-phenylacetamido-1,2,4-thiadiazol-2-yl) ethyl sulfide

C/EBPβ: CCAAT/enhancer-binding protein beta

CCL: C-C motif ligand

CCR: C-C chemokine receptor

CD: Cluster of differentiation

CD47: Cluster of differentiation 47

CD8: Cluster of differentiation 8

CDK12: Cyclin-dependent kinase 12

CRT: Calreticulin

CTLA-4: Cytotoxic T-lymphocyte-associated protein 4

CXCL: C-X-C motif chemokine ligand

DAMP: Damage-associated molecular patterns

DCs: Dendritic cells

DEGs: Differentially expressed genes

dMMR: Deficient mismatch repair

DON: 6-diazo-5-oxo-L-norleucine

FGAR: Phosphoribosyl-N-formylglycineamide

GLUL: Glutamate-ammonia ligase

GM-CSF: Granulocyte-macrophage colony-stimulating factor

GS: Glutamine synthase

GSEA: Gene-set enrichment analysis

HIF1: Hypoxia-inducible factor 1

HK2: Hexokinase 2

HMGB1: High mobility group box 1

HSPs: Heat-shock proteins

ICB: Immune checkpoint blockade

IDO: Indoleamine 2,3-deoxygenase

IHC: Immunohistochemistry

ISGs: Interferon-stimulated genes

JAK: Janus kinase

JHU083: (Ethyl 2-(2-Amino-4-methylpentanamido)-DON)

LC-MS/MS: Liquid chromatography–mass spectrometry

LILRB: Leukocyte immunoglobulin-like receptor B

LRP1: Low-density lipoprotein (LDL) receptor-related protein 1

MAC1: Macrophage-1 antigen

MCP-1: Monocyte chemoattractant protein-1

mCRPC: Metastatic castration-resistant prostate cancer

MDSCs: Myeloid-derived suppressor cells

MHCII: Major histocompatibility complex II

MSI: Microsatellite instability

mTORC1: Mechanistic target of rapamycin complex 1

MyD88: Myeloid differentiation primary response 88

NADPH: Nicotinamide adenine dinucleotide phosphate

NF-kB: Nuclear-factor kappa B

NK cells: Natural killer cells

NSCLC: Non-small cell lung carcinoma

OXPHOS: Oxidative phosphorylation

PAMP: Pathogen-associated molecular patterns

PBMC: Peripheral blood mononuclear cells

PCa: Prostate cancers

PD1: Programmed cell death protein1

PDAC: Pancreatic ductal adenocarcinoma

PD-L1: Programmed death-ligand 1

PGE2: Prostaglandin E2

PI3K: Phosphoinositide 3-kinases

PRRs: Pattern-recognition receptors

RCC: Renal cell carcinoma

ROS: Reactive-oxygen species

scRNAseq: Single-cell RNA sequencing

SIRPα: Signal-regulatory-protein alpha

SLAMF7: Signaling lymphocytic activation molecule family member 7

STAT: Signal transducer and activator of transcription

STC-1: Stanniocalcin 1

TAM: Tumor-associated macrophages

TCA: Tricarboxylic acid

TGI: Tumor-growth inhibition

TILs: Tumor-infiltrating lymphocytes

TIM: Tumor-infiltrating monocytes

TIRAP: Toll-interleukin 1 receptor (TIR) domain-containing adaptor protein

TLR: Toll-like receptor

TME: Tumor microenvironment

TNBC: Triple-negative breast cancer

Treg: Regulatory t cells

TRM: Tissue-resident macrophages

TSP-1: Thrombospondin 1

VEGF: Vascular endothelial growth factor

α-KG: α-ketoglutarate

Introduction

An Unmet Need for Novel Immunotherapies in Urologic Cancers

Advances in cancer immunotherapy has had significant impacts on metastatic cancer. While metastatic cancers such as melanoma, lung cancer, and renal cell carcinoma show dramatic responses to immunotherapy, prostate and urothelial carcinoma have generally failed to show any significant response (**Table 1**) [1]. Prostate cancer is the most commonly diagnosed cancer that accounts for 21% of all cancer cases in men in the U.S. Prostate cancer is also the second most common cause of cancer-related death in the U.S., accounting for 34,500 deaths in men in 2022 [2]. Despite advances in detection, screening, and therapy over the past few decades, the mortality rate due to prostate cancer remains very high [3]. The immunologically 'cold' and immunosuppressive tumor microenvironment (TME) with low mutational burden and poorly infiltrated T cells remains the key challenge for prostate cancer immunotherapy [1]. Ex vivo immune cell analysis of tumor specimens from prostate cancer patients suggests that tumor-infiltrating lymphocytes are skewed towards T-regulatory (Treg) and T helper 17 (Th17) phenotypes, which suppress autoreactive T cells and hamper anti-tumor responses [4]. The tumor-infiltrating immune cells that may contribute to prostate cancer progression include T cells, B cells, mast cells, and NK cells. For example, tumor infiltrating CD4+ T cells are associated with tumor progression and metastasis [5]. Also, infiltration of CD8+ T cells in invasive margins of prostate cancer may be related to the poor prognosis of patients [6]. Similarly, increasing TAMs in prostate cancer are associated with poor survival in prostate cancer patients [7]. More recently composition of the gut microbiota has been proposed to affect responses to chemotherapy and immunotherapy in prostate cancer patients [8].

Immune checkpoint blockade (ICB) therapies have revolutionized the treatment landscape of many cancers with durable responses in some cases. Tumor mutational burden (specifically related to mutations in mismatch repair pathway genes), the density of tumor infiltrating CD8+ T cells, and expression of immune checkpoint molecules determine the relative success of ICB therapies in traditionally categorized immunologically “hot tumors” as compared to immunologically “cold tumors” [9]. Novel immunotherapies mainly target immune tolerance via co-inhibitory checkpoints and enhance endogenous anti-tumor immune responses via various mechanisms to target malignant cells. These approaches have shown remarkable clinical activity in terms of progression-free survival and overall survival across several tumor types with fewer side effects as compared to chemotherapeutic interventions [10].

The highly immunosuppressive tumor immune microenvironment with a predominance of immunosuppressive TAMs in prostate tumors has compelled the formulation of therapies that could enhance immune infiltration by antigen-presenting cells and effector T cells [11]. Also, androgen deprivation (AD) therapy, a common therapeutic strategy in advanced prostate cancer, transiently mitigates T cell tolerance and induces T cell priming to prostatic antigens [12]. Hence, it is possible that AD therapy in combination with immunotherapy could have synergistic anti-tumor effects. Recent understanding of prostate tumor immune microenvironment fueled by a combination of single-cell transcriptomics and metabolomics approaches and the approval of drugs such as Sipuleucel-T and ICB provides a viable alternative treatment modality for mCRPC to prevalent methods such as ADT and chemotherapy [13]. Despite being immunologically ‘cold’ by definition, a subset of prostate cancer exhibits an immunogenic phenotype [14]. Indeed, a subgroup of patients with high PD-L1 tumor expression, CDK12 mutations, high tumor mutational burden, or tumors with high microsatellite instability (MSI) and mismatch repair-deficient (dMMR) have recently demonstrated excellent responses to (ICB) and their combinations with other agents [15]. Therefore, immunotherapy targeting a myeloid-rich TME remains an appealing treatment option for prostate cancer to optimize the management of this disease.

Macrophage Polarization

Macrophages are heterogeneous innate immune cell populations of myeloid lineages with a wide distribution in lymphoid and non-lymphoid tissues, wherein they play critical roles in phagocytosis, inflammation, tissue repair, and remodeling [16]. Together with dendritic cells (DCs) and B cells, macrophages represent the class of professional antigen-presenting cells (APCs), equipped to process and present peptide antigens to T cells via major histocompatibility complex II (MHCII), thus acting like a bridge between innate and adaptive immunity [17]. The enormous plasticity of macrophages allows them to acquire different phenotypes and functions primarily affected by their ontogeny and the resident tissue microenvironment [18].

Macrophage polarization is an estimate of macrophage activation at a given space and time [19]. Different polarization states of macrophages depend on the diversity of the environmental cues, duration, and kind of cytokine or chemokine exposure or effector molecules that they encounter [19]. Historically macrophage polarization states are defined as ‘classically activated’ or M1 and ‘alternatively activated’ or M2, each related to specific immune responses, among which both progression and resolution of inflammation constitute the key determinant [20]. The understanding of M1 and M2 macrophage polarizations has been primarily based on in vitro studies and utilization of knock-out (KO) mice that have often overlooked the complex microenvironment in vivo [21]. Hence, the M1/M2 paradigm fails to mimic in vivo macrophage polarization or activation states [22].

M1 Macrophage Polarization

Mackaness introduced the term macrophage activation (classical activation) in the 1960s to describe the antigen-dependent but non-specific enhanced microbicidal state of macrophages in response to secondary bacterial challenge [23]. M1 or classically activated macrophages produce a large amount of pro-inflammatory cytokines, are strongly microbicidal and tumoricidal due to the

increased production of reactive nitrogen and oxygen intermediates, mediate pathogen-resistance and promote Th1 responses [24]. Within the tumor context, M1 macrophages trap phagocytose and lyse tumor cells [25].

The stimuli for M1 macrophage polarization are classified based on their ability to induce prototypic inflammatory responses and cell-surface activation markers and differ substantially. M1 macrophages are activated by Th1 cytokines (IFN-γ, and TNF-α), immune-modulatory cytokine, GM-CSF, pathogen-associated molecular patterns (PAMPs), and damage-associated molecular patterns (DAMPs) [26]. IFN-γ is produced by innate and adaptive immune cells and is the main Th1 cytokine associated with the M1 macrophage polarization [27]. IFN-γ signals via a rapid and transient induction of Janus kinase (JAK)-signal transducer and activator of transcription (STAT) and interferon-stimulated genes (ISGs) [21]. IFN-γ activated macrophages are potent producers of pro-inflammatory cytokines (TNF and IL-6), are hyper-responsive to various stimuli (e.g., TNF, type I IFN, and pathogenic microbial motifs), show refractiveness to anti-inflammatory cytokines (IL-10, IL-4, and IL-13), and resist tolerance [27].

Microbial PAMPs initiate the innate M1 activation program that includes macrophage activation via signaling through pattern recognition receptors (PRRs). The M1 macrophage polarization-inducing PAMPs include bacterial cell wall lipopolysaccharide (LPS, a Toll-Like Receptor (TLR) 4 ligand), single-stranded RNA (TLR3 ligand), and non-methylated CpG DNA (TLR9 ligand) [28]. The best studied M1 macrophage signal, bacterial LPS, activates MyD88 and MaL/Tirap (Toll-interleukin 1 receptor domain-containing adaptor protein)-dependent production of pro-inflammatory cytokines (e.g., IFN-β, IL-12, TNF, IL-6, and IL-1β), chemokines (e.g., CCL2, CXCL10, CXCL11), MHC members, and co-stimulatory molecules [29].

DAMPs are endogenous danger molecules released from damaged or dead cells that activate macrophages by interacting with PRRs. Cytosolic or nuclear proteins such as Hight mobility group box 1 (HMGB1), IL-33, histones, heat-shock proteins (HSPs), and extracellular matrix

proteins constitute DAMPs. The common non-protein DAMPs are monosaccharides, polysaccharides, purine metabolites, ATP, uric acid, heparin sulfate, and nucleic acids [30]. Granulocyte-macrophage colony-stimulating factor (GM-CSF), produced by various cells, including macrophages and parenchyma cells, signal via JAK2/STAT5, ERK, and AKT [31]. GM-CSF causes enhanced antigen-presentation, complement- and antibody-mediated phagocytosis, microbicidal capacities, leukocyte chemotaxis, and cell adhesion. Specifically, GM-CSF induces monocytes and macrophage cytokine production of IL-6, IL-8, G-CSF, M-CSF, TNF-α, and IL-1β [32].

M1-polarized macrophages are strong producers of pro-inflammatory cytokines and augment T-cell responses via increased expression of MHC class II- and co-stimulatory molecules like CD40, CD80, and CD86. M1 macrophage-released cytokines (IL-1, IL-6, and IL-12) help mediate T helper (Th1 and Th17) cell differentiation, while specific chemokines (CXCL9, CXCL10, and CXCL11) are important Th1 cell recruiters to the inflammation sites [21].

M2 Macrophage Polarization

M2-polarized or alternatively activated macrophages are involved in parasitic, helminthic, and fungal pathogenesis [19]. In addition, their role is established during allergy, atopic diseases, fibrosis, wound healing, angiogenesis, tissue repair, remodeling, and homeostatic maintenance of adipose tissues [33]. M2-polarized macrophages are induced in response to Th2 cytokines (IL-4, IL-10, IL-13 IL-33, and TGF-β) [34]. The IL4/STAT6 signaling is the key pathway involved in M2 macrophage polarization. In addition to STAT6, other transcription factors involved in M2 polarization include IRF4, PPAR-δ, and PPARG-γ [26]. The immunosuppressive attributes of M2-polarized macrophages are due to the increased production of cytokines (IL-10 and TGF-β) and chemokines (CCL1, CCL17, CCL18, and CCL22) that are involved in the recruitment of unpolarized macrophages and their subsequent polarization into an M2 state [19]. M2

macrophages are also strong producers of IL-8, CCL2, IP-10, macrophage inflammatory protein (MIP)-1β, and CCL-5 or RANTES that are potent recruiters of neutrophils, monocytes, and T lymphocytes in an inti-inflammatory or regulatory response [35]. In addition, these macrophages express cell surface receptors such as mannose-receptor (Mrc1, CD206), scavenger receptor (CD163), C-type lectin receptor (CD209), resistin-like molecule alpha 1 (FIZZ1), dectin-1, and chitinase-like protein (Ym1/2) that are associated with immunosuppression, and tissue remodeling [36].

Tissue-Resident Macrophages (TRMs)

Earlier work of van Furth and Cohn showed that significant populations of macrophages were derived from blood monocytes, which led to the establishment of a mononuclear phagocyte system (MPS) [37]. According to the linear MPS model, ontogenically committed bone-marrow precursor cells develop into circulating blood monocytes from which tissue macrophages are derived [38]. The recruitment of circulating monocytes to the tissues occurs via blood circulation under the chemotactic gradient of monocyte chemoattractant protein-1 (MCP-1) or CCL2 via the ligation of CCR2 expressed on monocytes [39]. In addition, several cell adhesion molecules, including integrins, selectins, mucin-like glycoproteins, and the immunoglobulin superfamily, are involved in this recruitment process [40].

The concept that bone-marrow-derived circulating monocytes were the sole precursor of tissue-resident macrophages (TRMs) was later challenged due to the evidence of macrophage proliferation in tissues and the presence of macrophage populations in the yolk sac before primitive hematopoiesis [41]. More recently, fate mapping studies and single-cell transcriptomics have revealed that macrophages are derived early in embryogenesis from the yolk sac and can contribute to adult pools of TRMs [42]. Because of their embryonic origin, TRMs have a long and

deep relationship with the tissues where they are located. These mutual interactions involve locally derived factors with strong tissue specificity. Because local tissue conditions fluctuate, these macrophages are highly dynamic in nature. TRMs are heterogeneous immune cell populations that carry out tissue-specific and niche-specific functions, like homeostatic functions, cell debris clearance, tissue immune surveillance, response to infection, and resolution of inflammation [43]. The heterogeneity of TRMs results from their developmental origin, local unique niche-specific factors, inflammatory status in the tissue of residence, and the time spent in the tissues [44]. This heterogeneity is reflected in vivo as different tissue-resident macrophages exist in different tissues. These include microglia (brain), alveolar macrophages (lungs), Langerhans cells (skin), osteoclasts (bone), peritoneal macrophages (peritoneum), and adipose tissue macrophages (fat) [45].

Adhering to the historical paradigm of M1 vs. M2 polarization of macrophages, TRMs are classified as M2-like, with a fundamental role in tissue homeostasis which involves their role during the development and resolution of inflammation [22].

While in vitro M2 macrophage polarization largely depends on IL-4 and IL-13, the M2-like phenotype of TRMs depends on broader M-CSF availability in vivo [46]. M-CSF is a key macrophage survival and renewal signal that also helps in the proliferation and differentiation of myeloid cells, including monocytes, macrophages, and osteoclasts [47]. Just as IL-4 induces M2 macrophage polarization in vitro, TRMs proliferate in the presence of IL-4 [48]. Despite these similarities, TRMs have different roles, proliferation capacities, and gene expression profiles [48]. We still need to fully understand the differential regulation of M2-like and TRMs. In addition, how these macrophages are replaced and differentiated during tissue homeostasis, infection, or diseased state is not established.

Tumor-Associated Macrophages (TAMs)

The TME is a complex and dynamic ecosystem containing cells, blood vessels, and an extracellular matrix (ECM) that supports cancer progression. The dynamic reciprocal relationship between cancer cells, and components of the TME promotes tumor cell survival, local invasion, and metastasis during early tumorigenesis [49]. In response to a hypoxic and acidic condition, the TME coordinates a program that promotes angiogenesis to ensure nutrient supply and replenish oxygen. During this process, tumors are infiltrated with diverse innate and adaptive immune cell populations that perform pro- and antitumoral functions [49].

Macrophages are among the most abundant non-neoplastic and most common innate immune cells in the TME. Indeed, macrophages can account for up to 50% of tumor mass in certain cancers [50]. Based on the historical definition of macrophage polarization, anti-tumor M1-like and pro-tumor M2-like macrophages coexist within a tumor. Additionally, the opposing effects of M1- and M2-like macrophages within the TME directly impact the existing anti-tumor therapies that aim to improve anti-tumor immune responses [21]. However, during tumor progression, the TME promotes M2-like macrophages through hypoxia and expression of cytokines to support tumor growth and progression. However, while some features are shared in M1 and M2 TAMs, recent studies highlight the unique transcriptional profile distinct from either purely skewed cell type. Hence, the classical definition of M1- or M2-macrophages cannot be precisely validated for TAMs in terms of their phenotypes due to the complexity and comprehensiveness of roles and heterogeneity of TAM populations [51].

Historically, bone-marrow-derived circulating monocytes recruited to the tumor sites to promote cancer progression are TAMs. These circulating monocytes are recruited mainly under the influence of the chemokine CCL2 produced from tumor cells, which signals through CCR2 expressed on monocytes. In mice, tumor-infiltrating monocytes (TIMs) almost exclusively express high levels of Ly6C. These Ly6C^{high} monocytes continuously renew the non-proliferating TAM populations and contribute to the heterogeneity of TAMs [52]. In addition to the CCL2/CCR2 axis,

several other chemoattractants (CCL5, CCL7, CCL8, CCL18, CCL20, CXCL12) and cytokines (CSF-1, VEGF, and PDGF) may have similar redundant roles in the recruitment of monocytes to the TME [35]. Many of the chemotactic factors also act as activators of transcriptional programs that contribute to functional changes in macrophage function. CSF-1, for example, attracts monocytes and increases macrophage survival and polarizes TAMs to an immunosuppressive M2-like phenotype. In contrast to M-CSF, GM-CSF activates macrophages and reprograms them to an anti-tumoral M1-like phenotype [53]. However, TAMs can have tissue origin, as studies suggest that TAMs could originate from the yolk sac and fetal liver, as demonstrated in pancreatic cancer and glioma, suggesting the coexistence of macrophages from different origins [54]. We still do not have a complete understanding of functions driven by the multiple origins of TAMs (e.g., bone marrow-derived vs. tissue resident). Yet, macrophage populations acquire different functional states depending on the tumor type. For example, while pancreatic resident macrophages of embryonic origin locally proliferate in situ and are pro-tumoral as they promote pancreatic ductal adenocarcinoma (PDAC) progression with fibrosis-modulating functions, the impairment of circulating monocyte infiltration alone had limited impacts on tumor progression [55]. Moreover, the recruited BM-derived macrophages appear anti-tumoral and show an increased antigen-presenting phenotype. Such distinct functionalities are observed in cases of lung cancer and non-small cell lung carcinoma (NSCLC), wherein tissue-resident TAMs significantly correlated with tumor growth in vivo. At the same time, the accumulation of TAMs derived from circulating monocytes was shown to cause enhanced tumor dissemination [56]. Thus, a comprehensive understanding of TAM heterogeneity and functionality is needed to understand their precise role in cancers. Indeed, TAMs are highly heterogeneous cells with both pro-tumoral and antitumoral functions. Each population carries a unique landscape based on the tumor type, stage, and immune composition of the tumors they infiltrate.

TAMs have primarily been associated with pro-tumoral functions, including promoting tumor growth, invasion, remodeling of extracellular matrix, and crosstalk with various immune cells as well as stromal and endothelial cells. These functions can aid in tumor metastasis, progression, and chemotherapeutic resistance. Due to lineage plasticity, these TAMs have been termed M2-like and can be reprogrammed to become antitumoral by becoming more inflammatory and behaving more M1-like [57].

The features of M1-like TAMs include secretion of pro-inflammatory cytokines such as IL-12, TNF-α, and CXCL10, production of nitric oxide (NO), reactive oxygen species (ROS) and increased expression of antigen presentation-related markers such as higher MHCII, CD86, and CD80 [21].

With the advent of single-cell RNA (scRNA) sequencing, it has been possible to start deciphering the molecular connection between the diversity of TAMs and their functionality. Ma et al. highlighted from 2 pan-cancer studies at least 7 different TAM sub-populations based on their molecular and reported functional diversity. Namely, angiogenic TAMs (angio-TAMs), tissue-resident macrophage-like TAMs (RTM-TAMs), interferon-induced TAMs (IFN-TAMs), lipid-associated TAMs (LA-TAMs), immune regulatory TAMs (Reg-TAMs), inflammatory cytokine-enriched TAMs (Inflam-TAMs), and proliferating TAMs (Prolif-TAMs) [57].

Angio-TAMs, LA-TAMs, and Reg-TAMs demonstrate shown some features of M2-like TAMs, which promote tumor growth, angiogenesis, or immunosuppression. Angio-TAMs are subdivided based on the high expression of angiogenesis-promoting factors or cytokines- *VEGFA, SPP1*, *VCAN, FCN1*, and *THBS1.* Angio-TAMs were identified from colorectal carcinoma (CRC), breast carcinoma (BRCA), NSCLC, nasopharyngeal carcinoma, and PDAC [58]. Reg-TAMs have been identified in pan-cancer tissues expressing higher levels of *CX3CR1, MRC1*, and *ARG1*. These are the closest to resemble alternatively activated macrophages and have been characterized to

have immunosuppressive functions [59]. LA-TAMs, the third recently characterized immunosuppressive TAMs, have higher gene signatures of lipid-related genes like *APOE, ACP5, APOC1, TREM2*, *FABP5,* and transcription factor MAF. They are also enriched for oxidative phosphorylation pathways or lipid catabolic pathways associated with immunosuppression and tolerance in gastric cancer, CRC, hepatic carcinoma (HCC), PDAC, and BRCA patients [60]. Moreover, studies have ascertained that LA-TAMs can promote tumor progression and actively suppress anti-tumor immune responses [61].

Inflam TAMs, IFN-TAMs, and Prolif-TAMs have shown anti-tumor and pro-inflammatory features. Recruitment of other myeloid cells and lymphocytes during the tumor-associated inflammatory response has been categorized as a function of inflam-TAMs. The expression signatures of inflam-TAMs include inflammatory cytokines*, IL1B, CXCL1, CXCL2, CXCL3, CXCL8*, and *CCL3* [62]. Transcription factors like *NFKB1, REL*, and *NFE2L2* are other markers identified to characterize inflam-TAMs. They have been identified in gastric cancer, esophageal carcinoma, PDAC, and CRC [63]. IFN-TAMs are the closest to expressing M1-like markers like antigen presentation signatures, i.e., *CD86* and *MHCII*, and interferon-regulated genes like *PDL1*, *CXCL10*, and *ISG15* characterized in pan-cancer types [60]. Prolif-TAMs are another proinflammatory function categorized TAM in pan-cancer types, especially gastric, CRC, prostate, and fibrosarcoma [60]. High expression of MK167, cell cycle genes, CDK1, CDC45, and HMGB1 are used to categorize this subset. If these cells are a transient population with a quick turnover to another subtype or whether they behave as precursors remains to be determined.

Finally, RTM-TAMs resemble the resident tissue macrophage at the organ site and have a high embryonic precursor signature. For example, *MARCO*, *VSIG4*, and *FOLR2* are markers of RTM TAMs reported in hepatocellular carcinoma and liver metastasis of CRC resembling Kupffer cells [60].

TAMs directly influence the properties of both the tumor and the TME. Because of their enormous plasticity and depending on environmental cues, the subsets as mentioned above are in no way exhaustive or exclusive [57].

Additionally, the functions of TAMs come from their ability to promote immune suppression, which has profound effects on other immune cells in the TME. For example, TAMs secrete PGE2, IL-10, and TGF-β, inhibiting the cytotoxic activity of T- and NK cells [64]. TAMs play a key role in Treg recruitment via the release of CCL5, CCL20, and CCL22, while the bidirectional interaction of TAMs and Treg promotes Treg activity via secretion of immunosuppressive cytokines IL-10 and TGF- β. Indeed, the same immune-mediators produced by TAMs also inhibit the maturation of dendritic cells (DCs) [64]. M2-like TAMs are also known to starve T cells due to their activity of the arginase and indoleamine 2,3-deoxygenase (IDO) pathway [65].

Another key mechanism of immune suppression by TAMs includes direct cell-to-cell contact with other immune cells. This is achieved via the suppression of immune responses through the expression of PD-L1, CD80/86, or death receptor ligands, FasL or TRAIL, that act as agonists for inhibitory receptors, PD-1, CTLA-4, FAS, and TRAIL-R1/RII, respectively present on effector immune cells [66]. In addition, B7-H4 and VISTA have similar functions [67].

Expression of the MYC oncogene affects almost 40% of transcript fingerprints of human M2 macrophages, while it is overexpressed in human TAMs [68]. MYC is known to induce expression of the anti-phagocytic 'don't eat me signal', CD47, and immune checkpoint protein PD-L1, enabling cancer cells to evade phagocytosis and promote immune suppression by dampening the effector T cell responses [69].

TAMs exert a more direct regulatory role in promoting metastasis via their response to tumor-cell-derived WNT signals; TAMs release IL-1 that subsequently activates γδT cells to produce IL-17 that in turn activates neutrophils to a pro-metastatic state in some p53 murine mammary tumors [70].

TAM Targeting Strategies:

The evolving knowledge of crosstalk between tumor cells and the TME has helped to develop strategies against the tumors' pro-metastatic non-cancer components. The indispensable role of TAMs in tumor initiation, progression, and dissemination, and their association with poor overall survival of cancer patients, forms a strong basis for targeting TAMs in anti-tumor therapies [71]. Also, TAMs are regulated by a complex network of signals, growth factors, and molecular pathways that expose several enzymes and checkpoint proteins as potential druggable targets [71]. One of the significant clinical challenges remains to block macrophage trophic phenotypes with their immunosuppressive behaviors and enhance their activation and anti-tumoral activities [71]. Indeed, the TAM-targeted therapeutic strategies have been focused on the elimination of TAMs, impairing their infiltration and phenotype conversion of pro-tumoral M2 TAMs to an anti-tumoral M1 state. Several preclinical studies suggest that the depletion of TAMs boosts the responses of chemotherapy and immunotherapy and suppresses metastasis [72].

Recruitment of TAMs in Tumors:

Tumor-derived factors such as CSF-1, CCL2, and VEGF are essential mediators in the crosstalk between TIMs and tumor cells. Immune mediators such as CSF-1 and CCL2 are the primary recruiters of TAMs to the tumor site but also play a key role in M2-like macrophage polarization [73]. Small molecule inhibitors and antibodies targeting the CCL2/CCR2 or CSF-1/CSF-1R axis have proven effective in preventing the recruitment of monocytes and macrophages to the tumor site, thereby reducing tumor growth and dissemination [71]. Although both CCR2 inhibitors and anti-CCL2 antibodies have shown anti-tumor efficacy and reduction in metastatic spread, withdrawal of anti-CCL2 treatment has shown a much stronger infiltration of bone-marrow-derived monocytes in the tumor, subsequently enhancing lung metastasis of murine breast tumors [74]. Other signaling pathways based on chemokines involved in monocyte recruitment

(CXCL12/CXCR4) in metastatic tumor spread have been targeted either alone or in combination with ICB and have been tested in preclinical animal models and are undergoing clinical trials [72].

TAM Depletion Strategies:

In addition to macrophage recruitment, the growth factor CSF-1 is involved in the proliferation, differentiation, and survival of bone marrow-derived monocytes/macrophages. Genetic ablation of CSF-1 signaling inhibits tumor advancement and metastasis [75], which forms a strong basis for targeting CSF-1/CSF-1R signaling. RG7155 (emactuzumab), a humanized antibody specific to CSF-1R, effectively depletes macrophages in patients with several solid tumors [76]. Recently, a small molecule inhibitor of CSF-1R, PLX3397 or Pexidartinib, received FDA approval for tenosynovial giant cell tumors [77]. Following the success of Pexidartinib, several CSF-1R inhibitors (ARRY-382, PLX7486, BLZ945, and JNJ-40346527) and CSF-1R monoclonal antibodies (AMG820, IMC-CS4, cabiralizumab, MCS110, and PD-0360324) have been the subject of investigation in both preclinical and clinical settings [78] . Interestingly, depletion of TAMs by CSF-1R blockade using small molecule inhibitors has shown increased infiltration of CD8+ T cells in tumors with improved response to therapies in murine models of several solid tumors [71]. A small molecule CSF-1R inhibitor, BLZ945, upon CSF1R blockade, reprogrammed TAMs by lowering the expression of pro-tumorigenic genes and upregulation of genes involved in antigen presentation and lymphocyte activation [53]. The reshaping of TME following BLZ945 administration induces positive crosstalk among TAMs, IFN-γ -producing NK and T cells, and IL-12-producing dendritic cells, thus sustaining a network of anti-tumor responses [71].

Despite the promising results and progress in targeting recruitment and depletion of TAMs, there needs to be more efficacy observed in clinical trials for CSF1/CSF-1R or CCL2/CCR2 blockade [71]. This approach indiscriminately targets all macrophages, effectively removing the macrophages that are needed to sustain cytotoxic T-cell responses [71]. In addition, compensatory accumulation of pro-tumoral neutrophils and apparent redundancy of the

chemokine system are other challenges of this approach that limit the clinical application [71]. Before the discovery of compounds targeting the CSF-1/CSF-1R pathway, drugs that were cytotoxic to monocytes or macrophages, like Bisphosphonates and Clodronates, were tested, but their toxicity remains a concern [79]. Trabectedin, an anti-neoplastic drug, is known to induce TRAIL-dependent apoptosis in TAMs [72]. Trabectedin, an anticancer agent, selectively targets monocyte and macrophage viability through a TRAIL-caspase-8-dependent mechanism, simultaneously reducing tumor burden [80]. Trabectedin was approved by the FDA in 2015 for the treatment of patients with unresectable or metastatic liposarcoma of leiomyosarcoma [81].

Remodeling TAMs:

Therapeutic strategies aiming to remodel or reprogram TAMs primarily focus on switching pro-tumoral TAMs into M1-like anti-tumoral TAMs, a strategy that benefits from the phenotypic plasticity of TAMs [72]. TNF receptor superfamily member CD40 is expressed on macrophages, and other antigen-presenting cells play a significant role in macrophage activation. Activation of CD40 via agonists increases the production of IL-12 and IFN-γ in CD8+ T cells concomitant with increased anti-tumor activity. However, several clinical trials have reported only moderate efficacy coupled with toxicity [82].

Cancer cells evade macrophage phagocytosis by overexpressing the ‘do not eat me’ signal (CD47) presented to macrophages. Interaction of CD47 on tumor cells with the signal regulatory protein a (SIRPα) on macrophages results in tumor cell phagocytosis inhibition, hence pharmacological targeting of CD47 to restore macrophage phagocytosis remains the most targeted pathway in hematological and solid tumors [83].

The leukocyte immunoglobulin-like receptor B (LILRB) family members are negative regulators of myeloid cell activation. Antibody-mediated blockade of LILRB2 has led to the phenotypic conversion of M2-like macrophages for increased inflammatory responses [84].

Macrophage PI3Kγ acts as an important switch between immune stimulation and suppression during inflammation and cancer. PI3Kγ signaling through AKT and mTOR inhibits activation of NF-kB while stimulating C/EBPβ activation that leads to immune suppression during inflammation and tumorigenesis [85]. Specifically, activated PI3Kγ induces arginase and IL-10 expression and inhibits expression of MHC I and IL-12 as the key immune suppression mechanism. Inhibition of PI3Kγ in combination with immune-checkpoint blockade has led to cytotoxic CD8+ T cell-mediated tumor growth reduction and metastasis [85]. An oral PI3Kγ inhibitor IPI-549 has shown early promise by demonstrating tolerability, signs of efficacy, and clinical activity in phase 1/1b across solid tumor patients [86].

The renewed interest in the metabolic reprogramming of TAMs is due to the wealth of information that identifies diverse metabolic circuits which contribute to the immunosuppressive activities of TAMs. In addition to growth factors, cytokine, chemokines, and their receptors, metabolites (amino acids and lipids) in the TME also contribute to the anti- or pro-tumoral activities of TAMs. An extensive network of genetic, epigenetic changes and transcription factors determine the metabolite levels of the TME [87]. The hypoxic and nutrient-starved TME causes recruitment, metabolic rewiring, and impairment of anti-tumor phenotypes of TAMs [88].

Increased lactate production by rapidly proliferating and chiefly glycolytic tumor cells in TME cause M2-like polarization of infiltrating macrophages characterized by increased arginase 1 expression [89], leading to immune suppression phenotypes. Blocking glycolysis in tumor cells thus becomes an important strategy to increase anti-tumor responses of TAMs. However, glycolysis is fundamental for macrophage activity against tumor cells, and glucose supply is essential for generating ROS and phagocytosis [88], raising questions about the utility of blocking the glycolytic pathway. This approach largely dependents on glycolytic inhibitors such as 2-deoxy-D-glucose (2-DG) that reverse macrophage polarization but is far from specific [90]. Among lipid mediators that influence the TME, tumor-derived prostaglandin E2 (PGE2) blocks early NK cell

activation and inflammatory activation of myeloid cells and drives their immunosuppressive phenotype [91]. The altered prostaglandin pathway in several tumors is linked with poor ICB efficacy [91]. Inhibitors of murine prostaglandin G/H synthase 2 (PTGS2, also known as COX2) or antagonists of the PGE2 receptors EP1/EP2 have shown reprogramming of effector immune cells and enhance the efficacy of ICB therapies [92].

Among amino acid metabolism, tryptophan metabolism remains one of the key targets of anti-tumor therapies to modulate TAMs. IDO1 (Indoleamine 2,3-dioxygenase-1) expressed on macrophages and non-immune cells catalyzes the initial oxidation of L-tryptophan and induces the accumulation of immunosuppressive kynurenine, which not only leads to the suppression of effector T cells but also causes expansion of immunosuppressive innate and adaptive immune cells, a key mechanism of immune suppression and tumor cell immune evasion [93]. Since tryptophan is needed for the optimal functioning of T cells, tryptophan deprivation via IDO1 severely compromises their effector function. Numerous small molecule IDO1 inhibitors have been developed, of which BMD-986205, Indoximod, and PF-06840003 are currently in clinical trials [94]. However, many ongoing clinical trials using different IDO inhibitors have shown contrasting results [95]. ECHO-301/KN-252, an IDO inhibitor, was tested in combination with pembrolizumab in metastatic melanoma; however, the results were not promising. One key reason IDO inhibitors are ineffective could be the compensatory expression of similar enzymes, such as tryptophan 2,3-dioxygenase (TDO) and IDO2 [96].

Glutamine Metabolism Inhibition:

Cancer cells are highly glutamine-addicted, and increased glycolysis is a hallmark of cancer [97]. Glutamine is one of the most abundant non-essential amino acids in the bloodstream that contributes to virtually every biosynthetic pathway in cancer cells [98]. Cancer cells use glutamine as a substrate for nucleotide, nicotinamide adenine dinucleotide phosphate (NADPH), and

glutathione. In addition, cancer cells utilize glutaminolysis to utilize glutamine-derived α-ketoglutarate (α-KG) that fuels the TCA cycle for the generation of reaction intermediates needed for protein, lipid, and nucleic acid biosynthesis [99]. Glutamine metabolism thus remains a preferred metabolic inhibition strategy to remodel the TME and starve cancer cells [100].

Recent reports suggest that glutamine synthase (GS), the only enzyme responsible for de novo synthesizing glutamine, regulates the immune system by modulating M2-like macrophage polarization. Pharmacological inhibition of GS skews M2-polarized macrophages towards M1-like macrophages, characterized by reduced intracellular glutamine and increased succinate with enhanced glycolytic flux through glycolysis, which could be partially related to HIF-1α activation [101]. Interestingly, GS-inhibited macrophages have increased capacity of T cell recruitment, reduced T cell suppressive abilities, and an impaired ability to cause endothelial cell branching or cancer cell motility [101]. The vital role of glutamine metabolism in the pro-tumoral functions of TAMs was observed as genetic deletion of macrophagic GS in tumor-bearing mice promoted metastasis inhibition [101].

Tumor-infiltrating M2 TAMs and myeloid-derived suppressor cells (MDSCs) show elevated glutamine consumption. Blocking glutamine metabolism by small molecules or inhibiting glutamine synthesis resulted in decreased tumor growth by modulation of MDSCs [102].

Glutaminolysis is a prominent target in cancer therapy, and its inhibition via GLS inhibitors such as bis-2-(5-phenylacetamido-1,2,4-thiadiazol-2-yl)ethyl sulfide (BPTES) and its analogs such as CB-839, are being actively investigated in GLS-targeting studies [103]. BPTES allosterically inhibits GLS1 (the GLS isoform that is found in most primary tumors) and slows tumor growth in vivo. However, the drug requires a higher concentration in vivo and has low solubility, which poses a challenge to the physiological delivery of the drug in clinical trials [104]. Another allosteric inhibitor drug, CB-839 or Telaglenastat, has entered clinical trials for patients with advanced RCC, NSCLC, and leukemias [98]. Telaglenastat has demonstrated efficacy in treating triple-negative

breast cancer (TNBC), with a marked reduction in glutamine consumption, glutamate production, and levels of glutathione and other TCA intermediates [105].

Other than targeting a single enzyme (GS), a combination therapy that targets multiple pathways in cancers may be the most effective when two drugs induce cell death when combined but not alone. A combination therapy using BPTES (glutamine metabolism inhibitor) and Metformin (glycolysis inhibitor) resulted in an optimal tumor growth reduction [103]. Several combination therapies have been utilized for cancer treatment, in which CB-839 has been used in combination with anti-tumor drugs and ICBs [98].

Many cancer cells have upregulated levels of c-MYC-activated amino acid transporter ACST2 (or SLC1A5) for increased glutamine uptake [106]. High levels of ASCT2 are correlated with aggressive tumor growth and short survival time [107]. Also, inhibition of glutamine importers significantly slows tumor growth of human colon and lung cancers [108]. The development of blocking antibodies and antibody-drug conjugates are promising approaches to inhibiting glutamine uptake and regulating the ASCT2 transporter. MED17247 is the only ASCT2 antibody-drug conjugate currently in phase I clinical trials [98].

Using glutamine mimetics is another approach to decreasing glutamine availability [109]. Glutamine analogs such as DON (6-diazo-5-oxo-L-norleucine) and acivicin showed tumor toxicity against several tumor types but are no longer in clinical applications due to their toxicity issues [110]. DON, a substrate analog of glutamine, binds to the active site of GLS. However, lack of sensitivity and toxicity caused difficulty in progressing clinical trials [110]. Like DON, acivicin and azacerine are glutamine analogs that interrupt nucleotide synthesis by inhibiting amidotransferases [111].

A DON-based prodrug, the compound JHU083, exhibits preferential tumor delivery and is well tolerated. JHU083 causes significant tumor growth reduction in murine models of melanoma, colon cancer, lymphoma, immunotherapy-resistant triple-negative breast cancer (TNBC), and glioma [112]. The metabolic reprogramming of the TME caused by JHU083 leads to a potentiated

CD8+ T cell response, decreased recruitment of immunosuppressive MDSCs, increased immunogenic cell death, and the repolarization of MDSCs to pro-inflammatory macrophages [112]. Another DON-based prodrug, sirpiglenastat (DRP-104) is currently being tested as a single agent or combined with atezolizumab in a clinical trial in patients with advanced solid tumors [113]. Since sirpiglenastat can simultaneously target multiple glutamine-dependent pathways, its overall performance in clinical trials might be superior to that of molecules targeting only one enzyme (e.g., telaglenastat) [114].

Currently, there is a great interest in tumor metabolic status and metabolic dysregulation of cancer cell populations in the tumor. Metabolomics has contributed to our understanding of the metabolic pathways in tumors and innate and adaptive immune cell populations that collectively drive the fate of tumorigenesis [115]. However, such approaches need to be combined with strategies that identify the heterogeneity of tumor cells, TAMs, and metabolic plasticity that are critical contributors to cancer cell resistance and significant roadblocks.

Chapter 1: Glutamine antagonist JHU083 reprograms immunosuppressive tumor-associated macrophages to drive tumor immunity in urologic cancers.

Abstract

Tumor metabolism is emerging as a critical regulator of immune-mediated anti-tumor responses. Here, we report potent anti-tumor effects of glutamine antagonist (JHU083) in urologic tumors *in vivo.* We also demonstrate that JHU083-reprogrammed tumor-associated macrophages (TAMs) and tumor-infiltrating monocytes (TIMs) are crucial in mediating significant tumor growth inhibition (TGI). Using orthogonal approaches, we show that JHU083-mediated glutamine antagonism induces TNF, inflammatory, and mTORC1 signaling transcriptionally and translationally in different intra-tumoral TAMs clusters. Additionally, we report that JHU083-induced glutamine antagonism increases proliferation in tissue-resident macrophages intratumorally and in different TAM sub-clusters. Functionally, we report that JHU083-reprogrammed TAMs have increased tumor cell phagocytosis and diminished pro-angiogenic capacities. *In vivo* modulation of glutamine consumption in TAMs results in increased glycolysis, shunting of succinate flux, and simultaneous disruption in purine metabolism. Although the effect of glutamine antagonism was less profound in the tumor-infiltrating T cells for their anti-tumor activity, it promoted a stem cell-like phenotype in $CD8^+$ T cells and decreased $CD4^+$ Treg abundance. Additionally, we report a global shutdown in glutamine utilizing metabolic pathways in tumor cells, leading to reduced HIF-1α, c-MYC phosphorylation, and induction of tumor cell apoptosis, all key anti-tumoral features.

Introduction

Dysregulated cancer cell metabolism is a hallmark of cancer [116]. Cancer cells have higher glucose consumption with simultaneous lactate production, independent of oxygen availability, called the Warburg effect [117]. In addition, cancer cells have altered TCA cycle metabolism as well as augmented purine and pyrimidine metabolism, and lipid biosynthesis to meet the bioenergetic demands and cellular proliferation [118]. Cancer cells are also highly addicted to glutamine, a non-essential amino acid considered essential for cancer cell fitness. Glutamine synthesis is upregulated in different malignancies, and many tumor cells die if devoid of exogenous glutamine, suggesting an essential role of this amino acid in tumor progression [119]. Cancer cells utilize glutamine (glutaminolysis) to fuel TCA cycle via α-ketoglutarate (α-KG) for generation of reaction intermediates that feed anabolic growth via synthesis of building blocks (proteins, lipids, and nucleic acids) [117]. Cancer cells depend on glutaminase (GLS), a mitochondrial enzyme, for the conversion of glutamine to glutamate that enters the TCA cycle to produce α-KG. Also, through the process of anaplerosis, cancer cells utilize glutaminolysis to replenish α-KG, that is essential for energy metabolism [98].

Myeloid cells are one of the major components of the tumor microenvironment (TME). The ability of myeloid cells to adapt to various environmental cues is related to the dramatic metabolic remodeling that drives their development, differentiation, and activation [120]. Tumor-associated macrophages (TAMs) are highly heterogeneous macrophage populations due to their rapid adaptability into diverse phenotypic, metabolic, and functional states in response to environmental signals from the TME [120]. Conventionally while M1-like macrophages are increasingly glycolytic coupled with excess lactate secretion and NADPH, lipid, and nucleotide biosynthesis, M2-like macrophages utilize oxidative metabolism (OXPHOS) for bioenergetic demands [120]. However,

this overly simplistic description of metabolic status does not suffice for TAMs due to their plasticity and heterogeneity, although TAMs are largely biased towards an M2 phenotype [121].

In addition to playing a significant role in cancer cell proliferation, glutamine metabolism is also known to contribute to macrophage activation [101]. TAMs of both human and murine origin have elevated levels of glutamine transporters and metabolic enzymes, showing increased glutamine consumption [122]. Glutaminolysis is an important feature of alternatively activated or M2-like macrophages accompanied by fatty acid oxidation [123]. GLUL (glutamate-ammonia ligase) is upregulated in most human cancers, and it favors M2 polarization by catalyzing the conversion of glutamate to glutamine in vitro [124]. Indeed, inhibition of GLUL favors polarization of M2-like TAMs to M1-like TAMs that is accompanied by increased glycolytic flux and succinate availability, suggesting a metabolic interplay between glucose and glutamine metabolism in the regulation of TAM function [101]. Both α-KG and succinate levels determine the macrophage polarization phenotype. While a higher α-KG/succinate ratio favors M2-like macrophages, a lower α-KG/succinate ratio favors M1-like macrophages [123]. Similarly, extracellular glutamine supplementation is also known to promote M2-like macrophage polarization [101]. Moreover, genetic deletion of glutamine synthetase (GS) promotes tumor vessel pruning, vascular normalization, accumulation of cytotoxic T cells, and inhibition of metastasis, providing a critical role of glutamine metabolism in angiogenesis, immune suppression, and metastasis in the TME [101]. These observations point out the fundamental role of TAMs as one of the key players in shaping the TME and in tumor progression and provide a strong rationale for targeting glutamine metabolism in TAMs.

Prostate cancer is less glycolytic, highly lipogenic, and dependent on oxidative phosphorylation than other solid tumor types, however recent evidence suggests that prostate cancer is dependent on glutamine metabolism for growth [125]. Along the same line, GLS1 expression in prostate cancer strongly correlates with tumor stage and disease progression [126].

Indeed, therapeutic strategies for targeting glutamine metabolism in prostate carcinoma have long been investigated due to the high glutamine addiction of these tumors. The broadly active glutamine antagonist DON (6-diazo-5-oxo-L-norleucine) was used as glutamine antagonist against multiple malignancies including prostate carcinoma, but dose-limiting gastrointestinal toxicities led to the termination of its clinical development [127]. Similarly, glutamine deprivation using glutamine antimetabolite and earlier attempts to inhibit GLS were met with significant toxicities [128]. However, the renewed interest in glutamine utilization blockade in malignancies including prostate cancer has emerged due to a better understanding of cancer cell metabolism and the advent of more selective GLS inhibitors with proven safety and tolerability [129].

Despite eliciting gastrointestinal and neurotoxicity in patients, the glutamine antagonist drug, DON, showed improved tumor toxicity, therapeutic efficacy, and significant effects on improving immunotherapies [127]. Potent anti-tumor activity of DON-induced glutamine antagonism is due to inhibition of multiple glutamine-utilizing enzymes like glutaminase, multiple glutamine amidotransferase involved in nucleotide synthesis, amino acid synthesis, hexosamine production, and glutamine transporters [127].

Orally, bioavailable novel glutamine antagonist prodrug JHU083 is a derivate of DON that significantly addresses its observed toxicities and is well tolerated. JHU083 shows significant tumor growth inhibition (TGI), attenuates metastatic progression and improves animal survival in different syngeneic murine models of melanoma, colon cancer, lymphoma, immunotherapy-resistant triple-negative breast cancer (TNBC), and glioma [130]. Metabolic targeting of the TME with JHU083 has shown the tumoricidal effect on tumor cells, while a potentiated $CD8^+$ T cell response was due to the differences in metabolic plasticity of these cells. In a landmark study, Oh *et al.* demonstrated in the murine 4T1 breast cancer model decreased recruitment of immunosuppressive myeloid-derived suppressor cells (MDSCs), increased immunogenic cell death, and the repolarization of MDSCs to pro-inflammatory macrophages within the TME. This study suggests that MDSCs are the prominent cells affected by JHU083 [112]. However, a

detailed understanding of the metabolic and functional aspects of the reprogramming of intratumoral TAMs upon glutamine antagonism remains to be elucidated [112].

Herein we provide translational relevance of increased glutamine metabolism in TAMs in human metastatic castration-resistant prostate cancer (mCRPC) samples from bone metastases and evidence of efficacy of targeting glutamine metabolism in three pre-clinical murine syngeneic urologic tumor models. Using JHU083-induced glutamine antagonism in these myeloid-rich urologic tumor models, we show that JHU083 promotes a potent and direct anti-tumor effect and reprograms the TME, exploiting the differential metabolic plasticity between tumor cells, macrophages, and T cells. Additionally, we report JHU083-mediated restoration of anti-tumor immunity through myeloid-cell (TAM and tumor-infiltrating monocytes (TIMs) reprogramming that includes increased phagocytic capacity, proliferation, inflammatory signaling, blockade of purine metabolism, increased glycolysis and shunting of succinate to drive tumor-toxic inflammatory signaling.

Results

Bone Metastatic Prostate Cancer tumors have enriched glutamine utilizing enzymes in TAMs

Using single-cell RNA sequencing (scRNAseq), Kfoury et. al. characterized the bone marrow (BM) microenvironment in prostate cancer (PCa)-matched tissues (bone metastasis, involved BM, distal BM and benign BM) from 9 mCRPC patients [23]. Using this data set, we examined expression levels of key enzymes involved in glutamine utilization, synthesis, and transport, as well as enzymes involved in glycolysis [23]. In the bone metastatic tumor fraction, an increased average expression of glutamine transporter *SLC1A5* (*ASCT2*), glutamine utilizing enzymes *GLS* (Glutamine synthase), *GFPT1* (Glutamine-fructose-6-phosphate transaminase), *PPAT* (Phosphoribosyl pyrophosphate amidotransferase), *GLUL* (Glutamine synthetase) and glycolytic

enzyme *Hk2* (Hexokinase) was observed relative to the benign or distal BM fraction (**Fig 1A and B**).

Specifically, increased expression of *GLUL* and *GLS* was observed in the TAMs (*CD68*$^{+}$*, CD163*$^{+}$), TIMs (*LER*$^{+}$, *PLAUR*$^{+}$), Mono 3 (monocyte cluster 3) (*MNDA*$^{+}$*, CTSA*$^{+}$), osteoclasts (*MMP9*$^{+}$*, SPP1*$^{+}$), and endothelial cells (*GNG11*$^{+}$*, IFI27*$^{+}$) in the tumor or involved BM fraction relative to the benign or distal BM fractions, suggesting increased glutamine metabolism in these cell types (**Fig 1B and C**). Increased *GLUL* expression was found in TAM and Mono 3 clusters in the tumor BM relative to distal, benign, and involved fractions (**Fig 1C and D**). Also, *GLS* expression was higher in the TAM cluster of the tumor fraction, suggesting predominant glutamine metabolism activity in these tumor-infiltrating myeloid cells. We also found increased *GLS* expression in the Mono 3 cluster of involved BM relative to the distal, benign, or tumor fractions (**Fig 1C and D**). Together these results demonstrate an abundance of key glutamine metabolizing enzymes in the immunosuppressive, pro-metastatic TAM population in metastatic PCa tumors. It also highlights the rationale of the multifaceted therapeutic benefit of utilizing a glutamine mimic to inhibit diverse glutamine utilizing enzymes to alter these cells for increased anti-tumor response metabolically [127].

Glutamine antagonism with JHU083 shows potent anti-tumor activities in urologic tumors

We employed two established syngeneic, heterotopic, immunocompetent mouse models to investigate whether JHU083-induced glutamine antagonism enhances host anti-tumor immunity in urologic tumors. As shown in **Fig 2A and B**, subcutaneous prostate and urothelial tumors developed by implanting B6CaP (CD45^{-} mouse prostate carcinoma) or MB49 (carcinogen-induced male urothelial carcinoma) cells, respectively [131]. Following the growth of palpable tumors (200-500 mm^3), tumor-bearing animals were randomized into two cohorts: placebo or oral JHU083 (~1mg/kg DON equivalent) for 5-9 days, followed by a lower dose of (0.3 mg/kg DON equivalent) [112]. A significant TGI and tumor weight reduction was observed in both tumors

following JHU083 monotherapy without any consequential weight loss (**Fig 2C-F**). We further validated the JHU083-mediated robust TGI in another aggressive syngeneic murine prostate tumor carcinoma model RM-1 (**Fig 2G**). Together, these results show a potent anti-tumor activity of JHU083 monotherapy as evidenced by robust inhibition of growth of urologic tumors without significant host toxicity.

Anti-tumor activity of JHU083 in urologic tumors is only partially dependent on T cells

We next set out to investigate the underlying immune-effector mechanisms of the anti-tumor efficacy of JHU083 in urologic tumors. To this end, we assessed if an adaptive immune response is vital for JHU083-mediated TGI by using anti-CD8β and anti-CD4 specific depletion and isotype control antibodies for 3 days before tumor engraftment to ensure T cell depletions (**Fig 3A**). Once tumors became palpable (200-500 mm^3), the animals were randomized and treated with JHU083 as described above (**Fig 2A-B**).

We observed aggressive tumor growth following antibody-mediated $CD8^+$ T cell depletion in MB49 tumor-bearing animals (**Fig 3B**), a phenotype not observed in B6CaP tumors (**Fig 3C**). However, in both tumor models, JHU083 treatment caused a robust TGI despite $CD8^+$ T cell depletion (**Fig 3B and C**), suggesting that the anti-tumor activity of JHU083 is only partially dependent on $CD8^+$ T cells in both tumor models. Importantly, JHU083-treated animals bearing MB49 or B6CaP tumors survived longer than untreated controls (**Fig 3B and C**), suggesting less prominent anti-tumor effects mediated by $CD8^+$ T cells upon JHU083 treatment.

Next, we investigated the role of $CD4^+$ T cells in both models of urologic cancer. Following a similar strategy adopted in the $CD8^+$ T cell depletion study, we observed that the depletion of $CD4^+$ T cells resulted in increased tumor growth in B6CaP tumors (**Fig 3E**). At the same time, there was no evident change in the MB49 tumor growth (**Fig 3D**), suggesting that $CD4^+$ T cells do not restrict MB49 tumor growth. Like the $CD8^+$ T cell depletion, the JHU083 treatment maintained anti-tumor efficacy even after $CD4^+$ T cell depletion was achieved. Additionally, even

though JHU083-treated animals survived longer compared to isotype control-treated animals, no significant changes were observed between JHU083 treatment alone relative to JHU083 treatment in $CD4^+$ T cell-depleted tumors (**Fig 3E and D**). Altogether, these results suggest that the efficacy of JHU083 in these urologic tumor models is less dependent on $CD4^+$ T cells and $CD8^+$ T cells.

JHU083 inhibits tumor growth in urologic tumors in a myeloid-dependent manner

Owing to the increased abundance of glutamine metabolizing enzymes utilized in the immune-suppressive TAM population in bone metastatic PCa tumors (**Fig 1C**), we next investigated the role of these myeloid cells in anti-tumor efficacy of JHU083 in urologic tumors.

To do so, we first performed an adoptive transfer (ADT) of both TAMs and TIMs, as previously described by Kaneda *et al.* (**Fig 4A**) [85]. Briefly, live FACS-sorted TAMs ($CD45^+$ $CD3^-$ $Ly6G^-$ $CD11b^+$ $F4.80^+$) from JHU083-treated or vehicle-treated MB49 tumors were mixed with *in vitro* cultured live MB49 cells in a 1:1 ratio and were subsequently implanted in the flanks of syngeneic recipient C57BL/6J mice. A significant delay in MB49 tumor progression was observed in the animals that received ADT JHU083-treated TAMs mixed with MB49 cells compared to those tumors that developed from vehicle-treated TAMs mixed with MB49 cells (**Fig 4B**). An even greater TGI was observed in tumors that originated using a mix of JHU083-treated TAMs and MB49 cells, and the animals subsequently received JHU083 treatment (~0.3 mg/kg equivalent of DON) (**Fig 4B**). Similarly, a stronger TGI was observed in MB49 tumors developed using a mix of vehicle-treated TAMs and MB49 cells following JHU083 treatment as compared to no treatment after ADT. No significant change in tumor volume was observed in ADT MB49 tumors and non-ADT MB49 tumors in the absence of JHU083 therapy. Together, these results support the antitumoral role of JHU083-treated TAMs. This, in turn, could be due to phenotypic changes in TAMs induced by JHU083-mediated reprogramming of TAMs to an anti-tumor state within the TME.

Next, we investigated the contribution of TIMs (live $CD45^+$ $CD11b^+$ $CD3^-$ $Ly6G^-$ $Ly6C^{high}$) in the TGI following JHU083 treatment. Briefly, JHU083-treated or vehicle-treated MB49 tumor-derived TIMs were mixed with live MB49 cells in a 1:1 ratio (**Fig 4A**) and implanted in the syngeneic recipient C57BL/6J mice, followed by tumor growth kinetics measurement. A delayed TGI was observed in MB49 tumors originating from JHU083-treated TIMs mixed with MB49 cells over MB49 tumors growing from vehicle-treated TIMs mixed with MB49 cells (**Fig 4C**).

Altogether these results demonstrate that JHU083-mediated TGI in urologic tumors is chiefly mediated via TAMs and TIMs. This phenotype was likely contributed via JHU083-induced functional reprogramming of TAMs and TIMs, thus rendering them strongly tumor-reactive for a prolonged duration. The contribution of $CD4^+$ T cells and $CD8^+$ T cells appears minimally and possibly secondary in these immunogenic urologic tumors.

JHU083 reprograms immunosuppressive TAMs and TIMs in the TME to become more inflammatory

We next set out to understand the transcriptional responses in TAMs and TIMs in the prostate cancer TME in response to JHU083-mediated glutamine antagonism. To this end, we adopted two orthogonal approaches of utilizing 10x Genomics-based single-cell RNA sequencing (scRNAseq) at day 7 post-JHU083 treatment (early time point) and bulk RNA sequencing of FACS sorted TAMs at day 14 post-treatment (late time point) in the B6CaP tumor-bearing mice (**Fig 5A and B**). Briefly, JHU083-treated or control B6CaP tumors were harvested and sorted for $CD45^+$ immune cells and $CD45^-$ tumor/stromal fractions (n=3/group) at an early time-point (7 days post-JHU083 treatment) and were subjected to the library preparation and RNA sequencing. For bulk-RNA sequencing, we used live FACS-sorted TAMs (live $CD45^+$ $CD3^-$ $Ly6G^-$ $F4.80^+$ $CD11b^+$) from B6CaP tumors (n=6/group) (**Fig 5B**).

At the early time point, using scRNAseq, we identified 9 different immune cell clusters within the $CD45^+$ fraction that were homogenously distributed across all samples based on the expression

of well-defined canonical markers (**Fig 5C**). Based on the UMAP and density plot, we noticed a shift in the density of macrophages (*Adgre1*$^{+}$ *Mrc1*$^{+}$ *Itgam*$^{+}$*)* after JHU083 treatment (**Fig 5D**). Next, we investigated macrophage/monocyte clusters and identified a total of 10 TAM clusters and 1 TIM (*Ccr2*$^{+}$ *Ly6c2*$^{+}$ *Cd44*$^{+}$) cluster. Within the TAM clusters we further identified inflammatory TAMs (Inflam_TAM; *S100a6*$^{+}$ *S100a4*$^{+}$ *S100a11*$^{+}$), Proliferating TAMs (Prolif_TAM; *Top2a*$^{+}$ *Pclaf*$^{+}$ *Diaph3*$^{+}$), glycolytic TAMs (Glycolytic_TAM; *Slc2a1*$^{+}$ *Tpi1*$^{+}$ *Gpr137b*$^{+}$), Type I IFN-responsive TAMs (IFN_TAM1 (*Ifit2*$^{+}$ *Isg15*$^{+}$ *Rsad2)*$^{+}$ and IFN_TAM2 (*Iigp1*$^{+}$ *Gbp2*$^{+}$ *Ifi47*$^{+}$) and 5 other TAM clusters named TAM1 (*Cd83*$^{+}$ *Sash1*$^{+}$ *Slc9a9*$^{+}$), TAM2 (*Ccnb2*$^{+}$ *Birc5*$^{+}$ *Cenpa*$^{+}$), TAM3 (*Ophn1*$^{+}$ *Itm2b*$^{+}$ *Fmd4b*$^{+}$), TAM4 (*Nup210l*$^{+}$ *Pde4c*$^{+}$ *Pdpk1*$^{+}$) and TAM5 (*Tmsb4x*$^{+}$ *Cdk8*$^{+}$ *Rplp1*$^{+}$) (**Fig 5E**). After JHU083 treatment early on, we observed an increased density of TAM1, TAM2, TAM4, TAM5, and proliferative TAMs and a decrease in TIMs and Inflammatory TAMs (**Fig 6A and B**).

To understand which of these clusters likely expand at a later time point to drive the TGI caused by JHU083-treatment, we systematically compared with a scoring matrix (details in methods) for each of the macrophage and monocyte clusters identified in scRNAseq analysis with the FACS-sorted, bulk-RNA sequenced TAMs (live CD45^{+} CD3^{-} Ly6G^{-} F4.80^{+}CD11b^{+}, n=6/group) from B6CaP tumors post-JHU083 treatment. Briefly, each of the cell clusters (day 7, scRNAseq) was scored based on agreement with differentially expressed genes (DEGs) identified in the bulk RNA-seq experiment (day 14) (see methods). This analysis identified TAM2, TIM, TAM1, and Prolif_TAM as putative populations that expand to dominate the transcriptional changes observed at day 14 (**Fig 6C and D**).

Based on this analysis, the proportion of four TAM clusters: TAM2, Prolif_TAMs, TAM1, and TAM4 at an early and late time point were increased after JHU083 treatment in B6CaP tumors (**Fig 6A-D**). Inflammatory TAMs and TIMs showed a decreased transcriptomic signature at an early time point but increased at a late time point, eluting to the time-kinetic influx of these populations post JHU083 treatment (**Fig 6A-D**).

Next, to understand the differential pathway regulations in response to JHU083 treatment, we performed GSEA pathway analysis in the DEGs in all the individual macrophage clusters from scRNAseq and bulk RNA seq DEGs. We identified four hallmark pathways enriched in DEGs following JHU083 treatment, namely TNFA signaling via NF-kB, inflammatory response, mitotic spindle, and G2M checkpoint in each of the top scoring TAM clusters, i.e., TAM2, TAM1, and proliferative TAM clusters (**Fig 7A).** We found an enrichment of these TNFA signaling via NF-kB, inflammatory response, mitotic spindle, and G2M checkpoint identified pathways in bulk RNA-seq-based identified DEGs in JHU083 treated TAMs. Additionally, we also found enrichment of hallmark mTORC1 signaling in the bulk RNA seq identified DEGs in JHU083 treated TAMs **(Fig 7B)**.

Alternatively, a manual examination of top DEGs from macrophages in both experiments reveals significant upregulation of key inflammatory genes, including interleukins (*Il1a, Il1b)*, myeloid chemoattractant (*Cxcl1),* inflammatory lectin type innate-sensing receptors (*Clec4e* and *Olr1*) and inflammasome *(Nlrp3*) **(Fig 8A-C)**.

Taken together, using two unbiased approaches, we identify TAM sub-populations that showed upregulation of hallmark TNF signaling and inflammatory pathways and an increased proportion of proliferative TAMs following JHU083 treatment.

Next, for orthogonal validation of inflammatory reprogramming of TAMs (live $CD45^+$ $Ly6C^-$ $Ly6G^-$ $F4.80^+$) and TIMs (live $CD45^+$ $CD11b^+$ $Ly6C^{hi}$) in both tumor models, we investigated the differential expression of canonical markers of myeloid-reprogramming or inflammation **(Fig 9A)**. To this end, we first investigated whether JHU083 treatment caused changes in cell proportion in TAMs or infiltration of TIMs. Using flow-cytometry, we found that the percentage of $F4.80^+$ TAMs (live $CD45^+$ $Ly6C^-$ $Ly6G^-$ $F4.80^+$) decreased, while the percentage of $CD11b^+$ myeloid cells (live $CD45^+$ $Ly6C^-$ $Ly6G^-CD11b^+$) and TIMs (live $CD45^+$ $CD11b^+$ $Ly6G^-$ $Ly6^{(hi)}$) increased at a late time point (day 14) in B6CaP tumors after JHU083 treatment. Orthogonal validation of $F4.80^+$ and $CD11b^+$ tissue area in B6CaP tumors by immunohistochemistry (IHC) showed a similar change

(Fig 9B-E). Concurrently, a similar increase in the percent of both $CD11b^{+}$ myeloid cells and $Ly6C^{(hi)}$ TIMs was observed **(Fig 9F)** in the MB49 tumors following JHU083 therapy. Since there was discrepancy between B6CaP vs. MB49 in terms of percentage TAM levels after JHU083 treatment, we investigated whether JHU083-induced changes were related to the intra-tumoral abundance in M1 (live $CD45^{+}$ $Ly6C^{-}$ $Ly6G^{-}$ $F4.80^{+}$ $MHCII^{+}$ $CD86^{+}$) or M2 (Live $CD45^{+}$ $Ly6C^{-}$ $Ly6G^{-}$ $F4.80^{+}$ $CD206^{+}$) TAMs in both models. After JHU083 treatment, we found an increase in M2 surface markers ($CD206^{+}$) and no marked increase in canonical M1 surface markers ($CD86^{+}$ $MHCII^{+}$) in B6CaP TAMs as previously reported by Oh *et al.* in 4T1 murine tumors indicating the tumor model- specific differences **(Fig 9B-E)**.

Finally, to understand if reprogramming by functional cytokine signaling occurs after JHU083 treatment, we used a flow cytometry-based approach to validate TNF levels by performing intracellular staining in TAMs (live $CD45^{+}$ $Ly6C^{-}Ly6G^{-}$ $F4.80^{+}$) and TIMs (live $CD45^{+}$ $CD11b^{+}$ $Ly6C^{hi}$) in B6CaP and MB49 tumors. Interestingly, the % TNF^{+} cells and the expression increased in TAMs (both in M1 or M2 sub-populations) and in TIMs after JHU083 treatment in B6CaP and MB49 tumors **(Fig 9 D and F)**.

Overall, using different approaches in different sub-clusters/ populations of TAMs and TIMs by both transcriptomics and flow cytometry-based approaches, JHU083 treatment increased TNF signaling and overall inflammatory signaling, which was consistent with the previously reported findings in the 4T1 model of breast cancer [112].

JHU083 conditions a fraction of tumor-resident TAMs to induce proliferation

Using GSEA analysis **(Fig 7)**, we observed enrichment of hallmark signaling pathway genes involved in proliferation (Mitotic spindle, G2M checkpoint) after JHU083 treatment in different TAM clusters (proliferative TAM, TAM 1, TAM 2, TAM 4, TAM 5, inflammatory TAM, IFN TAM1, and glycolytic TAM) identified in the scRNA seq analysis at an early time point as well as in the bulk-RNA sequencing dataset at a later time point. The proliferative TAM cluster was also enriched in

cell-cycle genes corresponding to G2M transition genes **(Fig 10A)**. This led us to investigate if proliferating (Ki-67^{+}) TAMs were differentially changed after JHU083 treatment using flow cytometry-based tumor immune infiltrate profiling. Indeed, JHU083 treatment increased the percentage of Ki-67^{+} TAMs (Live CD45^{+} Ly6C^{-} Ly6G^{-} F4.80^{+}) in the B6CaP TME specifically in CD206 co-expressing TAMs (Live CD45^{+} Ly6C^{-} Ly6G^{-}F4.80^{+} CD206^{+}) **(Fig 10B)**.

As GSEA analysis elucidated a proliferative TAMs cluster and proliferative pathways enriched at early and late time points respectively after JHU083 treatment, we investigated the ontogeny between the TIMs and the proliferative TAMs. To this end, we performed an RNA velocity analysis (ratio of the spliced to unspliced RNA transcripts) to predict transcriptional trajectories of each cell based on the ratios of their spliced and unspliced RNA transcripts [132], where the root cells are the undifferentiated cells and, the developmental endpoints are the differentiated cells connected via arrows pointing to the likely developmental paths [133]. Using this analysis, we determined that the proliferative TAMs were developmentally unrelated to the infiltrating monocyte fraction in the B6CaP TME **(Fig 10C)**. Previous studies have also suggested that peripheral bone marrow-derived monocytes infiltrate tissue and lose their proliferative potential during the final stages of monopoiesis [134].

Together, the results suggest that JHU083 can induce changes to the cell cycle and proliferation in different subpopulations of TAMs and a sub-cluster in TAMs enriched in proliferative signatures. Additionally, the RNA velocity analysis suggests that the proliferative TAM sub-cluster might be a resident macrophage population in the tumors that were phenotypically reprogrammed following JHU083 treatment that led to induced proliferation, the mechanism of which remains to be uncovered.

JHU083 promotes phagocytosis and decreases angiogenesis in the TME

Therapeutic remodeling of TAMs to enhance tumor cell phagocytosis remains an exciting avenue to improve their anti-tumor activity [72]. Similarly, the pro-angiogenic properties of TAMs also

remain an important target of myeloid cell-specific immunotherapies in solid tumors. Indeed, metabolic rewiring of macrophages via targeting glutamine synthetase (GS) previously showed decreased angiogenesis [101]. Here, we investigated phagocytosis and angiogenesis in the urologic tumor models to understand the functional implication of JHU083-mediated glutamine metabolic inhibition on intra-tumoral TAMs.

To this end, engineered RFP^+ MB49 cells and wild-type (RFP^-) MB49 cells were used to generate tumors that displayed uniform growth kinetics **(Fig 11A)**. JHU083 treatment of animals bearing either RFP^+ or RFP^- MB49 tumors caused statistically similar tumor regression over control that was confirmed by tumor volume measurements and in vivo imaging for luciferase intensity **(Fig 11A and B)**. After JHU083 treatment, the TAMs (live $CD45^+$ $Ly6G^-$ $Ly6C^-$ $F4.80^+$) showed augmented levels of *in vivo* phagocytosis of tumor cells relative to non-treated controls **(Fig 11C-E)**. Importantly, this increased phagocytosis was observed in both $CD206^+$ M2 TAMs and $CD86^+$ $MHCII^+$ M1 TAMs **(Fig 11C and E)**. In addition, we generated an RFP^+ RM1 tumor model to test the tumor cell phagocytosis in a prostate adenocarcinoma murine model. Consistently, augmented levels of phagocytosis of RM1 cells by TAMs was observed after JHU083 treatment **(Fig 11F and G)**, confirming it to be a consistent phenotypic response.

We further investigated whether JHU083-induced an increase in phagocytosis in intra-tumoral TAMs due to increased tumor cell apoptosis or due to a direct effect on increasing the phagocytic potential. To tease this out, we treated human monocyte-derived macrophages (HMDMs) [135] with 1-5 mM active drug DON either during the differentiation phase (D1-5) and/or during the polarization phase (D5-9). Following 9 days of DON treatment HMDMs showed enhanced phagocytosis of the CFSE-labeled PC3 cells compared to untreated control (in proficient glutamine media) when co-cultured together **(Fig 12A)**. This result suggests that glutamine metabolism in differentiated and polarized macrophages immediately augments their phagocytic activity **(Fig 12B and C)**. This phenotype was further supported when we examined the phagocytosis gene scores within the scRNAseq dataset in all TAM clusters. Specifically, TAM1,

TAM2, Inflam_TAM, and Prolif_TAM showed an enriched UCell score for phagocytosis genes after JHU083 treatment **(Fig 12D)**. Moreover, *Myo1e,* a key late-stage phagocytic force generating myosin-II gene [136], was highly expressed in TAMs of JHU083-treated B6CaP tumors **(Fig 12E)**. Altogether, these results suggest that targeting glutamine metabolism directly increases the phagocytic activity of TAMs against tumor cells.

Active drug DON inhibits glutamine synthetase (GS) activity [137], a pro-angiogenic enzyme known to promote metastasis [101]. Hence, we sought to determine the effect of DON and JHU083 treatment on angiogenesis in the TME. To understand tumor angiogenesis, we performed immunohistochemistry (IHC) for CD31 (vascular differentiation marker) in B6CaP and MB49 tumors. After JHU083 treatment, we observed that the percent of tumor tissue area stained for CD31 decreased significantly in tumors from three independent experiments excluding the necrotic regions in B6CaP and MB49 tumors **(Fig 13A and B)**. These results suggest that glutamine blockade in TAMs using metabolic inhibition results in augmented phagocytic capacities and diminished tumor angiogenesis, two essential functional tumor control mechanisms by myeloid cells.

JHU083 induces parallel metabolic changes in glycolysis, purine metabolism, and succinate in TAMs

DON-mediated glutamine antagonism has broad-ranging effects on glutamine-consuming enzymes in multiple metabolic pathways in addition to glutaminolysis [127]. Previous reports suggest divergent metabolic reprogramming in T cells relative to cancer cells in the TME due to the differential effects of glutamine inhibition [101]. Since we found that JHU083-mediated glutamine metabolism inhibition led to tumor suppression concomitant with macrophage (TAM) polarization shifts, we hypothesized that blocking glutamine metabolism would significantly affect the metabolic milieu of both the TME and TAMs.

We first investigated the metabolic phenotypes in B6CaP intra-tumoral TAMs and TIMs using the evaluation of surface and intracellular expression of surrogate markers using flow cytometry. We did not see significant changes in the relative abundance of TAMs expressing mitochondrial proteins voltage-dependent anion channel 1 (VDAC1) (mitochondrial mass), TOMM20 (OXPHOS- oxidative phosphorylation), and carnitine palmitoyl- transferase 1a(CPT1a) (fatty acid oxidation) in JHU083-treated tumors over control **(Supplementary Fig 4A)**. However, a marked increase in GLUT1 (glucose transporter) and HKII (glycolysis) was found in TAMs and TIMs following JHU083 treatment **(Fig 14A and B)**. The elevated levels of GLUT1 and HK2 were most significant in $CD86^{+}$ $MHCII^{+}$ M1 TAMs while only a trend (for their elevated levels) was seen in $CD206^{+}$ M2 TAMs **(Fig 14A)**. Indeed, GSEA analysis of DEGs in bulk RNAseq dataset of FACS-sorted TAMs from JHU083-treated B6CaP tumors earlier revealed significant enrichment of glycolytic pathway genes **(Fig 14C and D)**. Additionally, mTORC1, as a key regulator of glycolysis [138], was found upregulated in JHU083-treated TAMs relative to control **(Fig 7B)**.

Next, we investigated the direct outcome of the transcriptional and translational alterations on the metabolome of TAMs following JHU083 treatment. The metabolic discrepancy between the TAMs in the TME, as opposed to the ex-vivo, generated, homogenous macrophage populations, could be due to the highly complex milieu of the TME [139]. This prompted us to modify and optimize the rapid digestion, sorting, and tumor sample processing protocol [140] for TAMs in our effort to understand the differential intra-tumoral metabolite levels after JHU083 treatment **(Fig 15A)**.

Using an LC-MS/MS-based targeted metabolomic approach, we quantified the relative abundance of 156 key metabolites in FACS-sorted TAMs ($CD45^{+}$ $CD3^{-}$ $Ly6G^{-}$ $CD11b^{+}$ $F4.80^{+}$) from B6CaP tumors. Control (n=3 animals) and JHU083 treated (n=3 animals) TAMs were used for metabolic quantification **(Fig 15A and B)**. Notably, we discovered stalled purine nucleotide metabolism with an increase in Phosphoribosyl-N-formylglycineamide (FGAR) and guanosine and a decrease in cADP-ribose in JHU083-treated TAMs **(Fig 15C and D)**. As reported recently,

a novel glutamine pro-drug, DRP-104 (a derivative of DON), causes intratumoral purine nucleotide metabolic inhibition together with affecting glutaminolysis [113]. Similarly, JHU083 appears to induce inhibition of purine nucleotide metabolism in the TME.

Due to the technical challenges in recovering and missing the peaks for lost metabolites in a targeted metabolomics approach, we had limited success quantifying glycolysis or TCA cycle metabolites. We overcame this challenge by further optimizing the protocol and performed an in vivo tracing of [U-^{13}C] glucose in the rapid-sorted TAMs (CD45^{+} CD3^{-}Ly6G^{-} CD11b^{+} F4.80^{+}) [141] from B6CaP tumors to understand the effect of JHU083 on glycolysis and TCA cycle.

Using the in vivo [U-^{13}] glucose tracing metabolomic approach, we quantified glucose carbons entering the TCA cycle (citrate, a-ketoglutarate, succinate, fumarate, malate), amino acids (aspartic acid, glutamine, and glutamate), and glycolytic intermediates (lactate and pyruvate) as well as their relative abundances in control and JHU083 treated B6CaP TAMs. Strikingly, we observed decreased glucose carbons in succinate and an elevated level of glucose carbons in fumarate in JHU083-treated TAMs relative to control TAMs **(Fig 16A and C)**. To further understand if succinate levels get impacted by this decreased glucose carbon flux, we investigated the relative abundance of all TCA cycle metabolites.

Interestingly, we found a decreased abundance of succinate and α-ketoglutarate (α-KG) in TAMs upon JHU083-mediated glutamine blockade, suggesting a divergent metabolic response likely affecting TCA cycle intermediates **(Fig 16B)**.

Our results indicate that a disrupted TCA cycle, as previously reported in homogenous ex vivo inflammatory M1 macrophages with succinate, either converting rapidly to fumarate or shunting towards HIF1-α to induce IL-1β signaling [142]**.** To understand this regulation, we investigated TCA cycle enzymes and inflammatory cytokine transcripts in all TAMs (*Adgre1*$^{+}$ *Mrc1*$^{+}$ *Itgam*$^{+}$) from scRNA sequencing **(Fig 16D)**. Indeed, we observed increased succinate dehydrogenase subunit b (*Sdhb*) and *Il1b* transcripts in B6CaP-TAMs following JHU083 treatment **(Fig 16D)**. Moreover, bulk RNA sequencing of FACS-sorted B6caP-derived TAMs showed a highly enriched

score for signaling by interleukin pathway following JHU083-treatment **(Fig 16E)**, suggesting increased inflammation as a direct consequence of JHU083-induced divergent metabolic reshuffling in TAMs.

In conclusion, these results indicate that JHU083 contributes to intra-tumoral metabolic plasticity in TAMs, induces glycolysis in prostate carcinoma by fueling a broken/disrupted TCA cycle which in turn might be partly responsible for inducing inflammatory signaling. In parallel, glutamine antagonism also affects purine nucleotide metabolism in TAMs in the TME.

JHU083 affects tumor cell metabolism and induces cell death in urologic tumors

Glutamine is the key carbon and nitrogen source for energy production, nucleotide, and amino acid synthesis [143]. Previously, Leone et al. showed that JHU083-mediated glutamine blockade results in suppressed oxidative and glycolytic metabolism in cancer cells resulting in decreased hypoxia and nutrient depletion; however, this remains to be elucidated in myeloid-rich urologic tumors [141]. To this end, we investigated the effects of glutamine antagonism on the growth and metabolism of tumor cells in both B6CaP and MB49 tumors.

First, we performed western blot analyses of $CD45^-$ tumor/stromal whole cell lysates from MB49 and B6CaP tumors for key glutamine-utilizing enzymes following JHU083 treatment. JHU083 treatment led to suppressed ASCT2 (a major glutamine transporter), glutaminase1 (GLS1), KGA isoform, and glutaminase 2 (GLS2) **(Fig 17A)**. While we didn't observe a significant difference in the whole cell lysate from $CD45^-$ fraction in MB49 tumors, we here report a reduced surface GLUT1 expression in the $CD45^-$ cells of B6CaP tumors using flow cytometry **(Fig 17A and B)**.

Knowing that the impact of blocking glutamine in urologic tumor cells influences glycolysis, we next used a targeted metabolomic screen for whole B6CaP tumors **(Fig 17C)**. A total of 218 tumor metabolites were quantified, of which 23 showed differential modulation ($P<0.01$) between JHU083-treated vs. control B6CaP tumors **(Fig 17D and E)** that were subjected to metabolic

pathway analysis **(Fig 17F)**. Metabolic pathway analysis unveiled severely reduced nucleotide metabolism metabolites (xanthosine, CMP, deoxyuridine, dUMP, dCDP, CDP, Thymine, UDP) **(Fig 17F)**. Additionally, JHU083-mediated targeting glutamine metabolism changed metabolite levels resulting in impaired amino acid metabolism, one-carbon metabolism, glycolysis, hexosamine pathway, and TCA cycle metabolism **(Fig 17E)**.

To better understand the net result of the impaired metabolism in tumor cells, we used LC-MS-based absolute quantification of intra-tumoral glucose, glutamine, glutamate, and FGAR in both MB49 and B6CaP tumors. We observed an accumulation of increased glutamine, glucose, and FGAR **(Fig 17G)**.

Since JHU083 is known to affect c-MYC and HIF-1α signaling [141], we investigated c-MYC and HIF-expression levels in $CD45^-$ enriched fractions from MB49 tumors **(Fig 18A and B)**. While we did not observe any change in total c-MYC levels after JHU083 treatment, a significant decrease in phosphorylated c-MYC (both T58 and S62) and HIF-1α was observed.

These results suggested a global metabolic shutdown in urologic tumor cells prompting us to investigate possible effects on tumor cell viability. We found a dose-dependent reduction in MB49 cell viability **(Fig. 18C)** confirmed by enhanced cleaved-caspase-3 levels seen in tumor/stromal ($CD45^-$) cells from JHU083 treated MB49 tumors **(Fig. 18D)**.

Together, these results suggest a profound anti-tumor effect of JHU083 that impairs tumor cell metabolism leading to reduced proliferation and survival in the TME of urologic tumors.

JHU083 induces long-lived T cell markers and affects immunosuppressive Tregs in the TME

JHU083-mediated glutamine antagonism promotes anti-tumor immunity by conditioning tumor-infiltrating lymphocytes (TILs) towards a long-lived, memory-like phenotype that is highly proliferative, markedly activated, and capable of enhanced effector function in the TME [141].

While we observed only partial $CD8^+$ and $CD4^+$ T-cell dependence in JHU083-mediated anti-tumor immunity in the urologic tumor (recall our T-cell depletion experiment), we went on to investigate whether JHU083-treatment causes functional changes in TILs as reported previously [141].

To this end, we re-examined the scRNAseq study that we performed on the $CD45^+$ immune cell fraction from B6CaP tumors following JHU083 treatment **(Fig 5D)**. Within the lymphoid compartment, cell types, namely: T cells (*Cd3d*$^+$, *Trbc2*$^+$), NK cells (*Klrb1c*$^+$, *Gzma*$^+$, *Ncr1*$^+$), and Tgd cells (*Trdc*$^+$, *Il17a*$^+$), were homogeneously represented across all samples **(Fig 5D)**. A further investigation led us to identify a greater diversity of lymphocytes that included a total of 12 different cell clusters identified across samples based on the assigned canonical markers. These lymphocytic sub-set cells included: CD8_1 (*Epsti1*$^+$, *Ly6c2*$^+$, *CD8a*$^+$), CD8_2 (*Pdcd1*$^+$, *Cd8a*$^+$),CD8_3 (*Tcf1*$^+$ *Lef1*$^+$) , NK_1 (*Ly6c2*$^+$ *Sell*$^+$ *Epsti1*$^+$), NK_2 (*Gzma*$^+$, *Tyrobp*$^+$), CD4_1 (*Tcf1*$^+$, *Lef1*$^+$), CD4_2 (*Icos*$^+$, *Rora*$^+$ *Tpt1*$^+$), CD4_3 (*foxp3*$^+$, *Ikzf2*$^+$), CD4_4 (*Eae1*$^+$, *Trps1*$^+$), gdT (*Trdc*$^+$, *Il17a*$^+$, *Tcrg-c1*$^+$) cells and Proliferating cells (*Hmgb2*$^+$, *Stmn1*$^+$, *Birc5*$^+$) **(Fig 19A-C)**. JHU083-treated B6CaP tumors showed a decreased abundance of foxp3+ CD4_3 cluster and increase in both stem cell-like TCF1+ and Lef1+ CD4_1 and CD_8 T cells **(Fig 19A and D)**.

These functional changes in the overall abundance of CD8 and CD4 TILS were orthogonally validated by investigating the TME of both urologic tumors following JHU083 treatment. Flow cytometry-based evaluation of B6CaP and MB49 tumors unveiled an increased percent of stem-like CD8 T cells ($CD44^-$, $CD62L^+$ of $CD8^+$) and a decreased percent of $CD4^+$ Tregs ($FoxP3^+$ of $CD4^+$) in response to JHU083 treatment **(Fig 19E)**.

Next, we investigated whether the stark reprogramming of TAMs in the urologic tumor models in response to JHU083 therapy could relieve the immune suppression on T cells and contribute towards an inflammatory immune response in the TME. DON-treated PBMC-derived macrophages during the differentiation and polarization phases (D1-9) were used to perform a T-cell suppression assay using the autologous T cells **(Fig 20A)**. Autologous $CD8^+$ enriched T cells

co-cultured with DON (0.5 μM)-treated macrophages showed increased proliferation compared to glutamine-enriched media, which served as control **(Fig 20B)**. Moreover, $CD8^+$ T cells co-cultured with these reprogrammed macrophages had increased expression of two key functional markers: TNF-α and IFN-γ **(Fig 20C)**.

Given the fact that DON-treated and reprogrammed TAMs increased polyfunctional $CD8^+$ T cells **(Fig 5H)** and stem-cell-like $CD8^+$ T cells **(Fig 19E)** and decreased proportion of exhausted T cells **(Fig 19D)**, we sought to determine if an ICB therapy in combination with JHU083 would further synergize anti-tumor efficacy of JHU083 in urologic tumors. To this end, we treated MB49 tumors with combinatorial therapy (JHU083 + anti-PD1). Although we observed only a partial response to anti-PD1 monotherapy, the addition of JHU083 resulted in further decreases in tumor volume **(Fig 21A and B)**. However, we could not statistically confirm this combinatorial effect either due to the highly effective TGI caused by JHU083 monotherapy or a model-specific limitation of tumor volume measurement.

Overall, while JHU083-treated T cells contribute less prominently towards a direct anti-tumor role, reprogrammed TAMs can potentially increase the proliferation and polyfunctionality of the T cells *in-vitro*. Additionally, as reported previously, $CD8^+$ TILs in urologic tumors also increase stem cell-like markers and markedly fewer $Treg^+$ cells [141].

Discussion

Classically, in vitro stimulated macrophages have two broader activation states referred to as M1 (classically activated) and M2 (alternatively activated). While M1-polarized macrophages elicit type 1 responses and mediate tumor cell killing; M2-polarized macrophages promote Th2 immunity and are pro-tumoral [24]. Inside tumor niches that represent a more dynamic and complex microenvironment, TAMs display a remarkable ability to adapt to a broad spectrum of intermediate activation states while co-existing together [144]. Specific TAM subsets play a dual supportive or inhibitory role in cancer progression. As discussed, M2-TAMs are pro-tumoral and promote oncogenesis, angiogenesis, epithelial-to-mesenchymal transition (EMT), metastasis, and provide protective niches for cancer stem cells; M1-TAMs exert tumoricidal functions and support the efficacy of various anti-tumor immunotherapies [71]. TAMs thus stand out as promising targets for developing novel anti-tumor immunotherapies [19], prompting the development of several myeloid-targeting immunotherapies targeting their recruitment, accumulation, reprogramming, checkpoints, and immunometabolism [71].

The challenges faced by T cell-based ICB in prostate carcinoma (PCa) are mainly due to the restricted CD8 T cell infiltration [145] with a concomitant increase in immunosuppressive M2-TAMs in the TME [146]. In fact, immunosuppressive M2-TAMs remain the major obstacle in prostate cancer immunotherapy.

Targeting metabolic checkpoints offers promising opportunities for cancer therapies. Specifically, targeting glutamine metabolism could help maximize the efficacy of existing cancer therapies. Prostate tumors are highly glutamine-addicted, also M2-TAMs display increased glutamine uptake that appears to promote M2-macrophage polarization [147]. In this study, we have used a novel glutamine antagonist as a therapeutic agent to understand the effects of glutamine

inhibition on the metabolic remodeling of TAMs and its consequential impact on their anti-tumor functional attributes in urologic cancers.

Taking advantage of a published dataset that earlier characterized metastatic prostate cancer in bone marrow as well as matched tissues at single-cell resolution using single-cell transcriptomics [147], we investigated the involvement of tumor-infiltrating immune cells in glutamine metabolism. Our analysis showed increased expression of several glutamine-utilizing enzymes, including *GLS* and *GLUL,* in both TAMs and TIMs in PCa tumors and involved BM fraction **(Fig 1)**, suggesting increased roles of these myeloid cells in glutamine metabolism. This also reinforces the therapeutic benefit of glutamine metabolism inhibition in mCRPC to address the unmet need of therapeutic interventions. Glutamine metabolism in tumors represents an important metabolic checkpoint and remains one of the most promising approaches to target solid tumors [141].
Here for the first time, we carried out the comprehensive evaluation of JHU083, a novel antagonist of glutamine utilizing enzymes as an immunotherapeutic intervention in urologic (prostate and bladder) tumor models. We found that in vivo administration of JHU083 caused a stark TGI in three different syngenetic mouse models of urologic tumors **(Figure 2)**. Sfanos et al. earlier reported the 'exhausted' nature of prostate tumor infiltrating CD8 T cells due to very high expression of PD-1, while the presence of these cells is associated with an increased risk of clinical progression in men indicating further validating our results [148].

Using the T cell depletion experiments, we characterized a mild TGI contributed individually by either CD8β or CD4 T cells, as JHU083 administration caused significant TGI despite T cell ablation **(Fig 3)**. In addition, using the adoptive transfer experiments with TAMs and TIMs **(Fig 4)**, for the first time, show the role of myeloid cells in delaying tumor growth following JHU083-mediated glutamine antagonism. Previously Leone et al. showed increased global methylation in T cells on broad methylation sites following JHU083-treatment caused memory phenotype of CD8

T cells in breast cancer [141]. The TCA cycle metabolite α-KG is essential for increasing OXPHOS and FAO (fatty acid oxidation) in M2 macrophages. In addition, α-KG plays a key role in M2-macrophage polarization through Jmjd3 (Jumonji domain-containing 3, a key enzyme for demethylation of H3K27)-dependent demethylation of H3K27 in the promoter region of M2-specific marker genes [123]. Given the limited availability of α-KG in the TME due to JHU083-mediated glutamine antagonism, the likelihood of cessation of such epigenetic mechanism leading to M2-TAM polarization could not be ruled out and remains to be fully explored. Whether JHU083 treatment led to qualitative and quantitative changes in TAM phenotypes and abundance in prostate (B6CaP) tumors, we used two complementary approaches in which sorted total immune cells and TAMs were used to perform scRNAseq and bulk RNAseq studies. The GSEA analysis led to the identification of different TAM populations in B6CaP tumors that showed upregulation of the hallmark TNF signaling and inflammatory pathways and an increased proportion of proliferative TAMs following JHU083 treatment.

Previously Oh et al. reported reduced infiltration of immunosuppressive MDSCs in a triple-negative breast cancer (4T1) model following JHU083 treatment without overall changes in myeloid cell recruitment [112]. Here, we report an overall increase in the percentage infiltration of total myeloid cells (live $CD45^+$ $CD11b^+$) and TIMs (live $CD45^+$ $CD11b^+$ $Ly6G^-$ $Ly6C^{(hi)}$) in the myeloid-rich urologic TME after JHU083-monotherapy **(Fig 9 B-E)**. The differential changes in the myeloid cell recruitment and TAMs with antigen-presenting markers (CD86 and MHCII expression, as M1 markers) in urologic (B6CaP and MB49) and 4T1 tumors could be due to the model-specific varying TME and tumor heterogeneity.

Since we found TAMs and TIMs as the primary immune cell types involved in anti-tumor immunity conferred by JHU083 in the urologic TME, we looked closely at the signaling pathways modulated in these cells in prostate tumors. We found TNF signaling induction in different subsets of TAMs and TIMs **(Figure 9)** as well as an increase in the percentage of TNF-secreting M1 and M2 TAMs

(Fig 9) after JHU083 treatment as a significant phenotype. Conformingly, Oh *et al.*, in the 4T1 tumors, reported a TNF-mediated anti-tumor effect by TAMs following JHU083 therapy [141]. Additionally, increased TNF and inflammatory signaling reprogram TAMs and promote their anti-tumor immunity [149]. Moreover, newer macrophage immunotherapies targeting CD40-CD40L, IFN-mediated STING pathways, and LILRB2 in different models have shown TNF-mediated anti-tumor immunity [71]. Our results demonstrate that the major role of TNF signaling in TAMs and TIMs could be attributed to the anti-tumor efficacy of JHU083 in urologic cancer.

Additionally, for the first time, we also report an induced cell proliferation signaling in subsets of TAMs and the proliferative resident TAM cluster enriched in the TME after glutamine antagonism. The flow-cytometry-based evaluation of B6CaP tumors showed increased Ki67+ TAMs **(Fig 10)** following JHU083 treatment that was in line with the observations made in the GSEA analysis in TAMs that earlier showed upregulation of hallmark signaling pathway genes involved in proliferation **(Fig 7)**. Interestingly, the RNA velocity analysis predicted that the proliferating TAMs were developmentally unrelated to the infiltrating monocytes, a phenotype that remains tentative and could be explored for its origin and significance in the TME.

One of the most promising strategies that target pro-tumoral TAMs in myeloid-rich preclinical tumor models or clinical trials in humans includes blocking angiogenesis and improving phagocytosis of malignant cells by TAMs [72]. We demonstrated that JHU083-treated TAMs were increasingly phagocytic *in vivo* **(Fig 11)**. Indeed, increased phagocytic features were not limited to M1-TAMs, but $CD206^{+}$ M2-macrophages also showed increased phagocytosis of tumor cells **(Fig 11C)**. We further confirmed the augmented phagocytic capacities in *in vitro* cultured and M2 polarized PBMC-derived macrophages that showed increased phagocytosis of PC3 cells after DON treatment **(Fig 11 C and E)**. A recent report suggests that tumor cells resistant to phagocytosis induce macrophage mitochondrial fission by glutamine-fructose-6-phosphate transaminase 2 (GFPT2)-mediated excessive use of glutamine [150], suggesting the effects of glutamine on phagocytosis capacities of TAMs. Our results are direct evidence that tweaking

glutamine metabolism could affect the phagocytosis of TAMs in the TME **(Figure 11-12)**. We also found increased expression of *Myo1e* in JHU083-treated TAMs. Interestingly, *Myo1e* plays a key role in adhesion turnover during phagocytosis and in membrane-cytoskeletal crosstalk for phagocytic cup closure [151]. How glutamine metabolic inhibition results in *Myo1e*-mediated increase of tumor cell phagocytosis by TAMs remains to be fully explored.

We also found decreased angiogenesis in JHU083-treated prostate and bladder carcinoma tumors, as evidenced by decreased tissue level expression of CD31 (vascular differentiation marker), indicating reduced neovascularization **(Fig 13)**. Our findings suggest the possibility of using other synergistic combination therapies to increase phagocytosis and antigen presentation of TAMs such as blockade of CD47-SIRPα or angiogenic inhibition with like ANG2–VEGF [71].

Changes in TNF and inflammatory signaling pathways in TAMs and TIMs in urologic tumors following treatment JHU083 prompted us to thoroughly investigate the metabolic changes in TAMs following treatment. Overall, in the prostate cancer TME, we discovered a significant rewiring of glycolysis, TCA cycle, and purine metabolism after JHU083 treatment **(Fig 14-16)**. Bradley *et al.,* in a landmark study using positron emission tomography, highlighted the nutritional partitioning of glucose and glutamine in freshly resected urologic carcinoma [152]. Strikingly, they reported the greatest glucose uptake capacity was displayed by myeloid cells in the TME, followed by T cells and cancer tissue, while cancer cells showed the highest glutamine uptake in the different tumor models [152]. This study also showed that this was a result of cell-intrinsic mechanisms through mTORC1-regulated glucose and glutamine-related gene expression. Here, for the first time, we show the divergent metabolic responses of glutamine antagonism by JHU083 on intra-tumoral TAMs that result in increased glycolysis and succinate shunting in the TCA cycle **(Fig 14-16).** This shunting of succinate and a break in the TCA cycle has previously been highlighted in *in vitro* differentiated inflammatory M1 macrophages that promote IL-1β levels by increased activity of succinate dehydrogenase B activity [142]. Indeed, we found both *Sdhb* and *il1b* transcripts increased in the total TAM population after JHU083 treatment.

Clinical trials of therapeutic remodeling via metabolic inhibition of oxidative phosphorylation pathway (NCT03291938 and NCT03272256), tryptophan metabolism (NCT02752074), and prostaglandin E2 synthesis (NCT03026140 and NCT03926338) in myeloid cells in different neoplasms have shown promise [153]. Regardless of such progress, the failure of the phase III trial of IDO inhibitor (ECHO-301/KN-252) highlights the key challenges of a compensatory expression of similar enzymes in targeting individual metabolic enzymes [154]. DON not only acts as an irreversible inhibitor of glutamine but also acts as a mechanism-based blocker of glutamine utilizing enzymes affecting multiple pathways [113]. Simultaneous inhibition of metabolic pathways based on differential binding affinities at particular concentration of JHU083 provides a unique opportunity to rule out therapeutic resistance in addition to superior intra-tumoral delivery [127]. In addition to the increased glycolysis and break in the TCA cycle, targeting multiple enzymes via JHU083 likely impacts purine metabolism [113].

Two other DON pro-drugs have concurrently shown the inhibition of phosphoribosyl formylglycinamidine synthetase (PFAS), an enzyme in purine metabolism that acts on FGAR intratumorally in cancer cells [113]. Here, we report increased accumulation of FGAR in both tumor cells and TAMs in both urologic tumors following JHU083 treatment **(Fig 15 and 17)**, elucidating the possibility of inhibition of PFAS. Moreover, in a recent study, purine metabolism was elicited as a key metabolic pathway feature of pro-tumoral macrophages [155]. Further investigations would be needed to dissect the impact of glutamine inhibition purine metabolism in TAMs.

Unlike normal cells that maintain a perfect balance between catabolism and anabolism, rapidly proliferating cancer cells are chiefly anabolic to meet the ever-increasing bioenergetic needs and essential building block molecules for growth and proliferation. This highly specialized metabolic reprogramming in tumor cells includes increased glutaminolysis, glycolysis, and de novo fatty acid synthesis [156]. Moreover, as highlighted by Bradley et al., urologic cancer cells have the highest glutamine uptake as compared to immune or stomal cells [152]. Tumor cells show increased

glutaminolysis to meet NADPH demands and TCA cycle intermediates as the essential building blocks for anabolic growth and proliferation [156]. Here, we show that in urologic tumor cells, JHU083 inhibits not only glutamine metabolism but also glycolysis, amino acid metabolism, one-carbon metabolism, hexosamine pathway, and nucleotide synthesis. This results in an overall impact on HIF-1α and c-MYC signaling, probably causing a global metabolic shutdown. Congruently, we quantified an induction of apoptosis in the non-immune ($CD45^-$) cells from JHU083 as well **(Figure 17-18)** as another outcome of a global metabolic shutdown on cancer cell survival.

Tumor cells continuously compete with tumor-resident immune cells, including TAMs, MDSCs, and T cells, a net result of which is altered tumor metabolites levels causing glucose starvation and accumulation of lactate and ammonia that creates a classical nutrient-deprived, acidic, and hypoxic TME unsuitable for normal immune cell function. This specialized metabolic reprogramming of tumor cells represents the second-generation hallmarks of cancer, highly promising targets of altered tumor-cell metabolism [117].

Previously, Leone et al. and Oh et al. reported T cell-mediated anti-tumor response as one of the key features of glutamine metabolic inhibition by JHU083 in different tumor models. Our investigation shows consistent observation in increased stem-cell-like $CD8^+$ T cell phenotype as previously reported [141]. Additionally, as a direct consequence of reprogrammed TME (TAMs and myeloid cells), we observed a reduction in the percentage of $Foxp3^+$ Tregs in JHU083-treated tumors **(Fig 19)**. Differentiated macrophages in vitro after glutamine blockade are shown to relieve the immune suppression on T cells by increased proliferation, TNF and IFN-γ secretion **(Fig 20)**. While we were unable to quantify these changes *in vivo*, a direct consequence of the reprogrammed macrophages/ monocytes on T cell features remains to be further explored. Although JHU083-induced increased effector functions of CD8 T cells *in vivo* and *in vitro*, we were unable to exhibit the superior combinatorial effect of anti-PD1 with JHU083 treatment **(Fig 21)**.

This could be either due to the extremely high TGI by JHU083-monotherapy or having poor efficacy of anti-PD1 blockade. Other T cell checkpoints and plausible usage of combinatorial checkpoint therapy in urologic tumors remain to be elucidated.

While this study provides key insights into the metabolic and phenotypic features of TAMs and TIMs in urologic tumors, its direct effect on T cell immunity remains to be further explored. Our effort to combine JHU083 with anti-PD1 immunotherapy in the prostate tumor model was aimed at achieving even superior anti-tumor benefits. However, our results suggest potential limitations of tumor models that represent the true TME to determine the overall effects. Further finding out the right doses of JHU083 for combination therapy in prostate tumor models could need further optimization. Although we have used MB49 urothelial tumor model to see similar responses as observed in prostate tumors due to its myeloid-rich TME, the model-to-model variation in treatment responses exists, and that was reflected in different experiments that were performed in this study. Another key limitation of this study involves long-term effects on tumor metastasis, a phenotype that remains to be examined in a relevant tumor model of prostate carcinoma.

Overall, we provide a metabolic and phenotypic snapshot of immunosuppressive TAMs in prostate tumors following therapeutic glutamine blockade. This study is unique because it enriches our understanding of remodeled TAMs following glutamine antagonism using a novel prodrug and provides a further basis to use this drug alone or in combination with existing therapies aimed at targeting TAMs in immunologically cold prostate tumors.

Materials & Methods

Ethics. All protocols used in this study involving animals strictly followed US NIH guidelines and were approved by the Johns Hopkins Medical Institutions Animal Care and Use Committee.

Animals

Experimental protocols involving live animals were performed in agreement with the protocols approved by the Institutions Animal Care and Use Committee (IACUC) at The Johns Hopkins University School of Medicine. Both male and female C57BL/6J (000664), aged 6-8 weeks, were purchased from Jackson Laboratories (ME, USA). Animals were kept under standard housing conditions (68-76 °F, 30-70% relative humidity, 12-12 light-dark cycle) with free access to standard chow and water. The animals were monitored daily for general behavior and appearance by veterinary specialists.

Tumor models and cell lines

MB49, a mouse urothelial carcinoma cell line (SC148) derived from an adult C57BL/6 mouse by exposure of primary bladder epithelial cell explant to 7,12-7,12-dimethylbenz[a]anthracene (DMBA) for 24 h followed by a long-term culture, was purchased from Sigma. B6CaP $CD45^{-ve}$ cells were gifted by Dr. Brian Simons (affiliation). RM-1 (CRL-3310™) a mouse prostate carcinoma cell line of a fibroblast-like morphology, was purchased from ATCC. MB49-luciferase RFP cells (SC065-R) were purchased from GenTarget Inc. MB49 or RM1 cells were cultured in DMEM supplemented with 10% FBS and 1% penicillin/streptomycin at 37 °C with 5% CO_2. Cells were harvested following trypsinization, and cell viability was confirmed using Trypan blue dye. For syngeneic heterotopic MB49 urothelial tumor development, live MB49 cells (5.0×10^4 cells per 100ml of 1x PBS per mouse) were implanted on the right flank in C57BL/6J female mice. For the development of syngeneic heterotopic prostate carcinoma tumors, B6CaP $CD45^{-ve}$ cells were

thawed, washed with 1 x PBS, and implanted subcutaneously (5.0 x 10^6 cells per 100 ml 1x PBS per mouse) on the right flank of C57BL/6J male mice for passaging of the cells in mice. Once the tumors reached 1000 mm^3, they were harvested and implanted after CD45 negative enrichment. Tumor growth was monitored every second day to observe the increase in the tumor burden at the time of treatment initiation. Tumors were measured by electronic caliper, and tumor volume was calculated using the following equation: tumor volume = (1/2 (length x (width)^2). The maximum allowed tumor, the volume of ~2 cm in any dimension, was based on the guidelines of the institutional IACUC for a single implanted tumor that was visible without imaging.

DON and JHU083 Treatment

6-diazo-5-oxo-L-norleucine (DON, D2141) was purchased from Sigma-Aldrich. JHU083 (Ethyl 2-(2-Amino-4-methylpentanamido)-DON) was synthesized as previously described and was provided by Dr. Barbara Slusher (Johns Hopkins University). Briefly, JHU083 was administered intraperitoneal (p.o.) at a dose of 1.83 mg/kg (1mg/kg DON molar equivalent) in 1x sterile PBS. Once palpable, tumor-bearing C57B/6J mice were orally treated with 1.82 mg/kg JHU-083 or vehicle for 5-9 days daily and then at a lower dose of 0.61 JHU083 (0.3 mg/kg DON equivalent). For all drug administrations, care was taken to handle animals gently to minimize stress.

***In vivo* drug treatment and T cell-specific depletion**

Palpable (100-500 mm^3) tumor-bearing mice were treated with a vehicle referred to as control (1 x sterile PBS) or with the 1.82 mg/kg pro-drug JHU083 (1 mg/kg DON equivalent) daily for 7 or 9 days. After 1.82 mg/kg daily treatments, a reduced 0.61 mg/kg (0.3 mg/kg DON equivalent) was given daily till the vehicle control tumors reached a maximum tumor volume of 2000mm^3 **(Fig 1C)**. For $CD4^+$ T cell depletion, mice were injected intraperitoneally (i.p.) with 200 mg of anti-CD4 (InVivoPlus GK1.5, BP0003-1, BioXCell) or Isotype control (InVivoPlus rat IgG2b isotype control, anti-keyhole limpet hemocyanin, LTF-2, BP0090, BioXCell) antibodies in 100 ml of 1 x PBS per

mouse on day 3 prior to tumor inoculation and then once every week till the end of the experiment. For $CD8^+$ T cell depletion, mice were injected with a similar dosage as used for an anti-CD4 antibody with either anti-CD8b (InVivoMAb Lyt 3.2, 53-5.8, BE0223, BioXCell) or Isotype control (InVivoMAb rat IgG1 isotype control, anti-horseradish peroxidase, HRPN, BE0088, BioXCell) antibodies. For studies combining anti-PD1 therapy, MB49 tumor-bearing mice after MB49 cell implantation were treated intraperitoneally with either 250 µg anti-PD1 (InVivoPlus RMP1-14, #BP0146, BioXCell) or JHU083 at 1.82mg/kg daily orally, both or Isotype control (InVivoPlus rat IgG2a isotype control, anti-trinitrophenol, 2A3, BP0089, BioXCell) on every third day.

Adoptive transfer experiments

Following the development of palpable MB49 tumors (100-200 mm^3), tumor-bearing B6 mice were orally given JHU083 (1 mg/kg equivalent to DON) or vehicle control (1 x PBS) daily for 7 days and then, a reduced dose of 0.3 mg/kg equivalent of DON until the experimental endpoint was met. Single-cell suspensions were made from harvested tumors, and $CD45^+$ cells were enriched using the mouse CD45 isolation kit (130-110-618, Miltenyi) and were surface stained. Briefly, tumor-associated macrophages (TAMs) (Live $CD45^+$ $CD3^-$ $Ly6G^-$ $CD11b^+$ $F4/80^+$) cells were isolated from the donor mice (vehicle control or JHU083-treated) mice and sorted by FACSAria. Sorted macrophages (TAMs) were then mixed at a 1:1 ratio with MB49 tumor cells, and 60,000 cells in total were injected subcutaneously into host C57BL/6J female mice for tumor development. Tumor volume measurements were done 3 times a week after palpable tumors were developed. These tumor-bearing animals were then orally given either 0.3 mg/kg equivalent of DON or sterile 1x PBS. Similarly, for tumor-infiltrating monocyte (TIM) adoptive transfers, TIMs (Live $CD4^{5+}$ CD3- $CD11b^+$ $Ly6G^-$ $Ly6C^{high}$) were separately sorted by FACSAria (BD) from both JHU083- or vehicle (1 x sterile PBS) treated mice. Sorted TIMs were then mixed with MB49 at a 1:1 ratio and injected subcutaneously into recipient syngeneic C57BL/6J female mice.

Tumor Digestion, flow cytometry, and sorting

Tumors were surgically resected, mechanically minced, and digested using Miltenyi's mouse tumor dissociation kit (130-096-730) according to the manufacturer's protocol using gentleMACS™ Octo dissociator (130-096-427). After tumor digestion, cells were filtered through a 100 mm cell strainer (TC70-MT-2, Stellar Scientific). For flow cytometry, single-cell suspensions were washed with 1x PBS and then incubated with ACK lysing buffer (118-156-721 Quality Biologicals). For fluorescence-activated cell sorting (FACS), cells were washed, and tumor-infiltrating $CD45^+$ cells were enriched using the mouse CD45 isolation kit (130-052-301, Miltenyi) as per the manufacturer's protocol. After staining, tumor-associated macrophages (TAMs) or monocytes (TIMs) were sorted using BD FACSAria™ Fusion.

Flow cytometry

Single-cell suspensions were stained with antibodies after viability staining and FcR blocking (BD bioscience, 564765). The following antibodies or dyes were purchased for cell surface or intracellular staining. The staining was followed according to the manufacturer's protocol. For intracellular staining, eBioscience™ Foxp3 / Transcription Factor Staining Buffer Set (00-5523-00, ThermoFisher scientific) was used and was performed as per the manufacturer's protocol. Following that, cells were washed and immunophenotyped using BD FACS Celesta, BD FACS symphony, or Cytek Aurora, and data were analyzed using FlowJo (Version 9 or 10). **Table 2** contains the list of mouse and human antibodies used in this study.

RNA preparation, bulk RNA sequencing, and data analysis

Bulk RNA sequencing was performed in FACS-sorted tumor-associated macrophages (TAMs) from mouse B6CaP tumors. Single cell preparations from the vehicle or JHU083-treated tumors were prepared and used for isolation of TAMs (Live $CD45^+$ $CD3^-$ $Ly6G^-$ $CD11b^+$ $F4/80^+$) via sorting on BD FACSAria™ Fusion after cell surface staining. The total RNA was isolated from vehicle

(n=3) and JHU083-trearted (n=3) tumors using the Trizol (15596026, ThermoFisher scientific) reagent based on the manufacturer's protocol. For RNA sequencing, RNA samples were converted to double-stranded cDNA using the Ovation RNA-Seq System v2.0 kit (Tecan, Männedorf, Switzerland), which utilizes a proprietary strand displacement technology for linear amplification of mRNA without rRNA/tRNA depletion as per the manufacturer's recommendations. This approach does not retain strand-specific information. Quality and quantity of the resulting cDNA were monitored using the Bioanalyzer High Sensitivity kit (Agilent), which yielded a characteristic smear of cDNA molecules ranging in size from 500 to 2000 nucleotides in length. After shearing 500 nanograms of cDNA to an average size of 250 nucleotides with the Covaris S4 (Covaris Inc., Woburn, MA), library construction was completed with the Truseq Nano kit (Illumina; San Diego, CA) according to the manufacturer's instructions. The mRNA libraries were sequenced on an Illumina Novaseq 6000 instrument using 150bp paired-end dual-indexed reads and 1% of PhiX control. Reads were aligned to genome build mm39. rsem-1.3.0 was used for alignment as well as for generating gene expression levels. The 'rsem-calculate-expression' module was used with the following options: --star, --calc-ci, --star-output-genome-bam, --forward-prob 0.5. Differential expression analysis and statistical testing were performed using DESeq2 software. The identified list of significantly differentially expressed genes (DEGs) was then enriched for their biological functions to explore and evaluate their involvement in critical biological processes in the context of the study. Largely, we employed Gene Set Enrichment Analysis (GSEA) using the R statistical tool to screen statistically significant, cumulative changes of groups of genes in the context of pathway analysis.

Single-cell sequencing (scRNA-seq) and data analysis

FACS-Sorted $CD45^+$ and $CD45^-$ cells from B6CaP tumors were used for scRNA sequencing. Briefly, cell counts, and viability were determined using the Cell Countess 3 with Trypan Blue. A maximum volume of 86.4 uL/sample was used for processing to target up to 20,000 cells. Cells

were combined with RT reagents and loaded onto 10X Next GEM Chip M along with 3' HT gel beads. The NextGEM protocol was run on the 10X Chromium X to create GEMs (gel bead in emulsion), composed of a single cell, gel bead with a unique barcode and UMI primer, and RT reagents. 180uL of emulsion is retrieved from the chip, split into 2 wells, and incubated (45 min at 53C, 5 min at 85C, cool to 4C), generating barcoded cDNA from each cell. The GEMs are broken using Recovery Agent, and cDNA is cleaned, following the manufacturer's instructions using MyOne SILANE beads. cDNA is amplified for 11 cycles (3 min @ 98C, 11 cycle: 15sec @ 98C, 20sec @ 63C, 1min @ 72C; 1min @ 72C, cool to 4C). Samples are cleaned using 0.6X SPRIselect beads. QC is completed using Qubit and Bioanalyzer to determine size and concentrations. 10uL of amplified cDNA is carried into library prep. Fragmentation, end repair, and A-tailing are completed (5 min @ 32C, 30 min @ 65C, cool to 4C), and samples are cleaned up using double-sided size selection (0.6X, 0.8X) with SPRIselect beads. Adaptor ligation (15min @ 20C, cool to 4C), 0.8X cleanup, and amplification are performed, with PCR using unique i7 index sequences. Libraries undergo a final cleanup using double-sided size selection (0.6X, 0.8X) with SPRIselect beads. Library QC is performed using Qubit, Bioanalyzer, and KAPA library quantification qPCR kit. Libraries are sequenced on the Illumina NovaSeq 6000 using v1.5 kits, targeting 50K reads/cell at read lengths of 28 (R1), 8 (i7), and 91 (R2). Demultiplexing and FASTQ generation are completed using Illumina's BaseSpace software.

Sequencing was performed in a total of 10,000 cells. After filtering out low-quality cells, red blood cells, and doublets, cells were analyzed for data interpretation.

To identify which macrophage cluster from the early time point (single-cell experiment) matches the transcriptional changes seen in macrophages at a later time point (bulk experiment), we performed GSEA on each cluster between JHU-treated and control samples. The list of significant up-regulated and down-regulated genes identified in the macrophage-sorted bulk RNA-seq experiment (late time point) was used as input as the respective 'up' or 'down' gene sets in the GSEA analysis. A score was calculated to rank each macrophage cluster based on the

enrichment of both up- and down-regulated gene sets by summing the p-value-weighted absolute values of each normalized enrichment score:

score = |NESup| * -log10(adj.pup) + |NESdown| * -log10(adj.pdown)

Single-cell RNA sequencing data mining

The previously published and publicly available human prostate cancer bone metastases data published by Kfoury et al. (2021) were downloaded as an RData object provided through the author's website https://pklab.org/bonemet [157]. Cell type annotations for the human datasets were downloaded through the Gene Expression Omnibus with the accession number GEO: GSE143791. Given that most, but not all, of the cells were annotated in the RData Conos object corresponding to the joint analysis of all samples, the remaining cells were labeled with the propagateLabels[AS2] () function. The data was then converted to a Seurat object for further analysis by extracting the expression matrix, cluster assignments, and tSNE embeddings from the Conos object [158], [159]

[159]Targeted Metabolomics and pathway analysis

Metabolites were extracted from flash-frozen whole tumors normalized by dry weights by individual tumor (B6CaP or MB49) or FACS-sorted TAMs (from B6CaP tumors) with 80% methanol (80% methanol: 20% water: v/v). Supernatants were isolated after centrifugation at high speed (15,000 g) for 10 mins and dried under nitrogen gas and stored at -80 °C for further liquid-chromatography mass spectrometry (LC-MS) analysis. Finally, dried metabolite extracts were dissolved in 50% Acetonitrile (ACN) solution, and metabolome profiling was performed on the Agilent LC-MS/MS system. The LC-MS/MS parameters used were as described previously [141]. Relative metabolite abundance was plotted and normalized (per mg of tumor tissue or the cell counts.

Absolute quantification of intra-tumoral metabolites

LC/MS-based absolute quantifications of glutamine, glutamate, and glucose were done using a validated method as previously described [160]. Briefly, glutamine and glutamate were extracted by one- step protein precipitation. Five microliters of methanol containing 10 µmol/L deuterated glutamate, glutamate, and glucose (internal standard) were added per mg of the tissue. Samples were centrifuged at 16,000 x g for 5 minutes at 4 °C. A standard concentration curve of glutamate and glutamine was prepared (0.1–10,000 µmol/g). Samples were analyzed using an Agilent 1290 UPLC coupled to an Agilent 6520 quadrupole time of flight mass spectrometer. Samples (2 µL) were injected and separated on a Waters Acquity UPLC BEH Amide 1.7 µm 2.1 x 100 mm HILIC column with a flow rate of 0.3 mL/minute. The mobile phases consisted of A (water + 0.1% formic acid) and B (acetonitrile + 0.1% formic acid). The mass spectrometer, equipped with a DUAL ESI ionization source, was run in positive, then negative ion mode for glutamine and glutamate, then glucose analysis, respectively. Data were acquired and quantified with MassHunter software.

Absolute quantification of formylglycinamide ribonucleotide (FGAR) was performed as previously described [155] with minor modifications. Briefly, FGAR was extracted from tumors by the protein precipitation method. Five microliters of methanol containing 10 µmol/L deuterated N-acetylaspartic acid (internal standard) was added per mg of tissue. Tissue samples were homogenized and centrifuged (16,000 × *g*, 5 minutes). For quantification, supernatants (2 µL) were injected and separated on an UltiMate 3000 UHPLC coupled to a Q Exactive Focus orbitrap mass spectrometer (ThermoFisher Scientific Inc.). Samples were separated on an Agilent EclipsePlus C18 RRHD (1.8 µm) 2.1 × 100 mm column. The mobile phase consisted of 8 mmol/L dimethylhexylamine (DMHA) + 0.005% formic acid in the water, pH 9 (A), and 8 mmol/L DMHA in acetonitrile (B). Separation was achieved at a flow rate of 0.4 mL/min using a gradient run. Quantification was performed in Full MS negative mode. Data was acquired and quantified with Xcalibur software.

In vivo glucose tracing in TAMs

20% (w/v) solution of [U-13C] glucose was used and injected intravenously thrice in 15-minute intervals in restrained B6CaP tumor-bearing mice without anesthesia [141]. 45 mins after the first injection of mice, tumors were harvested. Rapid tumor digestion for 10-15 minutes was performed as in 1x PBS following passing through cell strainers and ACK lysis mentioned previously. Tumor-infiltrating $CD45^+$ cells were enriched for 10 mins using the mouse CD45 isolation kit (130-052-301, Miltenyi), following fast staining in a pre-made antibody cocktail for FACs. TAMs were sorted with BD FACSAria™ Fusion, and the protocol for polar metabolites isolation was followed as stated. The cold chain at 4 °C was maintained throughout the protocol and cells except for digestion.

Phagocytosis assay

The in vitro phagocytosis assay was carried out using fluorescence microscopy. Briefly, in vitro cultured macrophages were stained with PKH26 dye (PKH26GL-1KT, Sigma-Aldrich), and PC3 (prostate adenocarcinoma cells, CRL-1435™, ATCC) were labeled with 2.5 μM carboxyfluorescein succinimidyl ester (CSFE, C34554, ThermoFisher scientific) according to the manufacturer's description. PBMC-derived differentiated macrophages were treated using the vehicle or non-toxic dosage of DON either during differentiation Day 1-9 or during polarization Day 5-9 and were subsequently co-cultured with PC3 prostate carcinoma cells at a 1:2 ratio (macrophages: PC3 cancer cells) and incubated for 2 h at 37 °C in sterile glass slides in 6 well plates. Cells were repeatedly washed to remove non-phagocytosed PC3 cells and were subsequently imaged with an Echo Dot Revolve microscope. We also used flow-cytometry-based quantification of phagocytosis of PC3 cells. Briefly, unstained differentiated macrophages were co-cultured with CFSE-labelled PC3 cells for 2h. Cells were repeatedly washed to remove non-

phagocytosed cells, detached, and stained with a viability dye, anti-CD45, and anti-CD11b antibodies for flow-cytometry-based evaluation.

To perform the in vivo phagocytosis assay, MB49-RFP cells were implanted for tumor development; following the growth of palpable tumors, animals were treated with JHU083 as described earlier. The percentage phagocytosis of MB49-RFP+ tumor cells was quantified based on flow-cytometry-based evaluation of appropriately cell surface-stained cells.

Immunohistochemistry (IHC)

Immunostaining of tumor tissues were performed at the Oncology Tissue Services Core of Johns Hopkins University. Chromogenic immune-labeling was performed on formalin-fixed, paraffin-embedded sections on a Ventana Discovery Ultra autostainer (Roche Diagnostics). Briefly, following dewaxing and rehydration on board, epitope retrieval was performed using Ventana Ultra CC1 buffer (catalog# 6414575001, Roche Diagnostics) at 96 °C for 64 minutes or using a target retrieval solution (catalog# S170084-2, Dako) for 48 minutes at 96 °C for CD8 antigen. Primary antibodies were used for staining and were detected using an anti-rabbit HQ detection system (catalog# 7017936001 and 7017812001, Roche Diagnostics) followed by Chromomap DAB IHC detection kit (catalog # 5266645001, Roche Diagnostics), counterstaining with hematoxylin, bluing, dehydration, and mounting.

Whole slide brightfield scans were performed on a Hamamamtsu NanoZoomer XR (C12000-02, Hamamatsu, Hamamatsu City, Japan). Image analysis was performed using HALO ver. 3.3.2541 (Indica Labs, Albuquerque, NM) with module Area Quantification v2.1.10. The details of antibodies and dilutions used to perform IHC are listed in **Table 3**.

Drug treatment

DON treatment in CD14+ PBMC derived macrophages differentiation/polarization

Briefly, $CD14^+$ monocytes were isolated from freshly collected PBMCs from healthy donors (leukopacks) and were differentiated into macrophages as previously reported [135]. $CD14^+$ monocytes were treated with various doses of DON (0.5 µM to 10 µM) either on Day 0 following cell plating and/or during differentiation or on Day 5 in differentiated monocytes during polarization till Day 9.

$CD8^+$ T cell suppression assay

To perform cell suppression assays, 0.7 x 10^5 of fully differentiated and polarized macrophages (M2/M2) were harvested using cell stripper solution (# Cat, Corning), counted, and seeded (please mention the cell number) into a 24-well flat bottom plate in 500 µL RPMI 1640 medium supplemented with 10% heat-inactivated FBS (HI-FBS) for 2 hours. $CD8^+$ T cells were isolated and enriched from the PBMCs of the same healthy donor using a human $CD8^+$ T cell negative selection kit (Stem cell technology, 19053). Negatively selected, enriched $CD8^+$ T cells were stained with CellTrace Violet (CTV) dye (ThermoFisher, C34557) at 1:1000 dilution as per the manufacturer's protocol. 1.5 x10^5 CTV stained $CD8^+$ T cells were resuspended in 500 uL RPMI 1640 medium supplemented with 10% HI FBS and co-cultured with previously seeded and adhered macrophages from the same healthy donor. Subsequently, 24 µL of Human CD3 / CD28 / CD2 T Cell Activator (Stem cell technology, 10970) and 30 unit/mL animal-free human recombinant IL-2 (Peprotech, AF-200-02) were added, followed by incubation at 37 °C, 5% CO_2 for 3 days. $CD8^+$ T cells were harvested at the end point and evaluated using flow cytometry analysis.

MTS assay

Murine MB49 cells, either 10,000 or 20,000 cells, were put into a 96-well flat-bottom culture plate per well and incubated for 2 hours at 37 °C and 5% CO_2. Subsequently, cells were either vehicle-treated or treated with DON at 0.5 µM, 1 µM, and 2 µM overnight. Following incubation, 20 µL

CellTiter 96 AQueous One Solution Cell Proliferation Assay (Promega cat#G3582) was added per well and incubated at 37 °C for 1 hour. Absorbance was measured at 490 nm using spectraMax Plus (Molecular Devices).

Immunoblotting

Tumors were harvested at the experimental endpoint and digested to prepare single cells as described above. Both $CD45^+$ and $CD45^-$ cells were isolated using a mouse CD45 (TIL) MicroBeads kit (Miltenyi 130-110-618) per the manufacturer's protocol. For $CD45^-$ cell faction, dead cells were then removed using Dead Cell Removal Kit (Miltenyi cat# 130-090-101). For the $CD45^+$ fraction, TAMs were sorted as described previously. For protein extraction from human monocyte-derived macrophages, fully differentiated and polarized macrophages were dissociated by cell stripper (Corning, 25-056-CI) and washed with 1 x PBS. Whole-cell protein lysate was collected using MAPK buffer supplemented with protease inhibitor (SelleckChem and Sigma), and protein concentration was determined by Bradford reagent (Biorad, 5000202). Equal concentrations of protein samples were loaded and resolved by SDS-PAGE and were subsequentially transferred to the PVDF membrane, followed by 5% BSA blocking. Membrane blots were incubated with primary antibodies (see the table below) overnight; either starbright 520 conjugated secondary antibody (Biorad, 12005870) or HRP conjugated secondary antibody (Cell Signaling, 7074S) was used to incubate the membrane. For HRP conjugated secondary antibody incubated blots, ECL substrate (Cell Signaling,6883s) (as per manufacturers protocol) was added and imaged by ChemiDoc imaging system (Biorad). The list of primary antibodies used in the immunoblotting experiments is listed in **Table 4**.

Annexin V-PI assay

We performed Annexin V-PI assay using Dead Cell Apoptosis Kit with Annexin V Alexa Fluor 488 & Propidium Iodide (eBioSciences) to determine apoptotic cell death in cells. Briefly, cell

monolayers were detached using ice-cold PBS once washed, and a million cells were resuspended in 1 mL in 1 x annexin-binding buffer. Next, 5 µL Alexa Fluor 488 annexin V and 1 µL 100 µg / mL PI were added per 100 µL of cell suspension. Cells were incubated for 15 mins at room temperature, away from light. Finally, 400 µL 1 x annexin-binding buffer was added per 100 µL cell suspension, and samples were analyzed by BD Celesta flow cytometer immediately.

Statistics

Generation of graphs and statistical analyses were performed with Prism 9 (GraphPad). Data are presented as mean values ± S.E.M (standard error mean) unless stated otherwise. Statistical analyses between two means were done by t-test or non-parametric 2-tailed Mann-Whitney t-test. Comparisons between three or more means were done by Two-Way ANOVA with Bonferroni post-test. We performed Log-rank (Mantel-Cox) tests for survival data (*P < 0.05, **P < 0.01, ***P < 0.001, ****P < 0.0001). Statistical analyses were done with either t-test or two-way ANOVA using Bonferroni's multiple comparisons (*P < 0.05, **P < 0.01, ***P < 0.001, ****P < 0.0001). scRNA sequencing and bulk RNA sequencing analysis (GSEA, violin plots and dot plots) are analyzed using Wilcoxon rank-sum test.

Figures

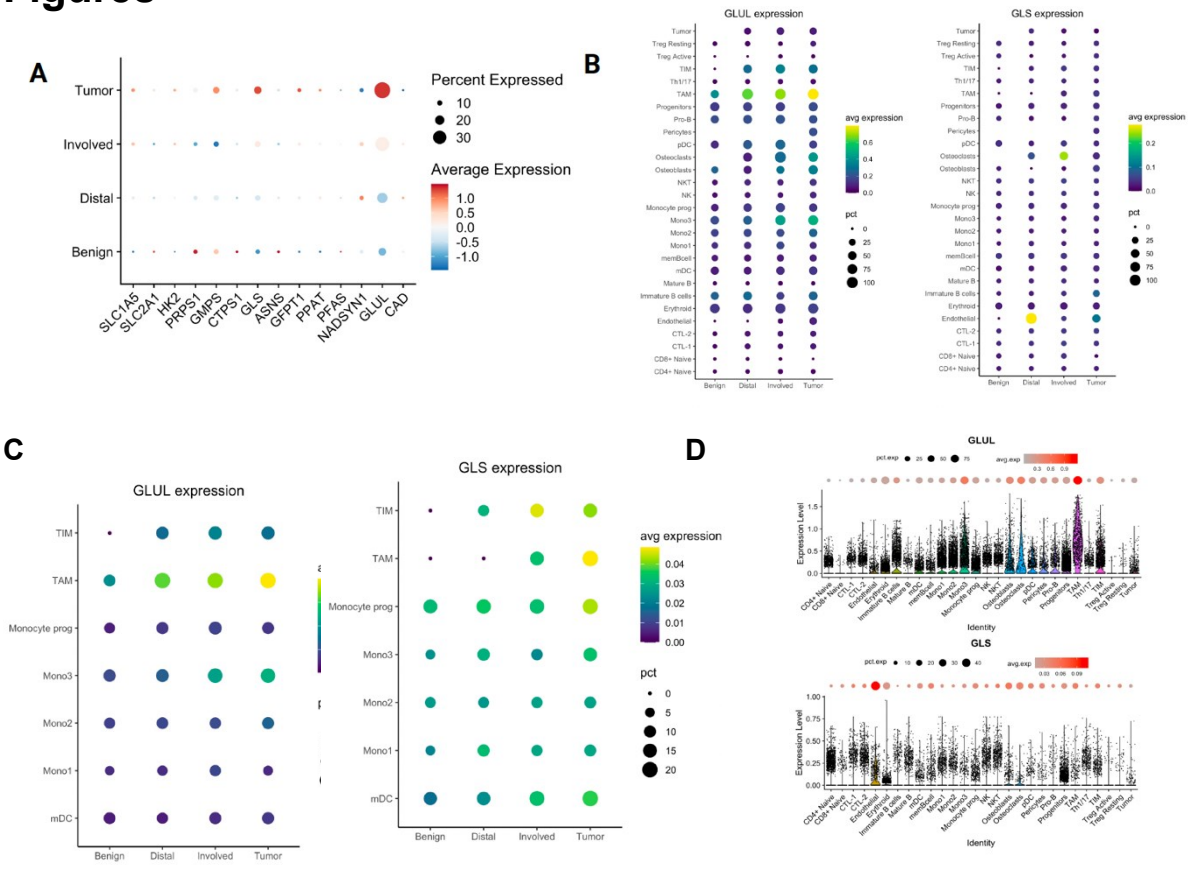

Figure 1. Enrichment of glutamine utilizing enzymes in TAMs. (A) Dot plot showing expression levels of glutamine pathway enzymes *GLUL* and *GLS* and fractional abundance of myeloid cells expressing these enzymes across samples (Tumor, Involved, Distal, Benign). **(B)** Violin plots showing the expression levels of *GLUL* and *GLS* and the fraction of cells expressing these enzymes. **(C and D)** Data for figures A and B are derived from the previously published single-cell RNA sequencing (scRNA-seq) integrated dataset from 9 metastatic PCa, and 7 benign BM control patient samples by Kfoury et al. 2021.

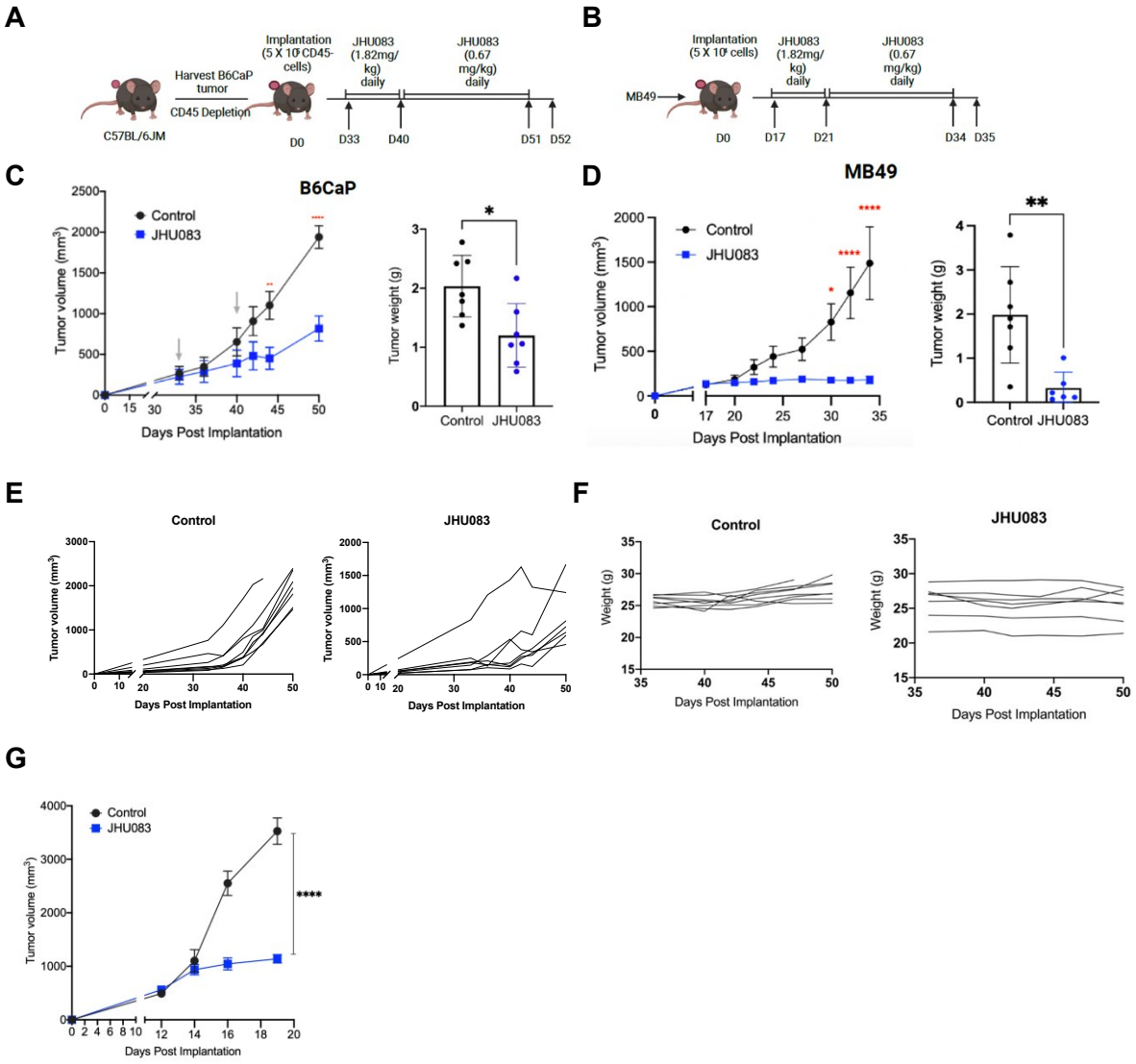

Figure 2. Anti-tumor efficacy of JHU083 in B6CaP, MB49 and RM1 xenografts. (A-B). Schematic diagram showing the heterotopic syngeneic urologic tumor models (B6CaP and MB49 tumors) and JHU083 treatment strategy. **(C-D)**. Tumor growth kinetic plots and tumor weight measurement in the B6CaP (n=8/group) and MB49 (n=9 or 10/group) tumors, respectively. **(E)**. Individual growth kinetics (tumor volumes) of control and JHU083 treated B6CaP tumors. (**F).** Animal body weights of vehicle- and JHU083-treated mice bearing B6CaP tumors throughout the therapeutic window and**(G).** Anti-tumor activity of JHU083 in RM-1 PCa tumors (n=3/ group).

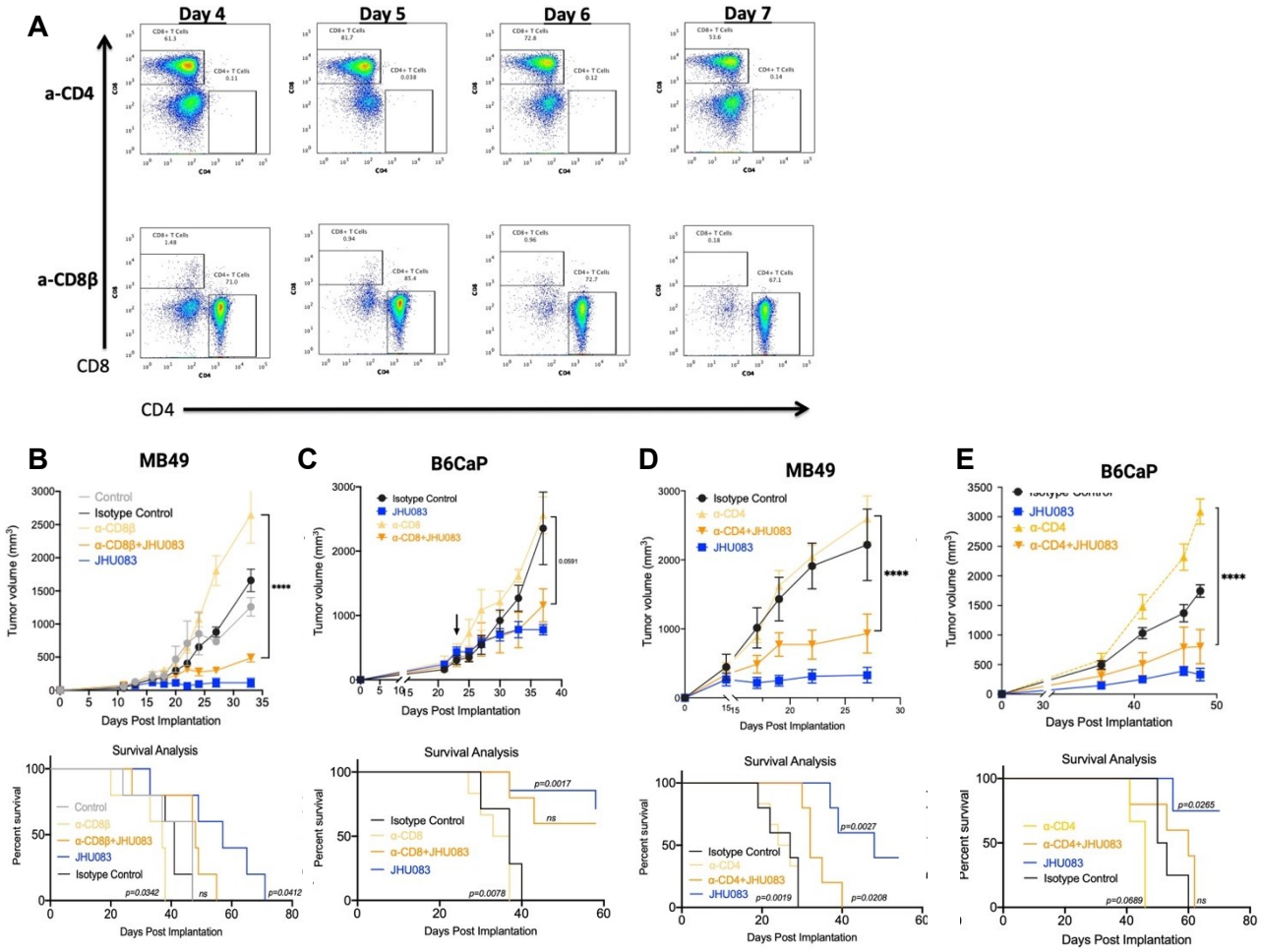

Figure 3. Anti-tumor immunity by JHU083 is less dependent on T cells. **(A)** Confirmation of anti-CD4 and anti-CD8β antibody-mediated T cell depletion in the spleen after intraperitoneal (i.p.) injections at 200 μg antibodies per treatment in C57BL/6J mice and **(B-C)** Effects of $CD8^+$ T cell depletion on tumor growth kinetics and animal survival for MB49 **(B)** (n=4-5/group) and B6CaP (n=4-6/group) **(C)** tumors, respectively. **(D-E)** Effect of $CD4^+$ T cell depletion on tumor growth kinetics of MB49 **(D)** (n=4-5/group) and B6CaP, and **(E)** (n=3-5/group) tumors and animal survival, respectively.

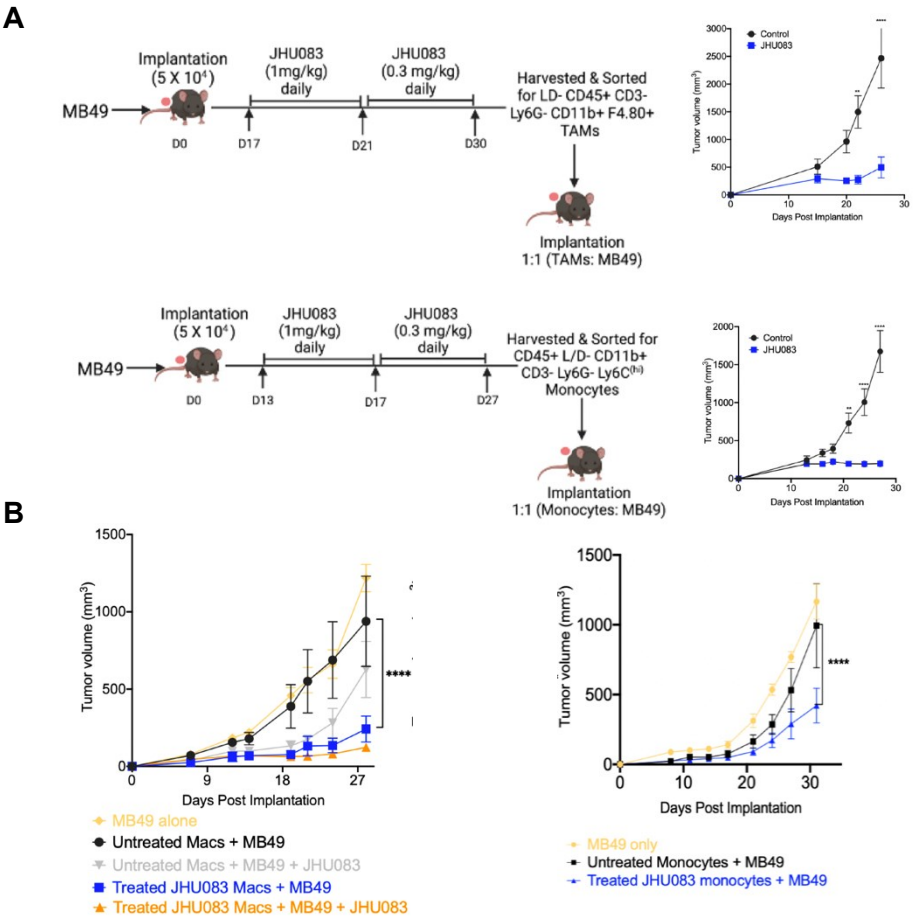

Figure 4. Anti-tumor immunity by JHU083 is myeloid cell (TAM and TIM) dependent.

(A) Schematic representation for adoptive transfer (ADT) of JHU083-treated TAMs (n=7 or 8/group) or TIMs (n=13/group) from the MB49 tumor-bearing mice and donor mice and tumor growth kinetics. **(B)** Anti-tumor activity of FACS-sorted and adoptively transferred JHU083-reprogrammed TAMs ($CD45^+$ $Ly6G^-$ $CD3^-$ $CD11b^+$ $F4.80^+$) (n=5 or 10/group), and **(C)** TIMs ($CD45^+$ $Ly6G^-$ $CD3^-Ly6C^{(hi)}$) (n=4 or 7/group) on MB49 tumor growth kinetics. Briefly, live-sorted tumor-derived TAMs or TIMs were mixed in a 1:1 ratio with wild-type MB49 cells and were used to implant flank tumors in recipient mice.

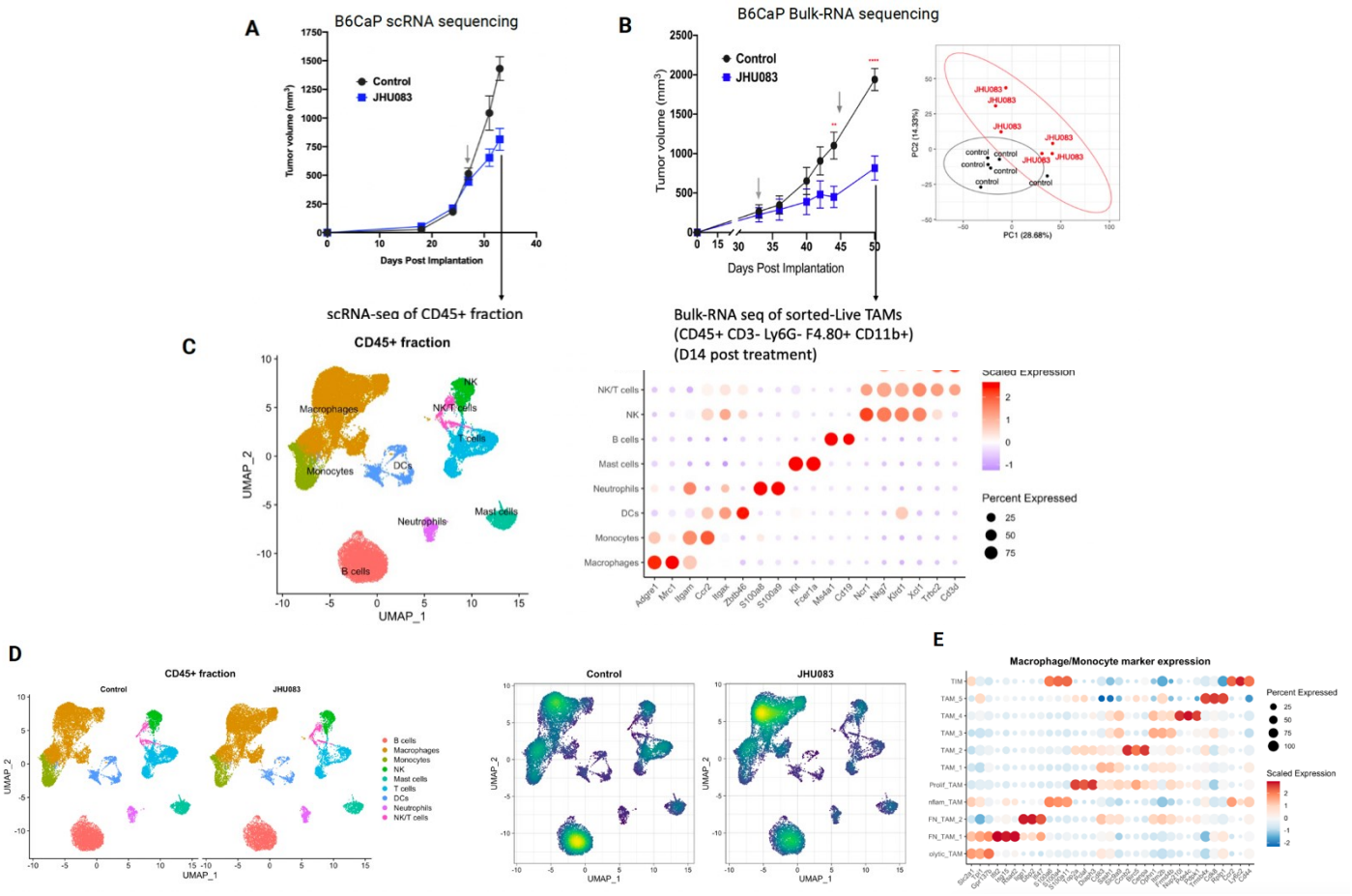

Figure 5. JHU083 transcriptomics and global changes in CD45+ cells in B6CaP. (A) Tumor growth kinetic plots of B6CaP tumors 7 days following JHU083 treatment. Briefly, control and JHU083 treated tumors were used for scRNAseq (Day 7 post-treatment) (n=6) on sorted Live $CD45^+$ cells and $CD45^-$ cells, and **(B)** at a late time point (Day 18 post-treatment) (n=6/ group) for bulk-RNA seq on sorted TAMs (Live $CD45^+$ $CD3^-$ $Ly6G^-$ $CD11b^+$ $F4.80^+$) with PCA analysis. **(C)** UMAP plots showing different immune cell clusters within the $CD45^+$ compartment from scRNAseq and dot plots showing expression levels of selected marker genes used to assign different immune cells. **(D)** UMAP plots showing identification and differential abundance of different immune cells within $CD45^+$ compartments between control vs. JHU083 treated by proportions and density. **(E)** Dot plot showing expression of selected marker genes used to assign different TAM subsets and the monocyte cluster identified within parent macrophage cluster.

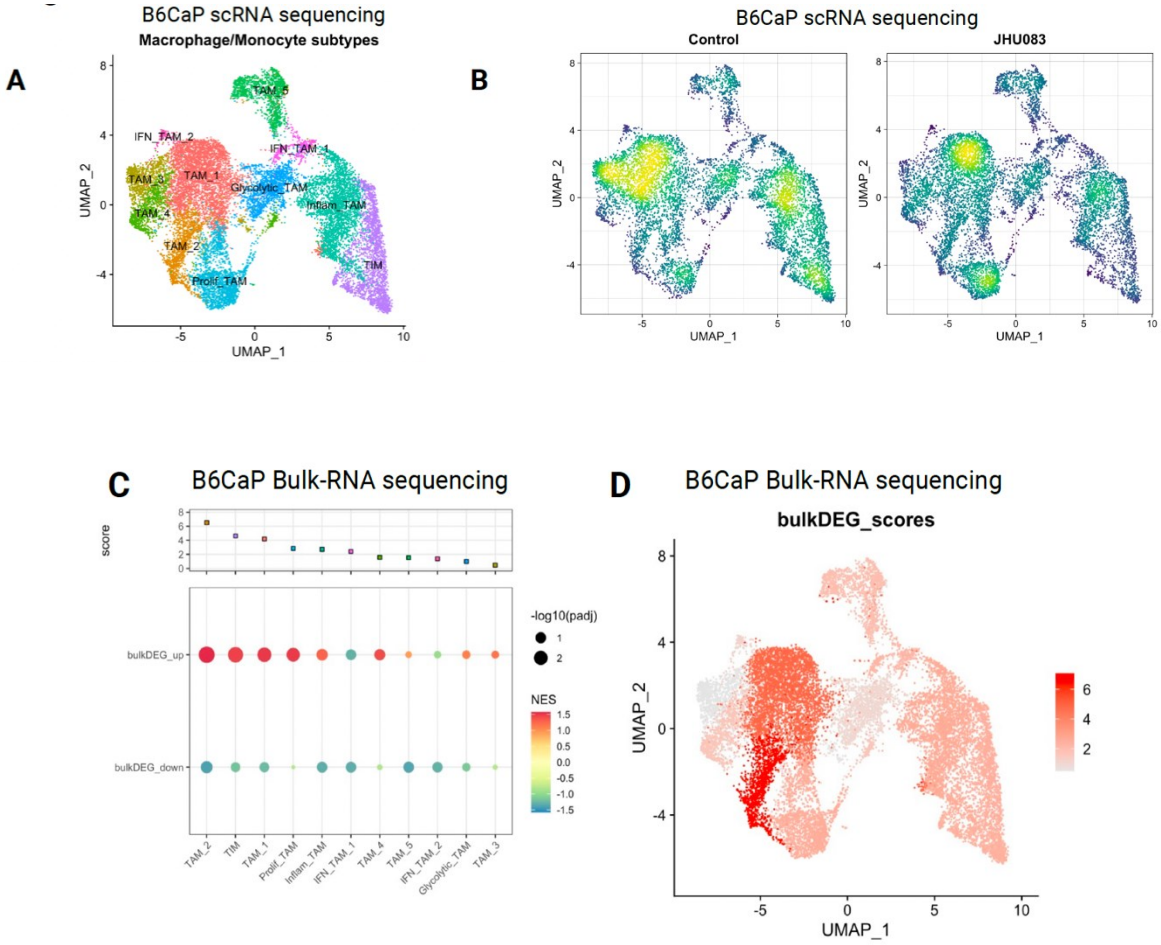

Figure 6. JHU083 induced changes in macrophage/ monocyte fraction in the TME (early and late time points). (A) UMAP plots showing different TAM and TIM clusters in B6CaP tumors at an early point with scRNA-seq (Day 7 post-treatment) (n=6) across all samples. **(B)** Density plot of different TAMs and the monocyte (TIM) clusters in control and JHU083-treated B6CaP tumors identified in figure A. **(C)** Scores plot of differential differences in each cluster between positively enriched and negatively enriched DEGs between JHU083 vs. Control at a late time point with Bulk-RNA seq on sorted TAMs from B6CaP treated tumors (Day 18 post-treatment) (n=6/ group). **(D)** UMAP plot based on the Top DEG bulk scores from **(C)** representing the differential magnitude enriched clusters based on scRNA-seq defined clusters in JHU083 vs. Control.

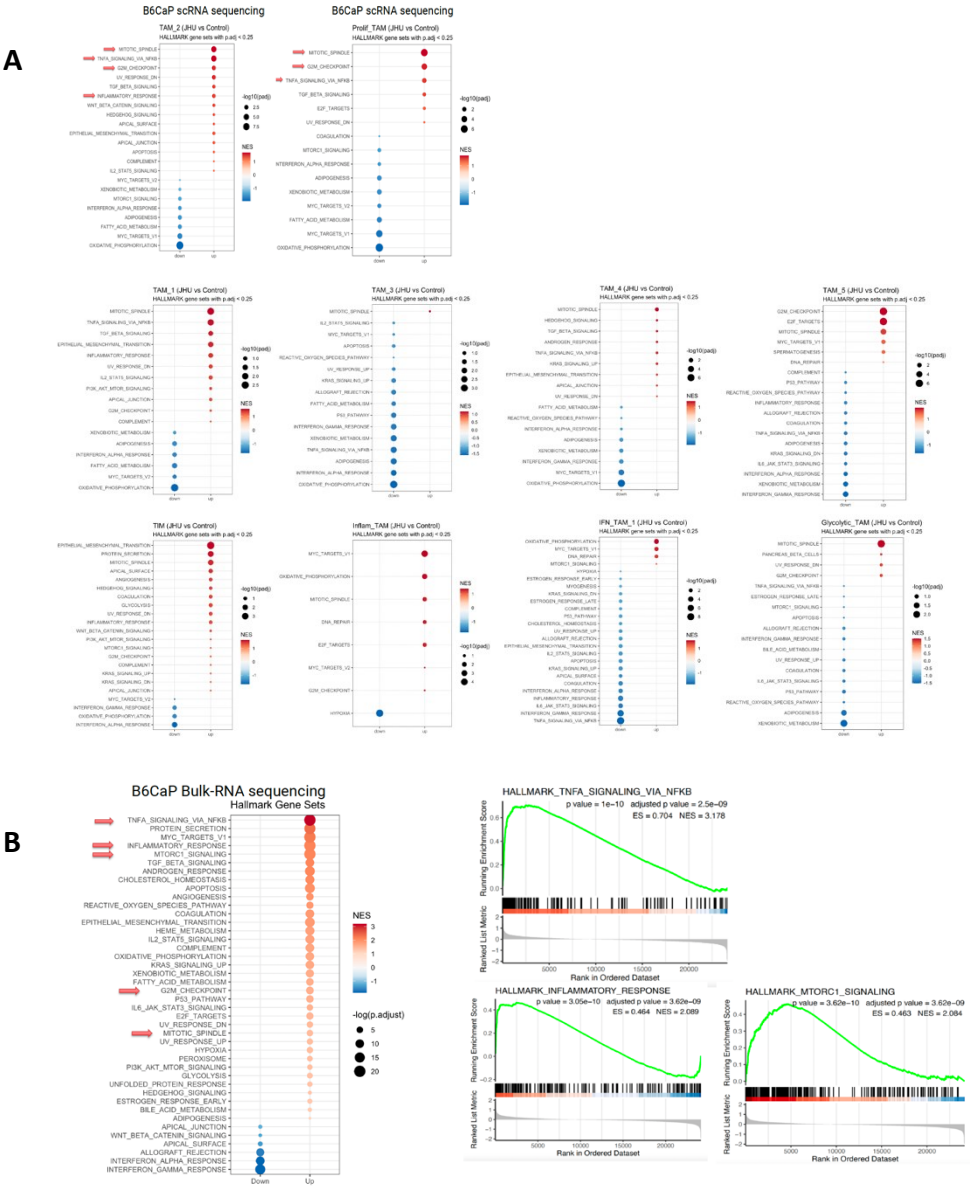

Figure 7. Pathway enrichment analysis in scRNA sequencing. (A). GSEA comparison between proliferative TAMs and TAM1 in JHU083 treated vs. control samples from scRNA sequencing in different Macrophage/Monocyte clusters (Day 7 post-treatment). **(B)** GSEA of top DEGs JHU083 treated vs. control from Bulk-RNA seq on sorted TAMs from B6CaP treated tumors (Day 18 post-treatment) (n=6/ group) and GSEA pathway enrichment for the Hallmark TNFA_signaling_via_NfKb, Inflammatory_response, mTORC1_signaling in genes upregulated after JHU083-treatment in DEGs from bulk RNA seq data from TAMs.

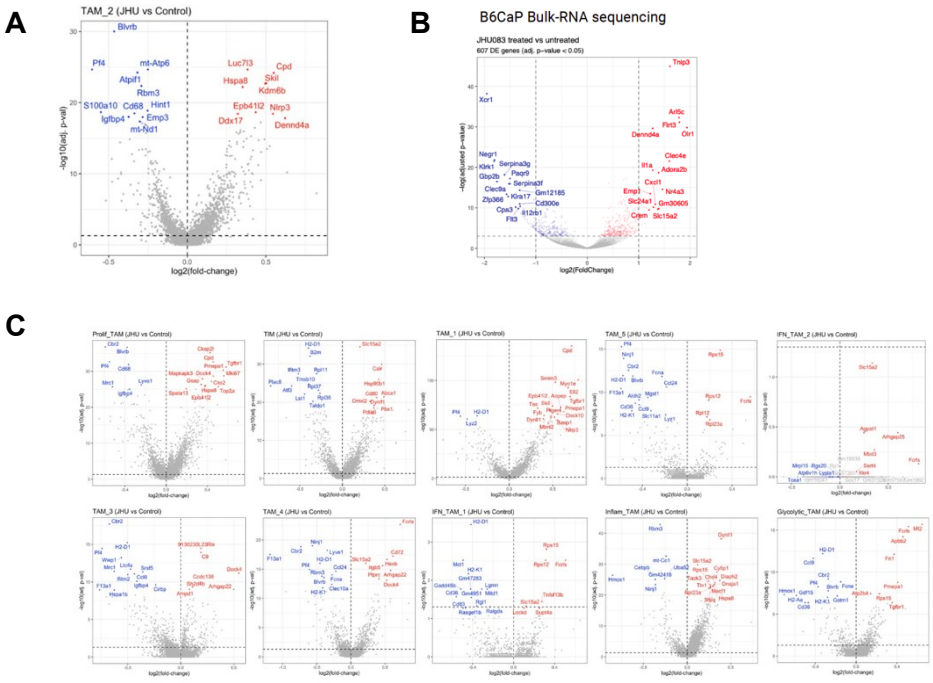

Figure 8. Top DEGs after JHU083 treatment in TAMs. (A) Volcano plot of top DEGs from TAM2 cluster between JHU083 treated vs. control in scRNAseq**, (B)** Volcano plot of top DEGs between JHU083 vs. control from Bulk-RNA seq data **(C)** Volcano plots representing top DEGs from the rest of the clusters in TAMs/ monocyte clusters identified in JHU083 vs. control**.**

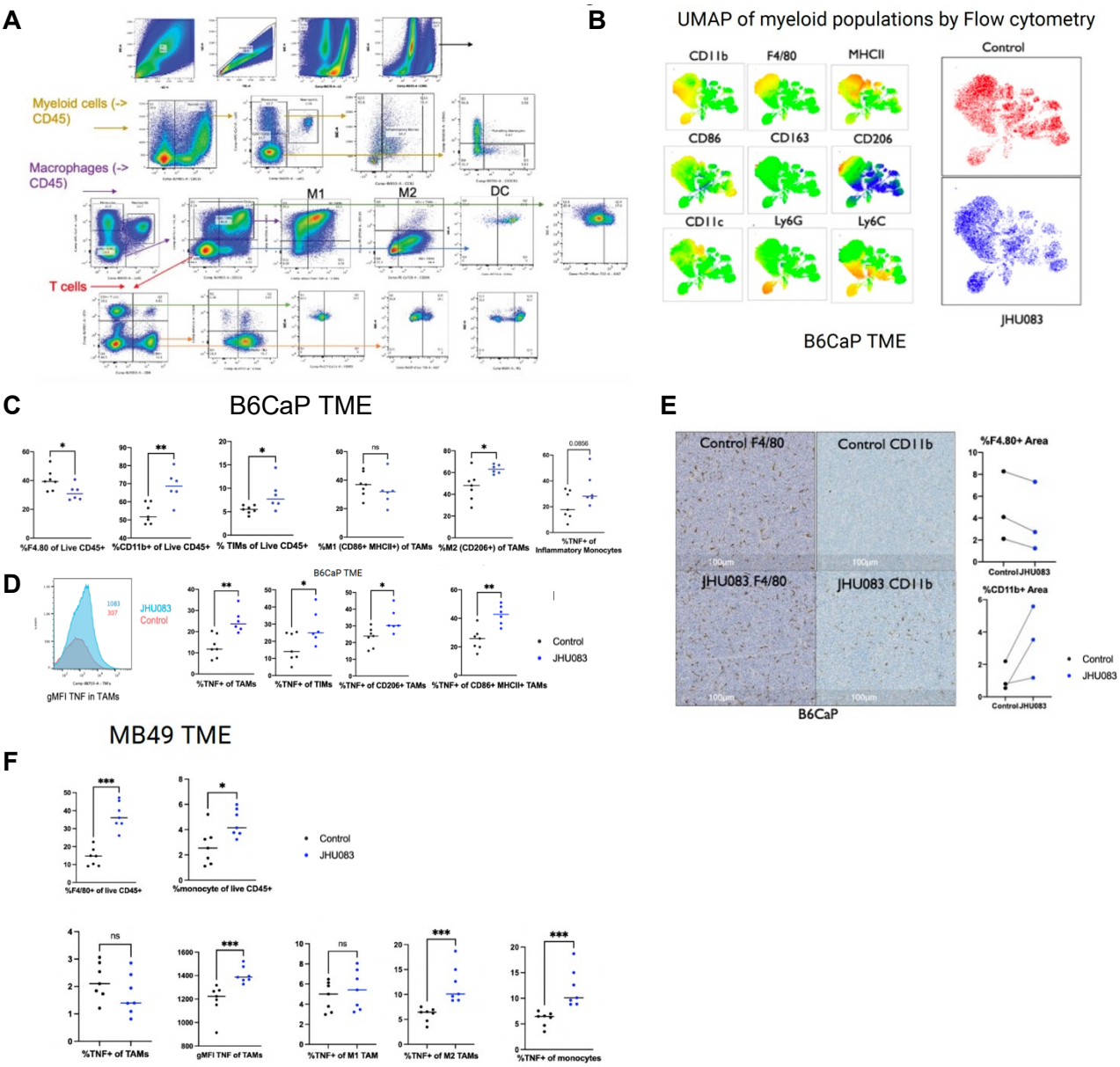

Figure 9. JHU083 induced myeloid reprogramming by TNF signaling. (A) Gating schematic utilized for flow cytometry-based analyses in both tumor types (MB49 and B6CaP) for surface and intracellular expression of phenotypic markers. **(B)** UMAP plots showing representation after flow-cytometry analyses of different myeloid fractions and their differential abundance in JHU083-treated vs. control B6CaP tumors. **(C)** Surface and intracellular expression of different immune subpopulations in B6CaP tumors in control vs. JHU083-treated samples**. (D)** The geometric mean of TNF of a representative TAM population in control vs. JHU083-treated samples. **(E)**

Representative immunohistochemistry (IHC) images and quantification of F4/80 and CD11B in three independent experiments B6CaP tumors (n=3/group) and **(F)** Surface expression and intracellular expression of myeloid cells subpopulations in MB49 tumors (n=7/ group).

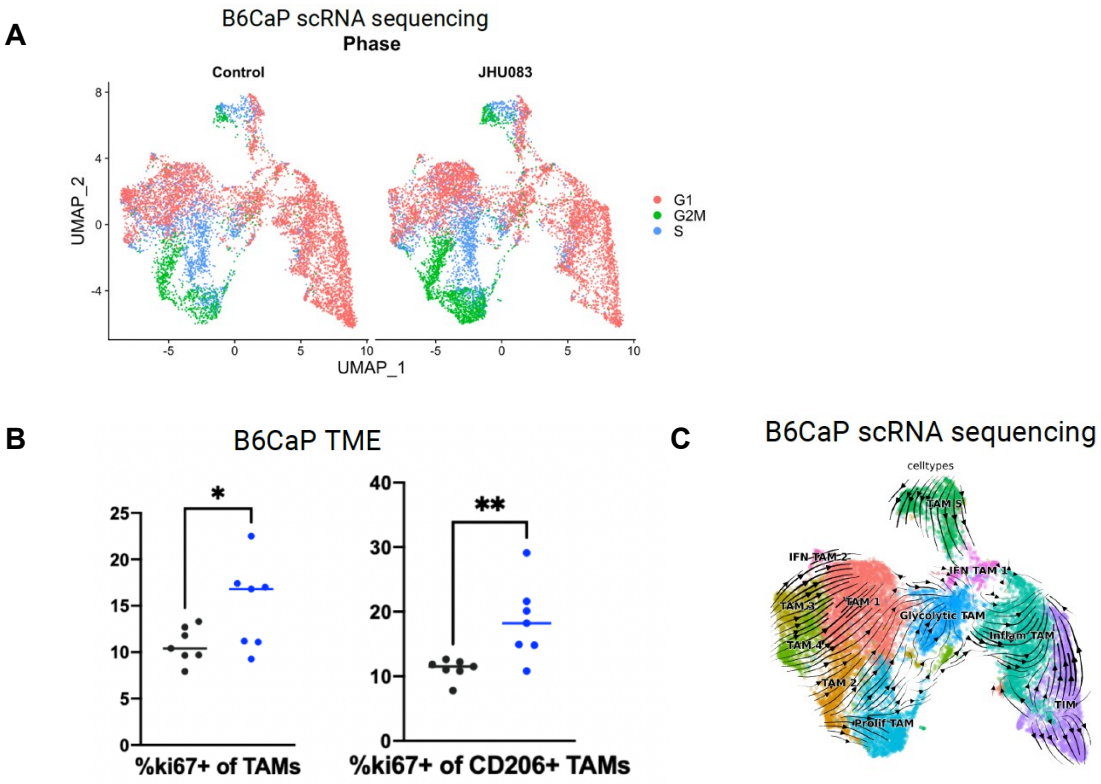

Figure 10. JHU083 increased proliferation in tissue-resident TAMs. (A) UMAP of cell cycle genes (G1, G2M, and S phase), **(B)** Intracellular expression of % ki-67+ TAMs in JHU083 treated TAMs vs. control B6CaP tumors, and (**C)** RNA velocity of clusters from (A) overlaid with RNA velocity stream.

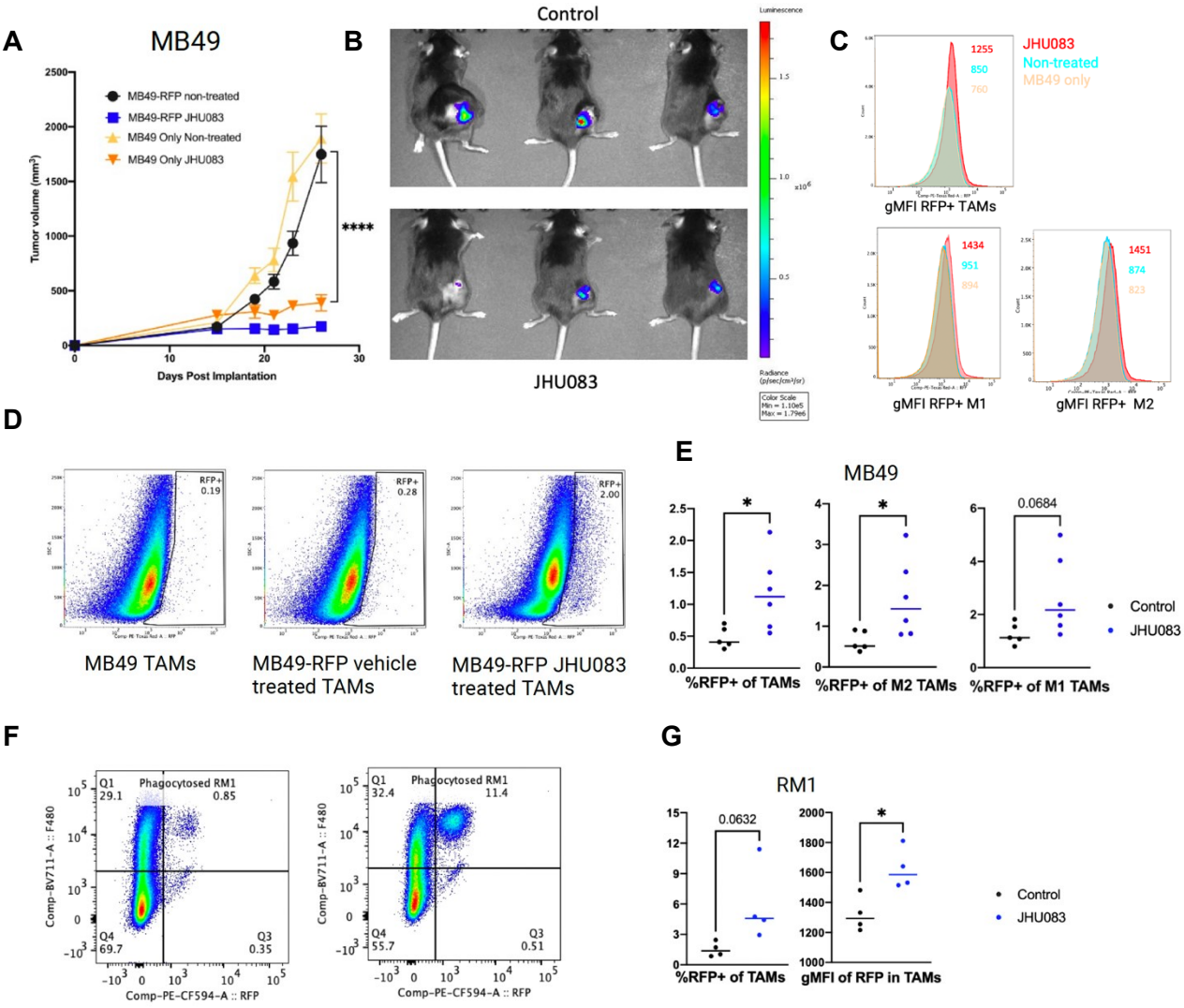

Figure 11. JHU083 induces in vivo phagocytosis of tumor cells. (A) Tumor growth kinetics of MB49 tumors in different conditions. JHU083 treatment decreases tumor growth in MB49-RFP$^+$ tumors relative to non-treated (n=5 or 6/ group) tumors. **(B)** IVIS quantification of tumor growth by luciferase in MB49-RFP+ tumors. **(C)** RFP gMFI expression in TAMs, M1 TAMs, and M2 TAMs. **(D)** Representative flow plots of RFP$^+$ MB49 tumor cells in JHU083 treated TAMs relative to vehicle-treated samples. **(E)** % RFP+ cells of TAMs, CD206$^+$ TAMs (M2), and CD86$^+$ MHCII$^+$ TAMs (M1). **(F)** Representative flow plots of RFP+ RM1 tumor TAMs % RM1-RFP+ cells, and **(G)** corresponding mean fluorescence intensity(gMFI) of TAMs (n=4/group).

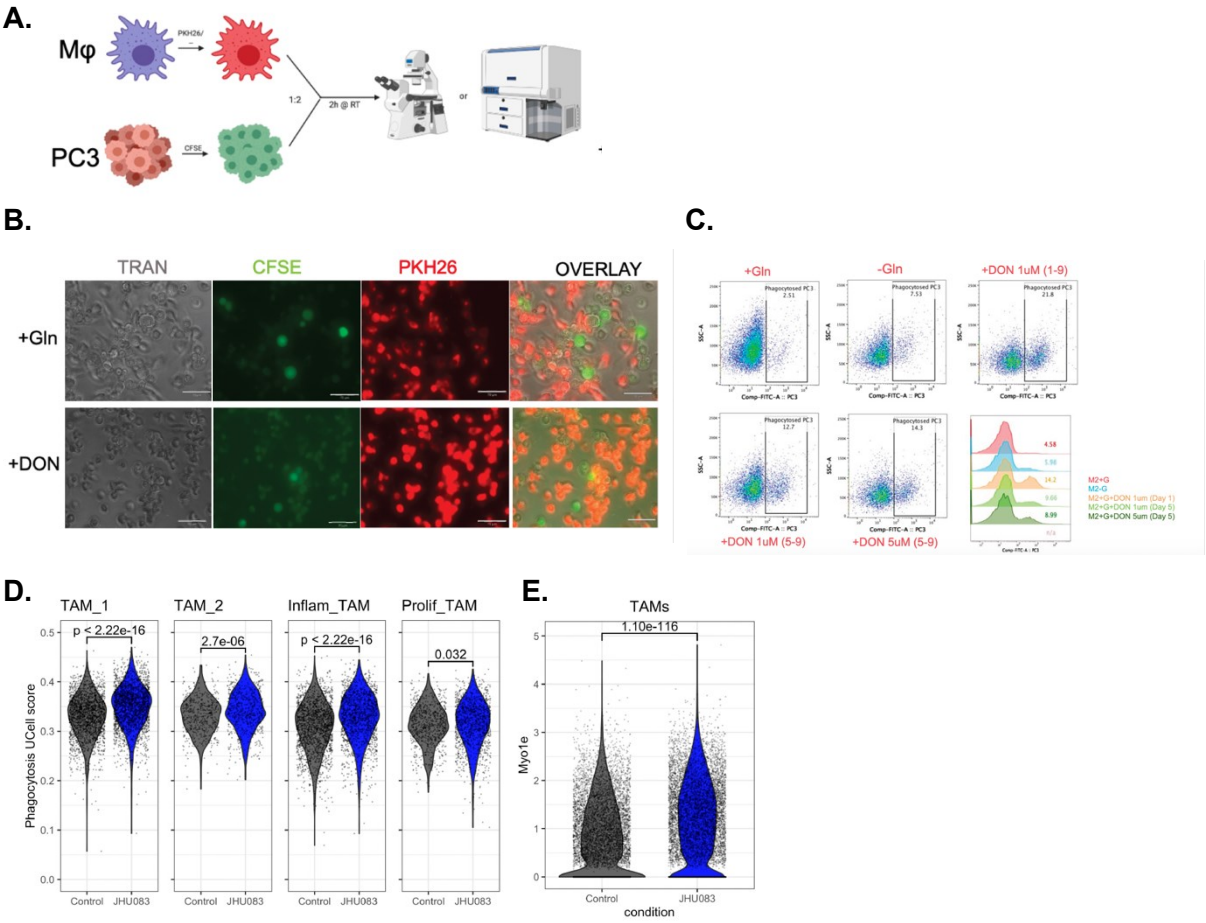

Figure 12. JHU083 increased phagocytic potential of macrophages. **(A)** Schematic diagram showing the determination of the phagocytic activity of TAMs. Briefly, DON-treated PBMC-derived macrophages were co-cultured with CFSE-labeled PC3 cells, and phagocytic activity was determined using flow cytometry. **(B)** Increased phagocytosis in DON-treated macrophages co-cultured with CFSE-labelled PC3 by immunofluorescence microscopy, and **(C)** quantification using flow cytometry. **(D)** Violin plots of Phagocytosis UCell scores on TAM_1, TAM_2, Inflam_TAM, and Prolif_TAM (Wilcoxon rank-sum test) from scRNA sequencing in B6CaP tumors (n=3/ group) **(E)** Violin plot for Myo1e expression in all TAMs in B6CaP-derived TAMs identified in scRNAseq analysis.

A.

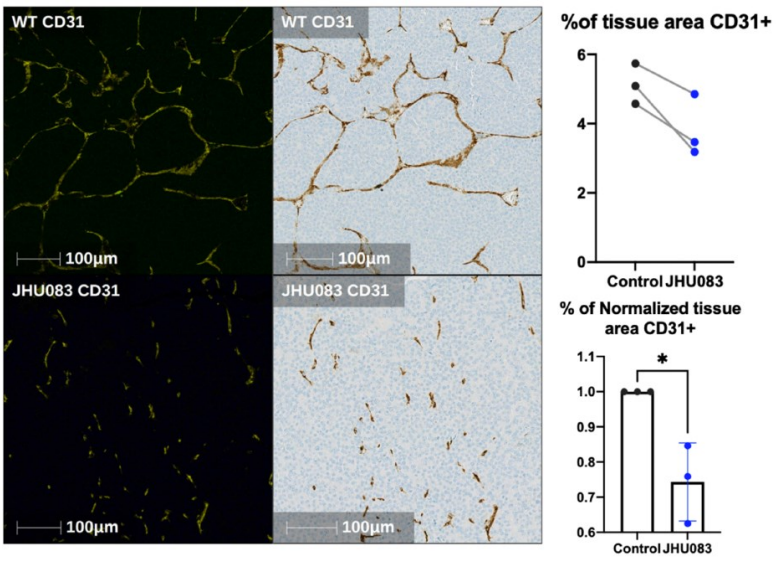

B.

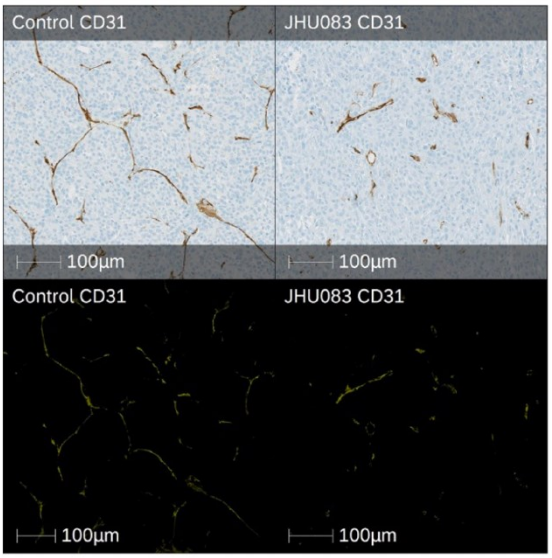

Figure 13. JHU083 affects tumor angiogenesis. (A) Immunohistochemical (IHC) quantification of CD31 intensity in B6CaP tumors (n=3/ group), and **(B)** IHC quantification of CD31 intensity in MB49 tumors.

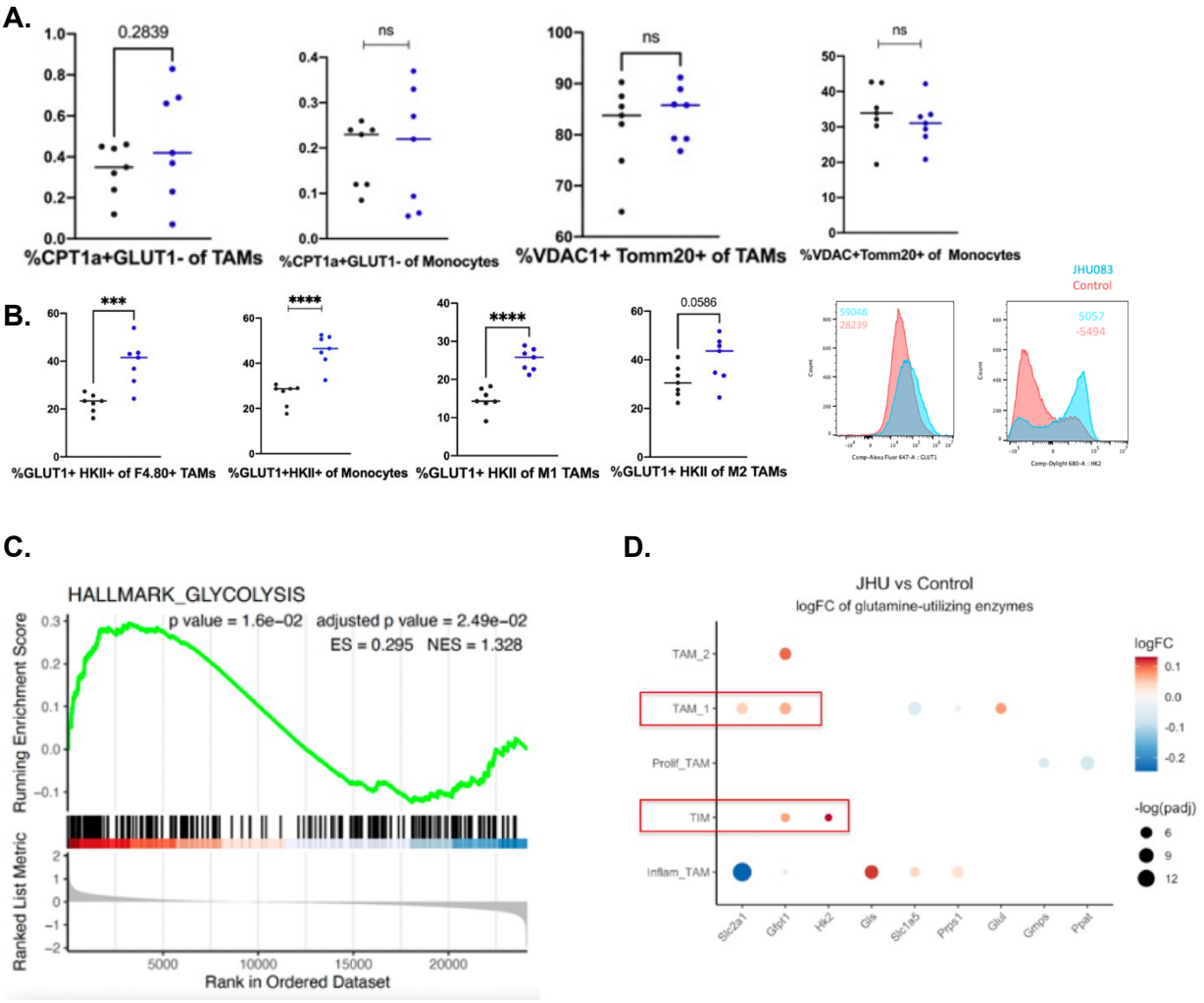

Figure 14. JHU083 increases glycolysis in TAMs. (A) Percentage of CPT1α+, VDAC1 TOMM20+ cells in TAMs and TIMs in B6CaP tumors (n=8/group). **(B)** Surface and intracellular expression of GLUT1 and HKII (percentage positive population and mean fluorescence intensity) on B6CaP-derived TAMs (n=8/group). **(C)** GSEA pathway enrichment for glycolysis in genes upregulated after JHU083 treatment in FACS-sorted B6CaP-derived TAMs, and **(D)** Log fold-changes of glutamine utilizing at early time point from macrophage/monocyte sub-clusters from scRNA sequencing data.

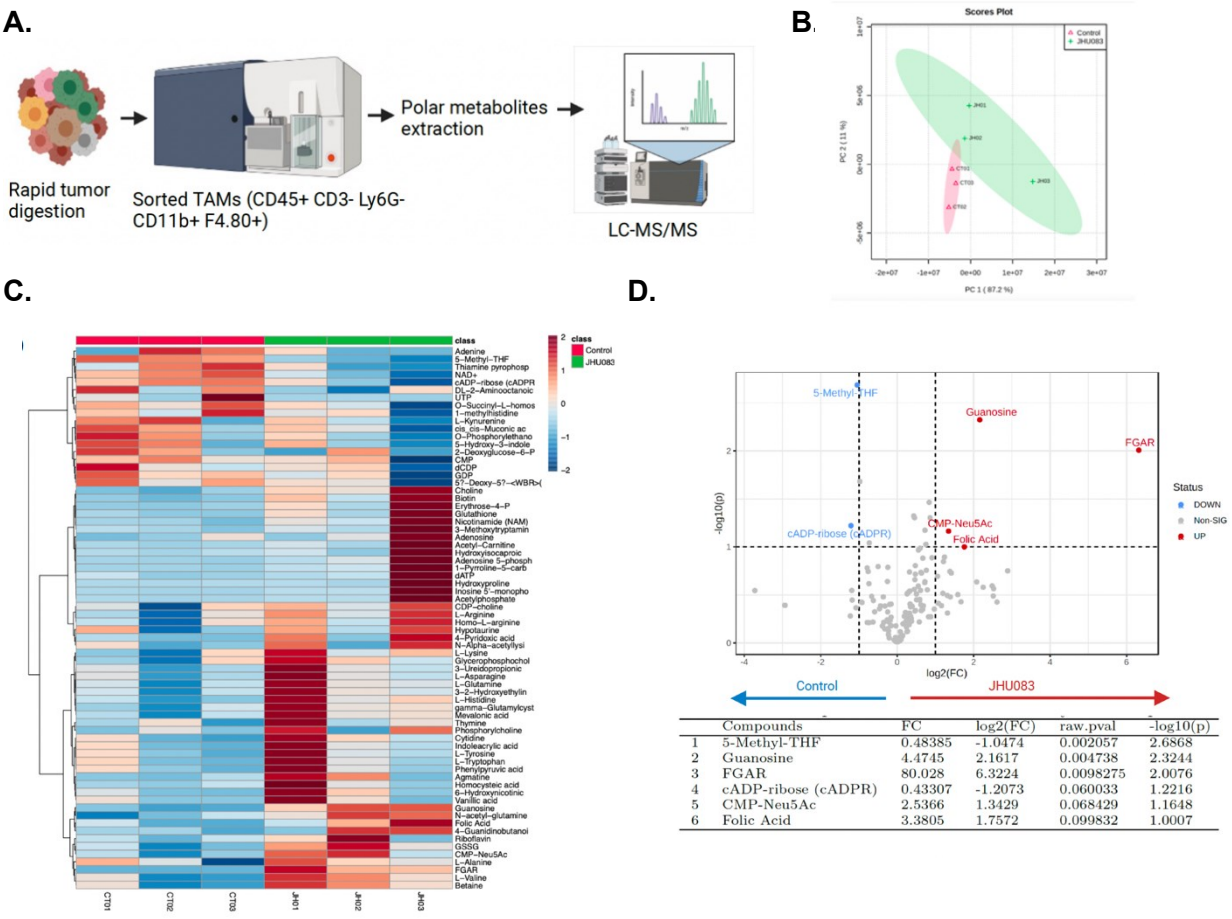

	Compounds	FC	log2(FC)	raw.pval	-log10(p)
1	5-Methyl-THF	0.48385	-1.0474	0.002057	2.6868
2	Guanosine	4.4745	2.1617	0.004738	2.3244
3	FGAR	80.028	6.3224	0.0098275	2.0076
4	cADP-ribose (cADPR)	0.43307	-1.2073	0.060033	1.2216
5	CMP-Neu5Ac	2.5366	1.3429	0.068429	1.1648
6	Folic Acid	3.3805	1.7572	0.099832	1.0007

Figure 15. JHU083 induces metabolic changes in purine metabolism. (A) Schematic diagram showing sample preparation for in vivo tracing of U-13 glucose in TAMs after rapid digestion and FACS-sorting. **(B)** PCA analysis of TAMs for targeted metabolite analysis with LC-MS/MS (n=3/group). **(C)** Heat map showing the differential metabolites in TAMs sorted from JHU-treated and control B6CaP tumors (n=3/group), and**(D)** Volcano plot showing fold changes in metabolite abundance in one-carbon metabolism, purine nucleotide metabolism, and hexosamine pathway in JHU083-treated vs. control TAMs.

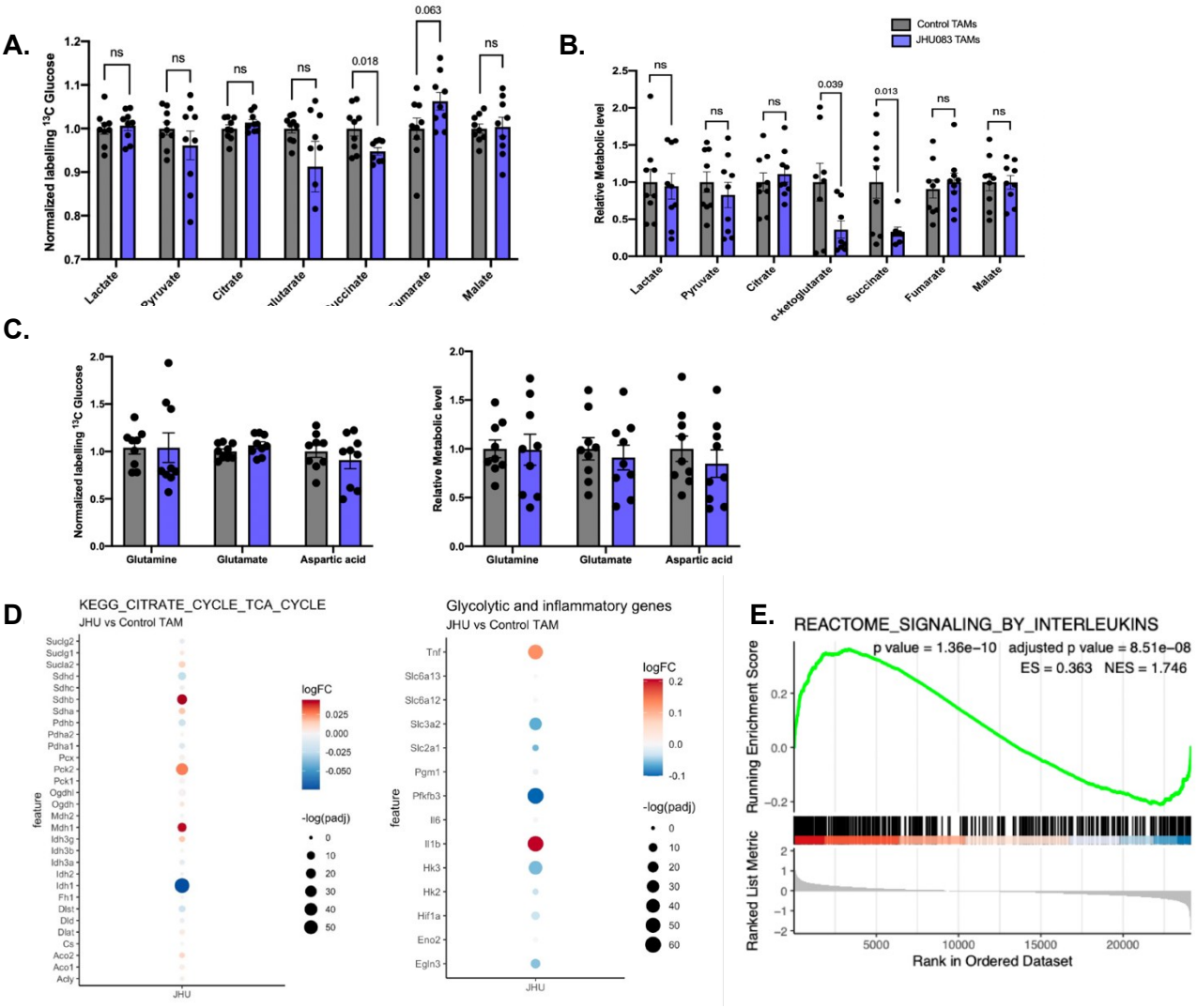

Figure 16. JHU083 promotes TCA cycle break by succinate shunting in TAMs. (A) Normalized relative labeled metabolites from U-^{13}C glucose in TCA cycle in TAMs derived from B6CaP tumors (n=9/group in 2 independent experiments). **(B)** Normalized relative metabolite abundances in TCA cycle in TAMs derived from B6CaP tumors (n=9/group in 2 independent experiments). **(C)** Normalized relative labeled metabolites and their abundances from U-^{13}C glucose in amino acids in TAMs derived from B6CaP tumors (n=9/group in 2 independent experiments).**(D)** Log fold-change of TCA cycle enzymes and inflammatory cytokine transcript in TAMs (from scRNA sequencing at an early time point (D7 post-treatment), and **(E)** GSEA pathway enrichment for the Reactome Signaling by Interleukins from DEGs identified in bulk-RNA seq data in B6CaP sorted TAMs.

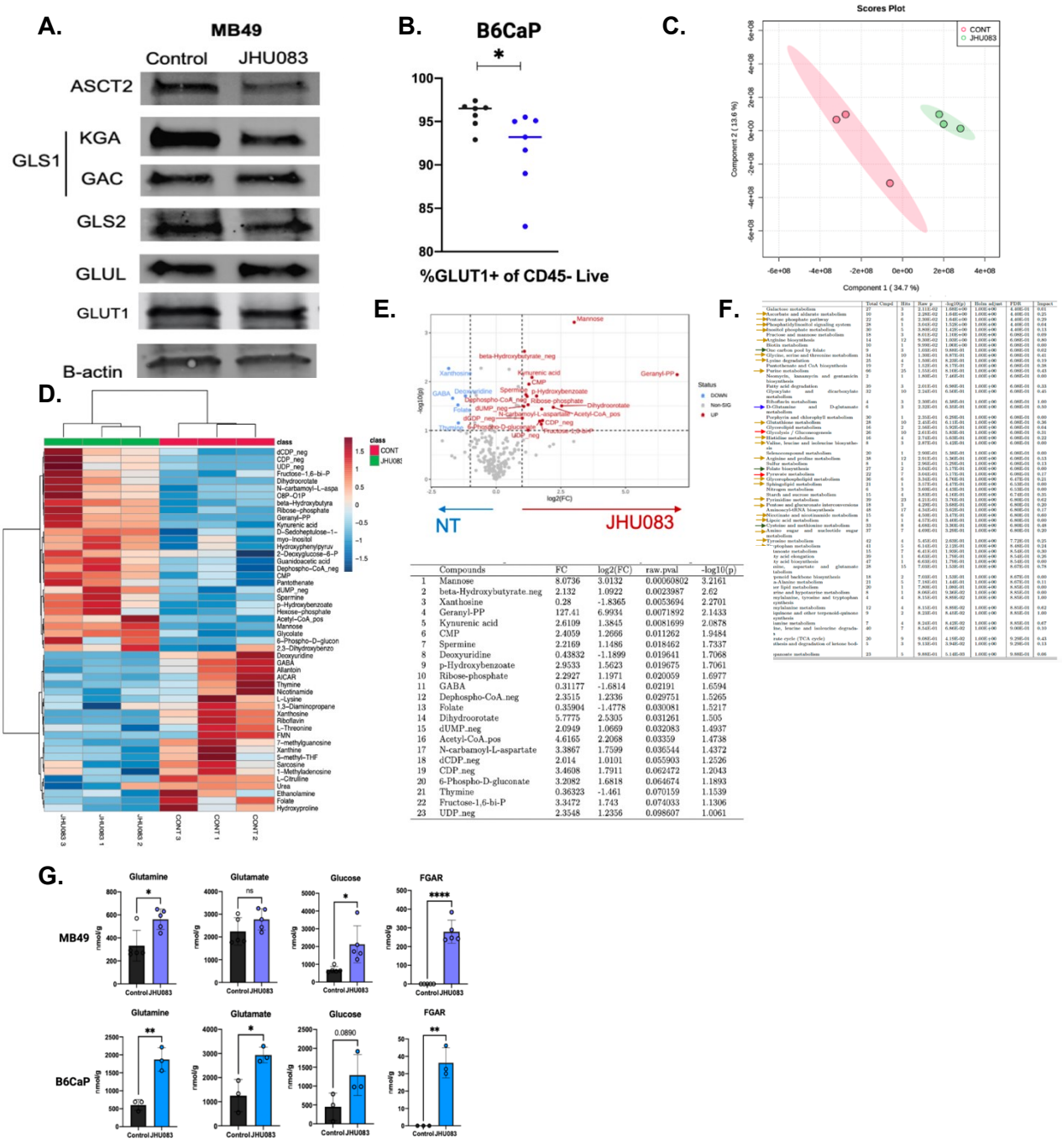

	Compounds	FC	log2(FC)	raw.pval	-log10(p)
1	Mannose	8.0736	3.0132	0.00060802	3.2161
2	beta-Hydroxybutyrate_neg	2.132	1.0922	0.0023987	2.62
3	Xanthosine	0.28	-1.8365	0.0053694	2.2701
4	Geranyl-PP	127.41	6.9934	0.0071892	2.1433
5	Kynurenic acid	2.6109	1.3845	0.0081699	2.0878
6	CMP	2.4059	1.2666	0.011262	1.9484
7	Spermine	2.2169	1.1486	0.018462	1.7337
8	Deoxyuridine	0.43832	-1.1899	0.019641	1.7068
9	p-Hydroxybenzoate	2.9533	1.5623	0.019675	1.7061
10	Ribose-phosphate	2.2927	1.1971	0.020059	1.6977
11	GABA	0.31177	-1.6814	0.02191	1.6594
12	Dephospho-CoA_neg	2.3515	1.2336	0.029751	1.5265
13	Folate	0.35904	-1.4778	0.030081	1.5217
14	Dihydroorotate	5.7775	2.5305	0.031261	1.505
15	dUMP_neg	2.0949	1.0669	0.032083	1.4937
16	Acetyl-CoA_pos	4.6165	2.2068	0.03359	1.4738
17	N-carbamoyl-L-aspartate	3.3867	1.7599	0.036544	1.4372
18	dCDP_neg	2.014	1.0101	0.055903	1.2526
19	CDP_neg	3.4608	1.7911	0.062472	1.2043
20	6-Phospho-D-gluconate	3.2082	1.6818	0.064674	1.1893
21	Thymine	0.36323	-1.461	0.070159	1.1539
22	Fructose-1,6-bi-P	3.3472	1.743	0.074033	1.1306
23	UDP_neg	2.3548	1.2356	0.098607	1.0061

Figure 17. JHU083 affects global metabolism in urologic tumor cells. (A) Western blot of glutamine synthesizing/ utilizing enzymes and transporters in CD45$^-$ fraction of MB49 tumors. **(B)** %GLUT1+ CD45- live cells by flow cytometry in B6CaP tumors (n= 7/group). **(C)** PCA analysis of B6CaP tumors submitted for LC/MS-MS analysis. **(D)** Targeted Metabolomic analysis of B6CaP tumors by LC-MS/MS (n=3/group). **(E)** Volcano plot of JHU083 treated vs. non-treated control

tumor metabolomic analysis. **(F)** Pathway analysis of differential metabolites upregulated by JHU083 treated B6CaP tumors, and **(G)** Absolute quantification of metabolites by LC/MS-MS (n=3 or 5/group).

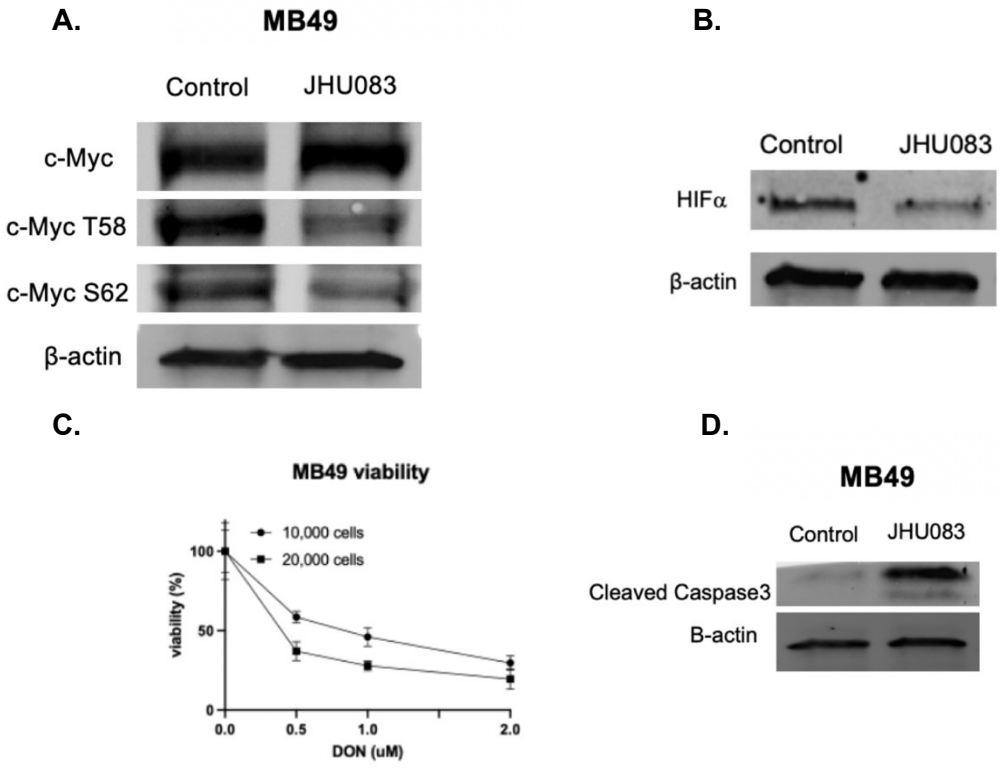

Figure 18. JHU083 induces cell death in urologic tumors. **(A and B)** Western blot quantification of c-MYC and phospho-c-MYC and HIF-α, and (**C and D**) MTT assay in DON-treated MB49 cells and Western blot cleaved caspase-3 quantification in CD45- fraction MB49 tumors.

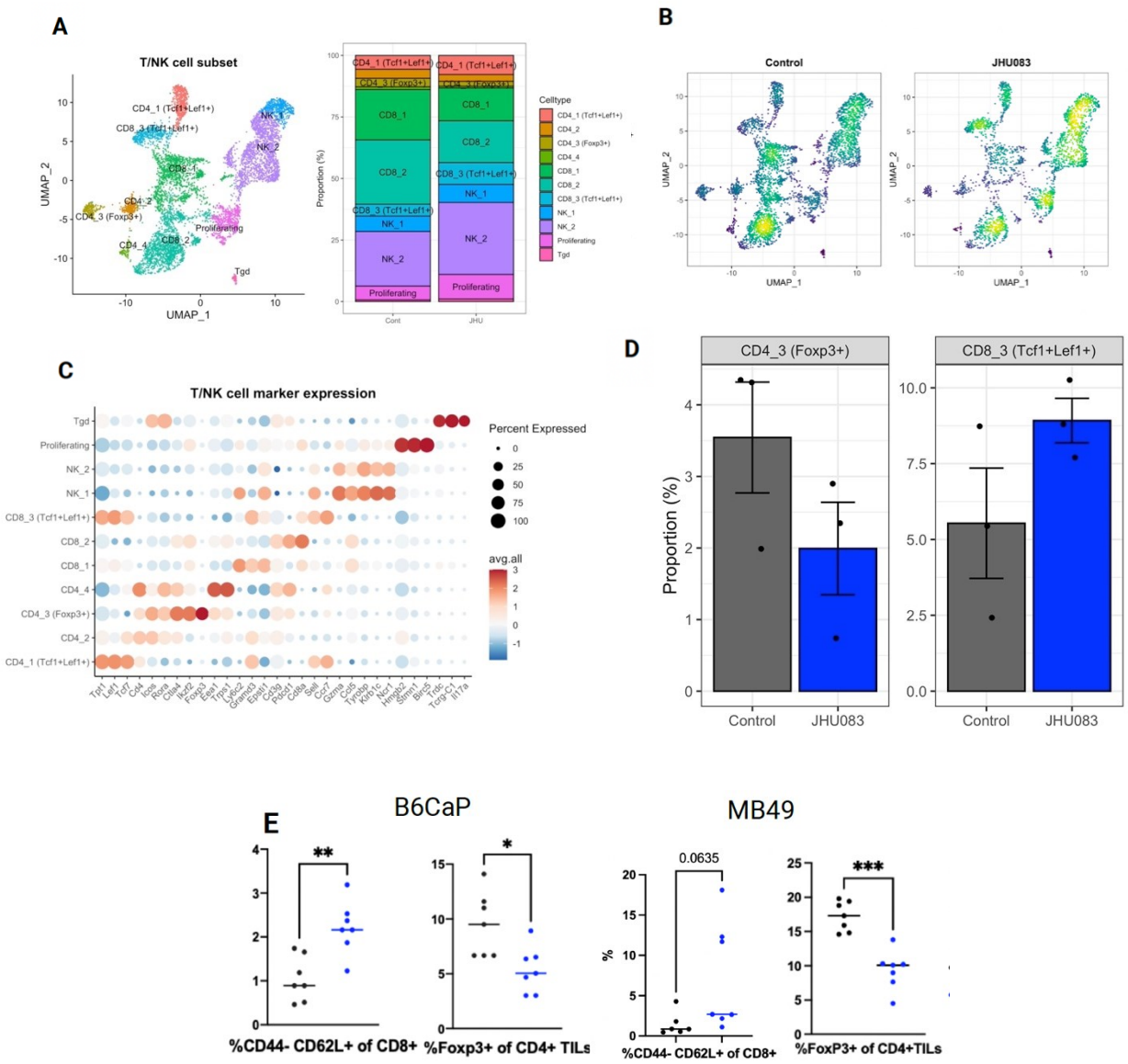

Figure 19. JHU083 induces long-lived T cell markers and affects immunosuppressive Tregs in the TME. (A) UMAP of lymphocytes from scRNA seq in B6CaP tumor-bearing mice treated with JHU083 vs. Control **(B)** Density plots of all NK and T cells based on UMAP **(C)** Dot plots of normalized expression of selected marker genes in T and NK cells subsets identified in A **(D)** Changes in proportions of NK cell subsets, Stem cell CD8 T cell, and CD4 Tregs from scRNA sequencing (n=3/group) **(E)** Surface expression and intracellular expression of Stem-like CD8 T cells and Foxp3 % positive population in B6CaP as well as MB49 TME (n=7/8).

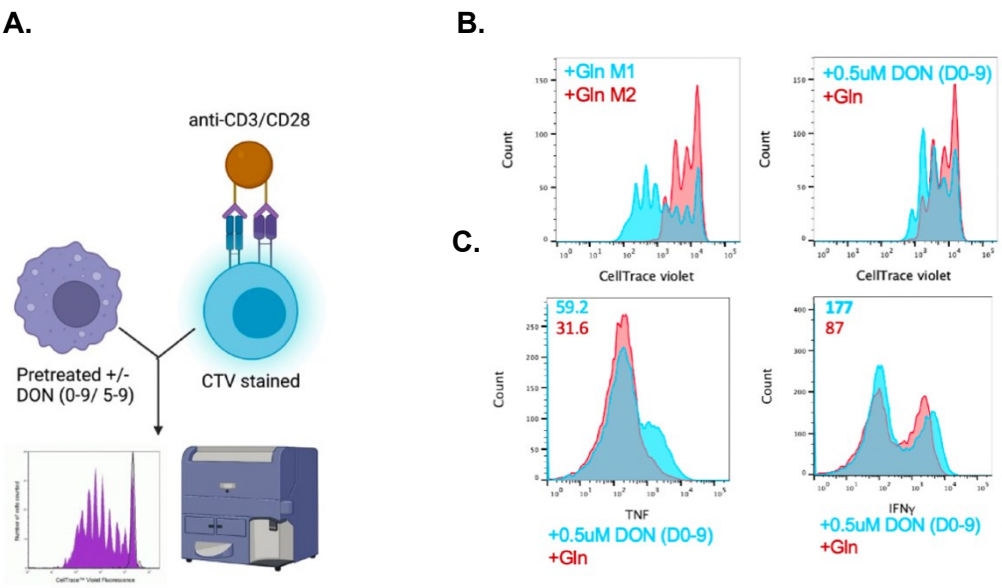

Figure 20. JHU083-treated macrophages promote polyfunctionality in CD8+ T cells

(A) Schematic workflow representation of T cell co-culture with DON-pretreated macrophages. **(B)** Proliferation was measured in CD8 T cells isolated from PBMCs and co-cultured with PBMC-derived macrophages pretreated with DON either during differentiation (Day 0-9) or during polarization (5-9) and **(C)** gMFI of TNF and IFNy in co-cultured CD8 T cells with pre-treated macrophages with DON.

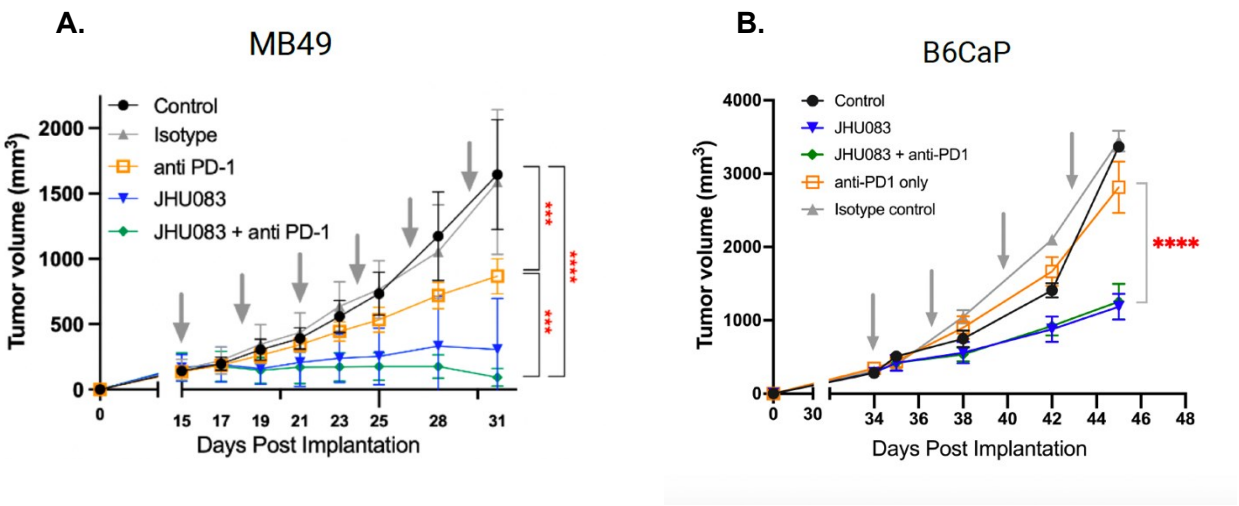

Figure 21. JHU083 synergy with anti-PD1 in myeloid-rich urologic tumors. (A and B) Tumor growth kinetics of palpable MB49 and B6CaP tumor-bearing C57BL/6J mice injected i.p. every 3rd day with anti-PD1 alone or in combination with daily oral gavage of JHU083 was measured. Data are presented as mean values ± S.E.M. Statistical analyses done with two-way ANOVA using Bonferroni's multiple comparisons (*P < 0.05, **P < 0.01, ***P < 0.001, ****P < 0.0001).

Table 1: Immunotherapy related clinical trials in urothelial cancers and metastatic castration-resistant prostate cancers. (OS= Overall survival rate) [1]

Disease	Treatment	Sample (n)	Results
mCRPC (progressed post-docetaxel)	Ipilimumab	399	No significant difference
Advanced urothelial carcinoma	Pembrolizumab alone or with combination	1010	No significant difference
mCRPC	Ipilimumab	799	Increase only in OS
mCRPC	Pembrolizumab	258	14.1 months of increase in OS
mCRPC	Nivolumab + Ipilimumab	90	19.0 increase in OS
Advanced or metastatic urothelial carcinoma	Ramucirumab	530	5.1 month increase in OS
mCRPC	Atezolizumab with enzalutamide	759	Ongoing study
mCRPC	Pembrolizumab + Docetaxel	1000	Ongoing study

Table 2. List of antibodies used in flow cytometry experiments and FACs sorting.

Marker	Fluorophore	Vendor	Cat #
CD206	PE CF594	BD	141732
CD86	Pe/Cy5	Biolegend	105016
CD62L	PECy7	BD	560516
CD11b	AF700	Biolegend	101222
CD4	APC Cy7	BD	565650
Ly6G	efluor 450	ThermoFisher	48-5931-82
CD44	BV480	BD	566200
TCRb	BV510	BD	563221
CD45	Pacific Orange	Invitrogen	MCD4530
Ly6c	BV570	Biolegend	128030
PD1	BV605	Biolegend	135220
CD8	BV650	Biolegend	100742
MHCII	BV711	Biolegend	107643
CD11c	BV750	Biolegend	117357
F4/80	BV785	Biolegend	123141
CD163	PE	ThermoFisher	12-1631-82
CPT1a	AF488	Abcam	ab171449
VDAC1	AF532	Abcam	ab14734
FOXP3	PerCpCy5.5	ThermoFisher	45-5773-82
Ki67	PerCp-eFluor710	ThermoFisher	46-5698-82
GLUT1	AF647	Abcam	ab195020
Hexokinase II	Dylight680	Abcam	ab228819
Tomm20	AF405	Abcam	ab210047

CD45	V510	Biolegend	103138
CD11b	UV805	BD	741934
F4/80	V711	BD	565612
MHCII	UV395	BD	743876
CX3CRI	V786	Biolegend	149029
CD206	PE-Cy7	Biolegend	141720
CD163	PE Dazzle	Biolegend	155316
CD86	APCR700	BD	565479
Ly6C	APC-fire 750	Biolegend	128046
Ly6G	V605	Biolegend	127639
CCR2	BV650	Biolegend	150613
L/D	V575	BD	565694
GLUT1	AF647	Abcam	ab195020
CD3	BUV496	BD	612955
CD4	BUV661	BD	612974
CD8	BUV563	BD	748535
CD44	BUV737	BD	612799
CD62L	BUV615	BD	752311
TNF	BB700	BD	566510
Arginase	PE	ThermoFisher	12-3697-82
CPT1a	FITC	Abcam	ab171449
CD31	AF594	Biolegend	303126
CD11b	FITC	Biolegend	101206
F4/80	PeCy7	Biolegend	123114
CD3	BV786	BD	564010
Ly6G	BV421	Biolegend	127628

Ly6C	AF700	Biolegend	128024

Table 3. Details of IHC antibodies used.

Antibody	Vendor	# Catalog	Titration/Dilution
CD31	AbCam	ab182981	1:1000
CD3	ThermoFisher Scientific	RM-9107-S1	1:200
CD8	ThermoFisher Scientific	14-0195-82	1:125
CD11b	AbCam	ab133357	1:8000
F4/80	Biorad	MCA497	1:2000

Table 4. Details of Western blot antibodies

Antibody	Vendor	# Cat	Dilution
ASCT2	Cell Signaling	ADD	1:1000
KAG	Proteintech	20170-1-AP	1:500
GAC	Proteintech	19958-1-AP	1:500
GLS2	Abcam	ab113509	1:1000
GLUL	Cell Signaling	80636	1:1000
HIF1a	Cell Signaling	14179S	1:500
β-actin	Cell Signaling	4967L	1:1000

Chapter 2: SIRPα-CD47 axis as a novel immunotherapeutic target of immunosuppressive macrophages in prostate cancer

Abstract

Treatment options for localized prostate cancer include radical proctectomy or androgen deprivation (AD) therapy followed by radiation therapy. Although AD therapy has a high rate of progression-free survival, nearly 30–50% of patients progress to developing mCRPC, which has a 30% 5-year survival rate.

Therapeutic options for mCRPC include chemotherapy- and ADT given in combination with androgen receptor axis-targeted therapy such as enzalutamide or abiraterone acetate. These therapies might yield progression-free survival of 18-20 months. Unfortunately, mCRPC is virtually resistant to either Sipuleucel-T vaccine (the only FDA-approved vaccine) or the existing T cell checkpoint blockade therapies. Additionally, the primary and metastatic (TME is highly immunosuppressive, characterized by fewer cytotoxic T cells and higher abundance M2-TAMs that occlude infiltration of other cytotoxic immune cells to mount an effective anti-tumor response. Utilizing a successful myeloid checkpoint blockade therapy to reprogram M2-TAMs in primary and mCRPC can be a promising alternative to a T cell ICB approach.

While targeted depletion of M2-TAMs via pharmacological or antibody-mediated targeting of the SCF-1/CSF-1R axis has shown promising anti-tumor responses, non-specific depletion of TAMs severely compromises host defense, homeostasis, and erythropoiesis. Remodeling TAMs in the TME remains an attractive approach to circumvent issues associated with TAM-depletion strategies.

Cancer cells overexpress CD47 (‘don’t eat me’ signal) that masks calreticulin-mediated phagocytosis-mediated elimination. Therapeutic targeting of the myeloid phagocytosis checkpoint CD47-SIRPα axis has shown tremendous preclinical and clinical anti-tumor responses against

diverse tumors. The ultimate goal of immunotherapeutic blockade of CD47-SIRPα interaction is to restore the lost phagocytic potential of TAMs that leads to enhanced antigenic presentation and T cell priming for effective anti-tumor T cell responses.

Here we show increased CD47 expression in prostate adenocarcinoma as compared to normal prostate tissue. The increased expression of key genes in the CD47-SIRPα axis was validated using diverse PCa cell lines and macrophages cultured in vitro. Further, we show that antibody-mediated blockade of CD47-SIRPα axis increases phagocytosis of metastatic prostate cancer cells by M2-polarized human macrophages. Finally, using different syngeneic murine models of prostate and bladder cancer, we provide evidence of tumor growth inhibition in a CD47 deficient background via antibody-mediated targeting of CD47-SIRPα axis. We also provide evidence of increased reprogramming of TAMs, leading to a phenotypic shift from M2-like TAMs to M1-like TAMs concomitant with increased antigen presentation, which possibly drives increased CD8 T cell proliferation in tumors lacking CD47.

Introduction

Cancer immunotherapy utilizes the patient's own immune system to combat cancer, which is primarily achieved by immune checkpoint-targeted therapy and the adoptive transfer of manipulated immune cells. The main focus of previously developed immunotherapies is to stimulate adaptive immune cells by revitalizing or boosting T-cell responses to override the immune inhibitory pathways to unleash T-cell responses [161]. The remarkable clinical success of checkpoint-targeted therapies against a range of cancers is a distinct advantage over traditional anti-tumor therapies. However, low response rates, high costs, and non-specific toxicity are some of the key challenges of checkpoint-targeted therapies that remain to be addressed [162].

Professional antigen-presenting cells (APCs) such as monocytes, macrophages, and dendritic cells (DCs) act as a bridge between innate and adaptive immunity due to their ability to process and cross-present peptide antigens to naïve T cells, which leads to their activation [17]. Professional APCs detect, phagocytose, and perform lysosomal degradation of tumor cells through a highly regulated process involving receptor-ligand interaction and act like the first line of defense against malignant cell transformation [17]. While non-malignant and healthy cells avoid self-elimination by professional phagocytes by expressing anti-phagocytosis receptors ('don't eat me' signals), malignant cells significantly rely on such receptors and overexpress them to elude immune-mediated destruction [163].

Tumour cell phagocytosis by macrophages and DCs is modulated by different pro-phagocytosis ('eat me') and anti-phagocytosis ('don't eat me') signals through receptor-ligand interaction at the cell surface. 'Eat me' signals or molecules are expressed on or secreted from cells to induce phagocytosis and include neoantigens, calreticulin (CRT, an endoplasmic reticulum chaperon protein), cell surface-bound thrombospondin (TSP-1) complement factors, oxidized low-density lipoproteins, lipid phosphatidylserine, the intracellular adhesion molecule ICAM-3 and glycoprotein signalling lymphocytic activation molecule family member 7 (SLAMF7) [164]. Cancer

cells express ‘don’t eat me’ signals to evade phagocytosis, which include cluster of differentiation 47 or CD47 (also known as integrin-associated protein, IAP), programmed cell death 1 ligand (PD-L1), β2-microglobulin (B2M) subunit of MHC I, stanniocalcin 1 (STC-1), GD2, CD24, and other unidentified ligands that bind to leukocyte immunoglobulin-like receptor 2 (LILRB2) [165].

Phagocytosis Checkpoints

CD47-signal-regulatory protein α (SIRPα)

The CD47-signal-regulatory protein α (SIRPα) axis, identified in the late 2000s, is the first myeloid-cell-specific tumor phagocytosis checkpoint [166]. Earlier considered as the ‘marker of self’ on murine red blood cells (RBCs) that binds to SIRPα on phagocytes, it was recently identified as a ‘don’t eat me’ signal on cancer cells [167]. Importantly, blocking CD47 alone is insufficient to induce tumor cell phagocytosis, as additional pro-phagocytic signals, such as calreticulin, are needed for the cells to be phagocytosed. The majority of normal cells, except aging RBCs, lack these pro-phagocytic signals and remain unaffected by CD47 blockade. However, since malignant cells overexpress pro-phagocytic signals, the CD47 blockade renders them susceptible to phagocytosis by professional APCs. Increased expression of CD47 remains a common feature in different solid tumors, including the ovary, breast, colon, prostate, bladder, brain, liver, and other hematological malignancies [168].

Historically, the role of CD47 in phagocytosis and immune recognition was identified when RBCs deficient in CD47 were reported to be cleared from the bloodstream via splenic red pulp macrophages, while normal RBCs via their functional CD47-SIRPα remained unaffected [163]. Later, it was established that the role of CD47 in inhibiting immune recognition and attack on self-tissues is conserved across species [119].

Therapeutic blockade of CD47 using monoclonal antibodies leads to increased phagocytosis of tumor cells via APCs and inhibition of tumour engraftment and growth in mice lacking T cells, B

cells, and NK cells, while depletion of macrophages restores tumour growth upon CD47 blockade [168]. These observations suggest the crucial role of phagocytes in immunosurveillance against cancer cells and the role of CD47 on cancer cells in immune escape via macrophage-mediated phagocytosis.

In addition to binding with SIRPα, CD47 also interacts with thrombospondin 1 (TSP-1) and another member of the SIRP family, SIRPγ [169]. While SIRPα is mainly expressed on macrophages, SIRPγ is mainly expressed on macrophages and lymphocytes, respectively [165]. SIRPα is a transmembrane glycoprotein that has a ligand-binding extracellular immunoglobulin domain and a cytosolic domain that includes an immunoreceptor tyrosine-based inhibitory motif (ITIM), which associates with either SH2-containing protein tyrosine phosphatase 1 (SHP1) or SHP2 [166]. CD47 has a long N-terminal extracellular domain and five transmembrane domains, as well as a short cytosolic domain, that differs between CD47 isoforms. The extracellular IgV-like domain of CD47 binds with the N-terminal IgV-domain of SIRPα that, leads to the phosphorylation of two tyrosine residues in the intracellular ITIM domains of SIRPα [170]. The phosphorylated tyrosine residues then recruit and activate SHP1 and SHP2, leading to a cascade that ultimately leads to dephosphorylation of myosin IIA and, hence inhibition of cytoskeleton rearrangement, leading to phagocytosis inhibition [171]. CD47 binding to TSP-1 inactivates vascular endothelial growth factor receptor 2 (VEGFR2), which leads to suppression of angiogenesis; hence TSP-1 is recognized as a potent tumor growth and metastasis inhibitor [172].

CD47 expression is induced by TNF-induced expression of NF-KB and through activation of transcription factors such as Myc, HIF-1, and NRF-1. Signaling via oncogenic activation of Myc and ERK directly affects CD47 expression and CD47-SIRPα signaling as the key mechanism of immune evasion in tumor cells [173].

PD-L1-PD1

PD-L1 is a ligand of programmed cell death protein PD-1 (CD279), an immune checkpoint receptor upregulated on activated T cells. It is considered a T cell exhaustion marker that induces immune tolerance. The engagement of PD-1 with PD-L1 (CD274) expressed on cancer cells and APCs is known to inhibit TCR-mediated activation of IL-2 release and T cell proliferation [174]. Therapeutic blockade of PD-1/PD-L1 interaction has been widely used with proven clinical efficacy in diverse cancers such as melanoma, colorectal cancer, non-small-cell lung cancer, and Hodgkin's lymphoma [175]. In a landmark study, PD-1 expression by tumor-associated macrophage was known to inhibit phagocytosis and anti-tumor immunity. In this study, *Gordon et al.* demonstrated increased PD-1 expression on TAMs in murine models of cancer and with increasing disease stages in primary human cancers [152,248]. The study provides the first evidence of the role of the PD-1/PD-L1 axis on macrophage phagocytosis as increased PD-1 expression on TAMs was negatively correlated with phagocytosis, reduced tumour growth, and increased survival in tumor-bearing mice in a macrophage-dependent manner [176]. Interestingly PD-L1 knockout significantly increased tumour cell phagocytosis by PD-1+ TAMs, providing evidence that cancer cell PD-L1 expression attenuates macrophage-mediated phagocytosis and hence therapeutic blockade of PD-1/PD-L1 axis could serve the dual purpose of increased T cell-mediated anti-tumor immunity and phagocytic destruction of tumour cells [176]. However, the signaling pathways that promote the anti-phagocytosis function of PD-1 in TAMs are not understood.

PD-L1 expression is regulated at genomic, transcriptional, and posttranslational levels. Both type I and type II IFN and proinflammatory cytokines promote PD-L1 expression in different tumors [177]. In addition, oncogenic HIF-1, Myc, NF-kB, PTEN/PI3K-AKT, and MAPK pathways play a crucial role in PD-L1 expression [178].

The MHCI (β2 Macroglobulin/B2M)-LILRB1

The major histocompatibility complex I (MHC I) is expressed on many nucleated cells, where it presents tumor-associated antigens to CD8 T cells to activate the adaptive response [179]. MHC I is a heterodimer composed of an α heavy chain and a β2-microglobulin (B2M) light chain. LILRB1 is a member of the leukocyte immunoglobulin-like receptor (LILR) family of receptors that is widely expressed on APCs, including macrophages, DCs and monocytes, and diverse other immune cells [84]. However, the expression of LILRB1 is significantly higher on immunosuppressive M2-like TAMs and tolerogenic DCs [180]. Binding of the B2M subunit of the MHC I on tumour cells with LILRB1 on TAMs inhibits phagocytic activities of TAMs, leading to reduced immune surveillance and enhanced immune evasion of cancer cells [180]. Disruption of B2M-LILRB1 binding potentiates phagocytosis of tumor cells *in vitro* and *in vivo*. Interestingly co-deletion of MHC I and CD47 caused synergistic tumor growth inhibition in immunocompetent hosts that were dependent on macrophages [180]. Like LIRLB1, LILRB2 (another member of the LILR family) interacts with MHC I molecules expressed on APCs. Therapeutic antibody blockade of LILRB2 is known to increase the phagocytic activities of TAMs and enhance their anti-tumor efficacy when combined with anti-PD-L1 antibodies in transgenic mice expressing human LILRB2 on $CD11b^+$ cells [180]. However, the exact mechanism of LILRB2 antagonism-induced macrophage phagocytosis inhibition remains to be explored [165].

Stanniocalcin 1 (STC-1)-Calreticulin (CRT)

Stanniocalcin 1 (STC-1) is a glycoprotein widely expressed in the ovary, prostate, bladder, kidney, adrenal, lung, and other organs in mammals [181]. Recently STC-1 was identified for its role in inhibiting phagocytosis by APCs, including macrophages and DCs. Tumour cell STC-1 expression correlates with immunotherapy efficacy and is negatively associated with patient survival across diverse cancer types. Both gain- and loss-of-function experiments suggested STC-1 promotes tumor progression and enables tumor resistance to checkpoint blockade in murine tumor models. STC-1 binds with an ‘eat me’ signal, calreticulin (CRT), and reduces its membrane exposure,

which significantly inhibits CRT-mediated tumour cell phagocytosis. Notably, STC1-CRT binding also impairs antigen presentation capabilities of APCs which results in reduced T cell activation [182].

CD24-Siglec 10

CD24 is a GPI-anchor protein located in the cell membrane of both normal and malignant cells. CD24 expression on cancer cells is significantly increased on the tumor cell surface as compared to adjacent tissue and is positively correlated with the occurrence and development of tumors. CD24 binds to different proteins, like Siglec 10, Siglec E, P- and L1-selectin, to perform different functions. Siglec 10, an immunosuppressive inhibitory receptor on TAMs, when it binds to CD24, reduces the phagocytosis of tumour cells [183]. Indeed, genetic ablation of either CD24 or Siglec-10, as well as antibody-mediated blockade of CD24-Siglec-10 interaction, significantly increased phagocytosis of CD24-expressing tumour cells, causing tumor growth reduction and increase in animal survival [184].

Phagocytosis Activating Pathways

Cancer cells overexpress anti-phagocytosis signals ‘don’t eat me’ signals than normal cells to counterbalance ‘eat me’ signals. Chief ‘eat me’ signals include tumor-associated antigens, the endoplasmic reticulum chaperon protein calreticulin, and the signalling lymphocytic activation molecule family member 7 (SLAMF7) (SLAMF7 or CD319) [185].

Calreticulin (CRT)

Calreticulin is an ER-resident chaperon protein that helps in proper protein folding and glycosylation. Apoptotic cells express calreticulin (CRT) on their surface, which forms a bridging complex with complement component C1Q and low-density lipoprotein receptor-related protein 1 (LRP1 or CD91) on phagocytes to initiate phagocytosis [186]. CRT is a damage-associated molecular pattern (DAMP) that is translocated to the surface of dying cancer cells in response to

proapoptotic agents. Recognition of CRT on dying cells facilitates phagocytosis by DCs, triggering immunogenicity [187]. CRT is anchored to the cell surface by binding with membrane glycans, where its interaction with the low-density lipoprotein receptor-related protein 1 (LPR1) receptor expressed on phagocytes [188]. Calreticulin is the dominant prophagocytic signal in different cancer types that is counterbalanced by CD47.

SLAMF7 and MAC1

SLAMF7 or CD319 is one of the seven members of the SLAM family receptors expressed on both tumor cells and immune cells, including macrophages. SLAM family receptors are single-pass transmembrane proteins with two to four extracellular immunoglobulin domains and tyrosine-rich intracellular tails that are involved in the phagocytosis of malignant hematopoietic cells [189]. SLAMF7 is a putative 'eat me' signal that has emerged in cancer. Genetic knockout of *Slamf7* in mice severely compromises the phagocytic abilities (induced by CD47 blockade) of bone marrow-derived macrophages against several B cell-derived and myeloid cell-derived murine cancer cell lines [190]. The interaction of SLAMF7 with macrophage-1 antigen (MAC1) forms a protein complex on the macrophage surface. Through MAC1, SLAMF7 interacts with two ITAM-containing receptors, FcRγ and DAP12, on the macrophage cell surface to initiate signaling via the SRC kinase, spleen tyrosine kinase (SYK), and Brunton's tyrosine kinase (BTK) to induce phagocytosis [190]. Whether SLAMF7 is needed for CD47-mediated phagocytosis is not clear, and further investigation is warranted [167].

Fc receptors

Fc receptors are cell-surface receptors expressed on various immune cells, including macrophages, DCs, B cells, NK cells, and granulocytes, and specifically recognize the Fc region of immunoglobulin (Ig) to regulate phagocytosis and antibody-dependent cell-mediated cytotoxicity (ADCC) [191]. The type I Fc common gamma receptors (FcγRs) are divided into

phagocytosis activating or inhibitory subtypes. FcγRIIB is the only phagocytosis inhibitory receptor, while FcγRI, FcγRIIa, FcγRIIc, and FcγRIIIa, are activating receptor-containing immunoreceptor tyrosine activating motifs (ITAMs) [192].

Role of CD47 in cancer and the tumor microenvironment

Role of CD47/SIRPa in Cancer

The expression of CD47 was first identified as a potential tumour marker for ovarian cancer in the 1990s. Later, differential CD47 overexpression was established between normal and cancer cells of different solid tumours and haematological malignancies.

CD47 expression has an overall effect on the TME, where it plays a role in immune homeostasis, and its expression is closely related to immune infiltration. The sensitivity of malignant cells towards CD47 blockade is well established in both *in vitro* and *in vivo* models. Therapeutic blockade of CD47 or SIRPα causes increased tumor cell phagocytosis by TAMs and improves anti-tumor response in tumor models of glioblastoma, melanoma, lymphoma, breast cancer, and colorectal cancer [167]. It has been shown that anti-CD47 therapy could play a role in causing phenotypic shifts of M2-like TAMs to anti-tumoral M1-like TAMs [193]. It remains an open question whether CD47 blockade plays a role in macrophage recruitment to the tumor site; however, it was noted that phagocytosis following CD47 blockade caused a systemic and local secretion of chemokines and cytokines that potentially caused myeloid cell recruitment into tumors in mice engrafted with small-cell lung cancer (SCLC) tumors [194].

In addition to its effects on macrophages and DCs, the blockade of CD47-SIRPα interaction promotes neutrophil-mediated breast cancer cell clearance by anti-HER2 antibody [195]. Similarly, SIRPα blockade was shown to promote neutrophil-mediated cancer cell phagocytosis of several human cancer cells and increased intra-tumoral infiltration of neutrophils [196].

Evidence also points out that the CD47-SIRPα axis is involved in the regulation of neutrophil-mediated trogoptosis of cancer cells [197].

As mentioned earlier, CD47 binds to TSP-1, and integrin and inhibition of CD47 can negatively regulate their function. TSP-1 restricts anti-tumor immunity via CD47-dependent regulation of innate and adaptive immunity via regulation of angiogenesis and perfusion of the tumor vasculature. In addition, TSP-1 plays a role in cell proliferation, invasion, and metastasis and is associated with a worse survival rate, either via its interaction with CD47 or independently [198]. Antibody-mediated blockade of CD47 leads to inhibition of TSP-1-mediated cell proliferation in vivo [199], an indication of the indirect anti-tumor effect of CD47 blockade.

While increased CD47 expression on NK cells is known to increase its recruitment in the TME, ligation of CD47 on NK cells via TSP-1 inhibits NK cell proliferation and its effector phenotypes, indicating an inhibitory function of CD47 on NK cells. This inhibitory effect of CD47 on NK cells via TSP-1 is abrogated via antibody-mediated blockade CD47 that blocks TSP-1 binding, delays tumour growth that is associated with increased NK cell recruitment, and increased granzyme B and IFNγ levels on intra-tumoral NK cells but not CD8+ T cells [200]. Augmented NK cell anti-tumor responses have been observed elsewhere following the disruption of CD47-SIRPα axis [201].

The CD47-SIRPα axis plays an important role in antigen processing and presentation, especially during immunogenic cell death and during chemotherapy with cytotoxic agents that induce apoptosis. Cytotoxic therapy, when given prior, shows synergy with CD47-directed therapies [202]. Tumor antigens and nucleic acid fragments released from dying cancer cells following chemotherapy into the tumor microenvironment potentiate anti-CD47 activity [202]. Indeed azacytidine (DNA hypomethylating agent) and venetoclax (B-cell lymphoma-2 inhibitor) are known to induce the expression of other pro-phagocytic calreticulin [203].

The increased T cell priming and anti-tumor effects of CD47 blockade are in part dependent on cGAS-STING signaling, especially in DCs [165]. The CD47-SIRPα signaling is an important link between innate and adaptive immune responses. Increased uptake of DAMPs (nuclear DNA, mitochondrial DNA, etc.) by cytosolic sensor cGAS (DNA sensor cyclic GMP-AMP synthase) following immunogenic tumor cell death causes activation of inflammatory responses, including type I IFN secretion via cGAS/STING/IRF3 signaling in professional APCs [204]. Increased type I IFN directly induces the maturation of DCs, increases the expression of costimulatory molecules, and cross-presentation of tumor antigens to T cells that prime T cell responses [165]. Anti-CD47 treatment has shown increased anti-tumor cytotoxic T cells and reduced regulatory T cell populations in several preclinical models of chronic lymphocytic leukemia, colon cancer, melanoma, and glioblastoma [205].

The CD47-SIRPα targeted therapy also helps overcome immune checkpoint blockade immunotherapy resistance mediated by T cell exclusion. A potent synergy between selective SIRPα blockade and immune checkpoint blockade has been observed that led to increased memory T cell responses and reversal of T cell exclusion in both syngeneic and orthotopic tumor models. The selective SIRPα blockade also caused tumor nest T cell recruitment by restoring murine and human macrophage chemokine secretion and increased anti-tumor T cell responses by promoting tumor antigen cross-presentation by DCs. However, nonselective blockade of CD47 caused impairment of human T cell activation, proliferation, and endothelial transmigration [206]. Since CD47 directly links innate and adaptive immune responses, it also provides a strong rationale for combining CD47 targeting agents with checkpoint inhibitors in clinical trials.

Therapeutic targeting of SIRPα-CD47

The CD47-SIRPα axis is the most studied myeloid phagocytosis checkpoint in malignancies. The therapeutic strategies aimed at blocking the interaction between CD47 and SIRPα can be broadly

classified as CD47 targeting agents, SIRPα targeting agents, and bispecific agents. These agents include anti-CD47 or anti-SIRPα antibodies and recombinant proteins containing the extracellular regions of CD47 or SIRPα, which at threshold titration, compete with the endogenous proteins for binding. Also, agents that target pathways regulating the CD47 transcription or its trafficking have been developed with the aim to hinder the cell-surface expression of CD47 in cancer cells [165]. Although most of the above-mentioned agents are under early-phase clinical trials, and safety trials, the publicly available data is encouraging due to the promising activity and favorable tolerability [165].

The first category of agents that target CD47 include antibodies or recombinant proteins. The CD47-targeting monoclonal antibodies and fusion proteins with SIRPα immunoglobulin structure bind with CD47 competitively to block the interaction between CD47 and SIRPα. Magrolimab or Hu5F9-G4 (5F9) is a humanized antibody with an IgG4 Fc fragment and has shown anti-tumor efficacy in preclinical models of AML and diverse solid tumor models [207]. A combination of magrolimab with rituximab showed an increased cure rate and disease-free survival in patient-derived NHL xenografted mice. Rituximab, in this combination, played the role of further activator of innate immunity via its active Fc effector function-inducing NK cells and macrophage-mediated cellular cytotoxicity. Magrolimab has undergone clinical trials alone or as a combination therapy with cytotoxic agents and checkpoint blockade antibodies to treat hematological cancers [207]. Other CD47-targeting monoclonal antibodies that have entered clinical development include IBI188 (letaplimab), AK117, and SRF231 [207].

SIRPα-Fc fusion proteins are engineered by combining the CD47-binding domain of SIRPα and the Fc region of human IgG1 or IgG4. These fusion proteins carry different Fc fragments to achieve a balance between therapeutic efficacy and toxicity [208]. The SIRPα-Fc fusion protein TTI-621 was developed using the Fc region of IgG1, while TTI-622 is another variant that is structured using the Fc region of human IgG4 with low Fc receptor interactions and associated

toxicities as compared to TTI-621 [209]. Another SIRPα-Fc fusion protein ALX148 was designed by combining the high-affinity D1 domain of SIRPα with the inactive human IgG1 Fc domain to avoid toxicity [208].

The second category of therapy includes SIRPα targeting agents that are anti-SIRPα antibodies or modified CD47 proteins targeting SIRPα. Unlike CD47, which is expressed in diverse tissues, including RBCs, the expression of SIRPα expression is limited to myeloid cells and neurons which makes SIRPα-targeting antibodies an attractive approach to avoid broader binding and undesirable effects on healthy cells. However, concerns remain regarding neuronal binding and cross-reactivity with other SIRP family members like SIRPβ and SIRPγ that affect the migration of neutrophils and T cells, respectively [207]. Anti-SIRPα antibodies BI 765063 and GS-0189 bear high affinity to SIRPα, have impressive safety profiles, and are in clinical development [207]. ADU-1805 is another anti-SIRPα monoclonal antibody that was developed to block all known SIRPα alleles with improved anti-tumor activity across SIRPα variants [210].

Bispecific agents are novel recombinant antibodies developed to target two different cell surface molecules together. Apart from their role in CD47-SIRPα blockade, bispecific antibodies are under development that is designed to target other cancer cell-specific surface molecules concurrently expressed on tumor cells (i.e., CD19, CD20, PD-L1) or T cells (e.g., PD-1). While the first strategy aims to improve the specificity of tumor targeting and prevent off-target effects, the latter promises synergistic activity with stimulation of both innate and adaptive immune systems [211].

HX009 (PD-1 and CD47 dual blocker), IBI322 (anti-CD47/PD-L1 bispecific monoclonal antibody), and SL-172154 (bifunctional fusion protein consists of human SIRPa and CD40L parts) are some notable bispecific agents undergoing clinical development [207].

Application of CD47-targeting therapies with immune checkpoint blockade

As discussed previously, phagocytosis checkpoint blockade therapies stimulate both innate and adaptive immune responses against tumors that provide a strong rationale for combining them with existing cancer immunotherapies. CD47 expression is linked with the exhaustion of CD8+ T cells via TSP-1, which programs CD8+ T cell exhaustion in cancer through its interaction with CD47 expressed on CD8+ T cells [212]. There is strong evidence suggesting combination therapy with anti-CD47 antibody, and PD-L1 blockade synergizes therapeutic response against melanoma [213]. Another bispecific fusion antibody targeting PD-L1 on tumor cells and SIRPα on phagocytes showed enhanced anti-tumor responses against murine MC38 tumors in syngeneic host compared with either PD-L1 or SIRPa blockade alone [211]. The systemic delivery of the bispecific antibody increased DNA sensing, DC cross-presentation, and anti-tumor T cell responses. While combining CD47 blockade therapy with inhibition of T cell checkpoint provides encouraging results, the effect of PD-1 inhibition might enhance the phagocytic capacities of intra-tumoral macrophages. A more detailed investigation is needed to identify the impact of CD47 blockade on T cell responses, especially in the background that CD47 negatively regulates the differentiation of $CD4^+$ Th1 cells and interacts with TSP1 to inhibit T cell proliferation [176].

Challenges of targeting CD47-SIRPα axis

The ubiquitous expression of CD47 remains one of the major concerns of the application of CD47-SIRPα targeted therapies, which causes rapid drug elimination, and haematological toxicity, which includes anemia and thrombocytopenia. As discussed previously, aging RBCs are significantly sensitive to phagocytosis, and hence their destruction remains a limiting toxicity concern with such drugs and may influence the age of cancer patients [214].

Key questions remaining to be answered

Despite the remarkable progress made in CD47-targeted therapies against cancer, many unanswered questions remain regarding the phagocytosis checkpoint blockade. We still do not know how phagocytosis regulators function in concert to modulate tumor cell clearance by professional APCs during different stages of tumorigenesis. The emerging evidence from the preclinical studies in animal models suggests that complementing T-cell checkpoint inhibition with phagocytosis checkpoint blockade remains an attractive avenue. Further, poor efficacy or toxicity of T-cell checkpoint blockade therapies in different tumors project phagocytosis checkpoint blockade as an alternative or complementing approach to treat unresponsive cancers.

Status of blockade of phagocytosis inhibitors in Prostate carcinoma

Immune checkpoint inhibition strategies targeting CTLA-4, PD-1, or PD-L1 have made major advances in clinical practices to treat urologic tumors, such as renal cell carcinoma and urothelial cancer [215]. However, immune checkpoint blockade therapies have only modest effects on prostate cancers. The immunologically cold and immunosuppressive nature of prostate tumors characterized by a low level of tumor-associated antigens and neoantigens coupled with an increased abundance of M2-TAMs and a lower number of CD8 T cells contribute to therapeutic resistance. Boosting the immune system is considered a good strategy for treating metastatic disease [216]. TAMs represent an interesting target for immunotherapy in prostate tumors. As discussed previously, therapeutic strategies to deplete TAMs or prevent the recruitment of precursor myeloid cells using pharmacological and antibody-mediated targeting of the CSF-1/CSF-1R axis have shown significant anti-tumor responses. However, the phagocytosis checkpoint pathways have never been explored in PCa.

In this study, we provide evidence of increased expression of CD47 and calreticulin in prostate cancer cells. We also provide in vitro and in vivo experimental evidence of therapeutic blockade of the CD47-SIRPα axis increases phagocytosis of prostate tumor cells and causes tumor growth inhibition. Finally, we provide evidence for the role of CD47 in reprogramming the tumor immune microenvironment that suggests increased reprogramming by antigen presentation and TNF+ phenotypic shifts in TAMs and CD8 T cell proliferation.

Results

Increased expression of CD47 and Calreticulin is a characteristic feature of prostate carcinoma.

CD47 expression has been proposed as a prognostic marker in prostate cancer; however, a detailed investigation of the CD47-SIRPα axis in prostate cancer has not been performed [217]. To investigate whether CD47-SIRPα might be a novel immunotherapeutic pathway in prostate cancer, we evaluated the expression levels of CD47 and calreticulin (CRT) in prostate adenocarcinoma. The human protein atlas database (https://www.proteinatlas.org/) contains pathology information based on protein expression (IHC) data from different cancers, including prostate carcinoma. We investigated the differential protein levels of CD47 and CRT in prostate adenocarcinoma tissues with either medium or high gleason scores as defined by protein atlas. We found increased expression of CD47 and CRT in the tumor tissues (tumor/ stromal cells) as compared to baseline controls **(Fig 22A-B)**. We next investigated mRNA expression levels of CD47 and CRT in TCGA, GTEx, and TARGET datasets using Xenabrowser (https://xenabrowser.net/), a database that helps to explore functional genomic data sets for correlations between genomic and/or phenotypic variables. We found elevated expression levels of CD47 and CRT in a total 648 adenocarcinoma patients versus the normal prostate tissue from all three datasets **(Fig 22C-D)**.

Next, we validated the protein expression levels of CD47 in prostate cancer samples using freshly resected tumor tissues following rapid autopsy using pathology with flow cytometry in CD45- fractions in two (n=2) renal cell carcinoma patients (RCC). Flow cytometric evaluation showed a $CD47^{(hi)}$ cell population in the tumor/stromal tissue as compared to non-tumor adjacent (NAT) derived from both patients **(Fig 22E-F)**. Thus, using two different approaches, we confirmed elevated expression levels of the 'don't eat me' signal, CD47, in prostate and RCC tumors. These

results provide a strong rationale for targeting CD47 in urologic tumors to remodel the immunosuppressive TME.

SIRPα and LRP-1 are expressed in immunosuppressive myeloid cells in urologic cancers.

The CD47-binding protein SIRPα is expressed on myeloid cells including macrophages. The binding of CD47 and SIRPα triggers a "don't eat me" signal that protects cancer cells from phagocytosis-mediated clearance [161]. The 'eat me' signal, CRT, is anchored to the cell surface of malignant cells by binding membrane glycans, where it interacts with LRP-1 expressed on macrophages to assist phagocytosis [188]. Next, we investigated the expression levels of SIRPα (the receptor for CD45) and LRP1 (the ligand for CRT) on macrophages in prostate cancer. To this end, we first examined expression levels of SIRPα and LRP-1 using Xenabrowser across 648 samples from TCGA, GTEx, and TARGET datasets. No significant transcript level changes were observed for SIRPα and LRP-1 in prostate adenocarcinoma patient samples when compared with normal prostate tissue samples **(Fig 23A)**. It is, however, important to note that overexpression of CD47 ligand expression on cancer cells can still prevent the engagement of SIRPα for phagocytosis evasion [218]. Hence, differential expression of either SIRPα or LRP-1 doesn't negate the consequences of enrichment of CD47 levels on the target cells.

In addition to macrophages and DCs, SIRPα is expressed on granulocytes and affects their function following engagement with CD47 [196]. Using the scRNAseq dataset from human protein atlas, we identified increased SIRPα+ macrophages as the major cell cluster that expressed SIRPα in non-malignant prostate tissues **(Fig 23B)**. Congruently, we investigated SIRPα expression in the live $CD3^-$ $CD19^-$ $CD56^-$ $CD45^+$ fraction in the RCC patient samples **(Fig 23C)**. However, we did not find significant changes in SIRPα+ CD14+ (Monocytic), SIRPα+ CD11b+ HLA-DR+ (Macrophages) or SIRPα+ CD11b+ HLA-DR-(Granulocytes) cells between NAT (non-adjacent tumor) versus tumor tissue. Interestingly, we observed patient-to-patient variation with

approximately 30-55% of SIRPα+ cells being monocytic in origin. In the patient 1 sample (case I), we found approximately 62-75% of the CD14- cells (granulocytic) were SIRPα+, while in case II, 78-83% of macrophages were SIRPα **(Fig 23D)**. This result indicates that SIRPα+ phagocytes in these tumors might be monocytes, granulocytes, or macrophages.

Since SIRPα+ cells might be of majorly of macrophage origin, we investigated the nature of these macrophages in RCC case I. Flow cytometric evaluation was carried out for surface expression of CD163, CD206, or PD-L1 as the key immunosuppressive markers of immunosuppressive TAMs. In the RCC tumor tissue, the expression (by counts) of CD163, CD206, and PD-L1 was higher as compared to non-adjacent tumor (NAT) **(Fig 23E)**. Overall, we found that SIRPα+ cells seemed to be higher in RCC tumor tissue vs. NAT **(Fig 23D)**. Our observation is in line with the data published in a study by *Yanagita et al*., which showed an increased expression of SIRPα+ in RCC tumor tissues versus NAT [219].

Targeting don't eat me and eat me signals results in increased phagocytosis of PCa cells.

Next, we sought to understand whether blocking the CD47-SIRPα axis would induce phagocytosis in prostate cancer cells. To this end, we first determined CD47 expression in different prostate carcinoma cell lines using flow cytometry. We observed CD47 expression in all the prostate adenocarcinoma lines regardless of their sensitivity- or resistance to androgen, i.e., AR null bone metastatic line-PC3, brain metastatic line-DU145, androgen-independent-CWR22Rv1 and androgen-sensitive line-LnCaP **(Fig 24A)**. We also validated the SIRPα levels in primary PBMC-derived macrophages, human monocytic line, THP-1 cells, and PBMC-derived CD14+ monocytes as phagocyte controls **(Fig 24B)**.

Next, we investigated the mRNA expression levels of SIRPα and LRP-1 on different phagocytic cells and CD47 and calreticulin (CALR) in different prostate cancer cells. Both SIRPα and LRP-1 were most highly expressed in canonically differentiated and M2-like polarized,

immunosuppressive CD206+ CD163+ macrophages **(Fig 24C)**. We also observed increased levels of CD47 and CALR in PC3 cells (AR null bone metastatic line) **(Fig 24D)**.

These results encouraged us to determine the phagocytosis of prostate carcinoma cells by immunosuppressive macrophages in vitro. We next co-cultured either untreated or neuraminidase pre-treated, CTV (cell trace violet)-labeled PC3 cells with M2-polarized and differentiated macrophages. As an intervention to prevent CD47-SIRPα interaction, anti-CD47 (1 μg/ml) or anti-SIRPα (5 μg/ml) antibodies were added in the co-culture assay **(Fig 24D)** as described in the methods. Following co-culture, the percentage of phagocytosed CTV+ PC3 cells were quantified within SIRPα+ macrophages in the live CD45+ fraction after careful exclusion of any CTV signal coming from a cancer cell by itself with flow cytometry **(Fig 24E)**. We found increased phagocytosis of PC3 cells following antibody-mediated blockade of either CD47 or SIRPα. In addition, we also observed a synergistic increase in phagocytosis upon neuraminidase pre-treatment **(Fig 24F)**. The increased phagocytosis of PC3 cells could be explained due to the exposed calreticulin binding site released from the phagocyte that acts as the 'eat me' or opsonization signal [188]. These results clearly indicate that antibody-mediated blockade of CD47-SIRPα interaction renders prostate carcinoma (PC3) cells more susceptible to phagocytosis by TAMs in vitro.

Targeting the CD47-SIRPα axis augments anti-tumor efficacy in urologic tumors.

Since we found increased phagocytosis of prostate cancer (PC3) cells by immunosuppressive TAMs following antibody-mediated blockade of CD47-SIRPα axis, we next sought to determine whether targeting CD47-SIRPα axis results in increased anti-tumor efficacy in vivo. To this end, we used three different urologic tumors in genetically modified animals or blocking antibodies against CD47 and SIRPα. We first inoculated CD45-enriched tumor/stromal B6CaP cells into male CD47-KO and congenic WT animals **(Fig 25A)**. Similarly, we implanted MB49 cells (urothelial carcinoma cells) into female CD47-KO and congenic WT animals **(Fig 25B)**. In both

tumor models, we observed a significant tumor growth inhibition (TGI) during tumor progression in a CD47 deficient background **(Fig 25C and D)**, a phenotype that could be due to the immediate elimination of CD47+ tumor cells early during tumorigenesis. To gain a better understanding of the outcome of therapeutic intervention to block CD47-SIRPα engagement on tumor growth, we used anti-CD47 or anti-SIRPα blocking antibodies following a dosing scheme reported earlier [220]. To this end, we used B6CaP, MB49, and RM-1 tumor models with a similar targeting strategy **(Fig 25E-F)**. We found increased tumor growth reduction mediated by either anti-SIRPα or anti-CD47 blockade antibodies as compared to the respective isotype controls in all three tumor models **(Fig 25G-I)**. We also observed increased animal survival following antibody-mediated blockade of both CD47 and SIRPα of B6CaP and MB49 tumor-bearing mice **(Fig 25G-I)**. These results provide a strong evidence of anti-tumor activity of therapeutic interference of CD47-SIRPα axis in urologic tumors.

Myeloid cell reprogramming upon CD47KO in B6CaP tumor-bearing mice.

The antibody-mediated TGI following CD47 blockade is due to increased antigen presentation either by DCs or macrophages and subsequent priming of cytotoxic T cells that cause increased infiltration and renders them to become proliferative and activated [221]. To gain an insight into myeloid immune cell status and the mechanism of anti-tumor response, we performed the comparative immune-infiltrate analysis in the CD47-KO versus WT prostate tumor. To this end, we investigated TAMs and monocytes within the myeloid compartment **(Fig 26A)**. Overall, there was an increase in the percentage CD11b, inflammatory monocytes, and DCs in CD47-KO tumors **(Fig 26B-C)**. Since macrophages have been reported to be the major SIRPα-expressing cells in normal prostate tissue **(Fig 23A)**, we closely investigated the reprogramming of TAMs and monocytes for the changes in putative antigen presentation capacities. Canonical M2 surface marker expressing TAMs (CD206+ CD163+) showed a marked increase in antigen presentation related co-stimulatory molecules CD86+ and MHCII in CD47-KO tumors as compared to WT.

Additionally, these antigen-presenting cells showed increased TNF levels as determined by intracellular staining, validating the functional reprogramming of TAMs to a more inflammatory state.

Next, we evaluated the implications of the functional reprogramming of TAMs on tumor-infiltrating T cells. To this end, we investigated naïve vs. effector, proliferation, and exhaustion marker on T cells **(Fig 27A)**. While we didn't observe any significant changes in the overall influx of CD4 or CD8 T cells **(Fig 27B-C)**, we found a higher percentage of Ki-67+ CD8 T cells **(Fig 27B-C)**.

Here, we provide an indirect evidence of macrophage reprogramming (a possible increase in antigen presentation) following CD47 deletion, as well as a consequent increase in the proliferation of CD8 T cells.

Discussion

Metastatic castration-resistant metastatic cancer (mCRPC) remains a terminal diagnosis with an aggressive disease progression despite currently approved therapies [1]. The current treatment options for mCRPC includes chemotherapy- and androgen-receptor axis-targeted therapies that might yield progression-free survival of 18-20 months [1]. Unfortunately, mCRPC is virtually resistant to either the Sipuleucel-T vaccine (the only FDA-approved vaccine) or to the existing T cell checkpoint blockade therapies [1]. The failure of immune checkpoint blockade therapies is due to the putative 'cold' nature of prostate cancer, which is characterized by restricted CD8 T cell infiltration, low tumor mutational burden, low PD-L1 expression, and increased infiltration of M2-TAMs that creates a highly immunosuppressive state. Also, androgen therapy is known to cause increased infiltration of M2-TAMs in tumors, associated with worse prognosis [222].

Phagocytosis checkpoint inhibition represents a novel and clinically proven strategy to activate macrophages that is analogous to how classic immune checkpoint inhibitors augment T-cell mediated adaptive immunity by targeting CTLA-4 and PD-1. The CD47-SIRPα axis remains one of the most promising myeloid-cell-based immunotherapeutic targets, leading to several clinical trials that are aimed to evaluate CD47-SIRPα blocking therapies [223]. However, there is a paucity of preclinical or clinical data showing therapeutic interference of CD47-SIRPα interaction in prostate cancer. In a study that aimed to establish the relationship between CD47 and prostate carcinoma and macrophage polarization, an examination of 263 patients with prostate adenocarcinoma was performed for tissue-level expression of CD47, CD68, and CD163. This study shows only 52.5% of tissues have increased expression of CD47. Interestingly, 71.9% of tissues showed high expression of CD163 protein, suggesting a putative relationship between increased levels of M2-like macrophages and CD47 expression [224]. However, the status of phagocytosis checkpoints, including CD47-SIRPα axis and their therapeutic targeting, remains unexplored.

Here, we provide evidence of increased CD47-SIRPα signaling in prostate carcinoma in patient samples and in different prostate carcinoma cells. Using in vitro and in vivo models, we also show that targeting CD47-SIRPα causes increased phagocytosis of prostate cancer cells in TAMs, strongly suppresses tumor growth progression, and improves the survival of tumor-bearing animals. In addition, using tumor immune infiltrate analysis, we provide the preliminary evidence of significant reprogramming of the prostate TME in the absence of a functional CD47-SIRPα.

Using the publicly available datasets, Human Protein Atlas (https://www.proteinatlas.org/) and Xena Browser (https://xenabrowser.net/), we showed increased expression of CD47 ('don't eat me' signal) and calreticulin ('eat me' signal) in prostate carcinoma tissues derived from patients. Since therapeutic blocking of CD47 alone does not ensure tumor cell phagocytosis, increased calreticulin expression on malignant cells is essential for their recognition by phagocytes.

Although unrelated to prostate tumors, we also confirmed the increased presence of $CD45^{(hi)}$ cells in tumor and stromal sites in RCC patient samples. Patients will RCC have increased expression of CD47 expression, blockade of which enhances the anti-tumor effects of macrophages through trogocytosis of cancer cells [225]. RCC tumors have increased infiltration of TAMs, which is associated with the worst prognosis.

SIRPα+ TAMs are the major myeloid cells, in addition to DCs and monocytes, that phagocytose tumor cells within TME following ligation of CD47 with SIRPα. Indeed, our investigation of the scRNAseq dataset (Xena Browser) in non-malignant prostate tissues revealed macrophages as the key immune cells that have high expression of SIRPα followed by fibroblasts.

The confirmation of increased expression of SIRPα and CD47 in macrophages (phagocytosis executioner) and prostate carcinoma cells (target cells) further confirms the increased level of CD47-SIRPα axis. Most strikingly, increased expression of SIRPα was observed in M2-polarized human primary macrophages, while androgen-resistant metastatic human prostate cancer line PC3 cells showed increased levels of CD47.

These results encouraged us to perform an *in vitro* coculture assay, which showed increased phagocytosis of PC3 cells by M2-polarized macrophages. However, antibody-mediated abrogation of CD47-SIRPα interaction suppressed the PC3 cell phagocytosis providing direct evidence of increased phagocytosis of CD47-overexpressing prostate carcinoma PC3 cells by M2-polarized macrophages. Since this assay did not represent the true tumor microenvironment that exists in prostate carcinoma, we further investigated the effects of therapeutic blockade of CD47-SIRPα axis on tumor growth in vivo.

We observed a significant suppression of tumor growth of B6CaP (prostate adenocarcinoma) and MB49 (bladder carcinoma) cells in CD47 deficient mice following tumor engraftment as compared to the wild-type tumors even in the absence of therapy, suggesting the importance of endogenous CD47 signaling in tumor control. Next, therapeutic antibody-mediated blockade of either CD47 or SIRPα resulted in significant tumor growth suppression in the prostate (B6CaP and RM1 tumors) and bladder carcinoma (MB49) tumors. Moreover, there was prolonged survival of B6CaP and MB49 tumor-bearing animals in response to anti-CD47 or anti-SIRPα immunotherapy suggesting the therapeutic benefits following blockade of functional CD47-SIRPα axis.

Previously, therapeutic antibody-mediated blockade of the CD47-SIRPα axis was shown to cause a phenotypic shift of M2-like TAMs to anti-tumoral M1-like TAMs inside the tumor microenvironment [193]. Whether interference with CD47-SIRPα axis leads to changes in immune infiltration or immune cell proliferation remains to be fully explored. However, therapeutic blockade of CD47 was shown to cause the systemic and local release of chemokines and cytokines responsible for myeloid cell recruitment in mice engrafted with SCLC tumors [194].

Our investigation of the prostate immune microenvironment containing CD47-KO prostate tumors revealed evidence of myeloid cell reprogramming. We found increased abundance of inflammatory CD11b+ monocytes and DCs in CD47-KO as compared to their wild-type

counterpart. We also found increased evidence of antigen presentation and inflammatory status in CD206+ CD163+ M2-TAMs in CD47-KO prostate tumors as they showed increased surface expression of CD86 and MHC II molecules with increased TNF levels. This indicates a potential phenotypic shift of M2-TAMs towards M1-like TAMs with increased inflammation. Within the lymphocytic compartment, we found increased presence of proliferating CD8 T cells. Although our investigation into tumor microenvironment reveals anti-tumoral benefits (increased macrophage polarization to M1-like TAMs) in the presence and absence of a functional CD47-SIRPα axis; these results need further evaluation in the presence of anti-CD47 or anti-SIRPα blockade in prostate carcinoma.

Overall, we have been able to provide preliminary evidence of the involvement and targetability of CD47-SIRPα axis in prostate carcinoma, which paves the way to carry out follow-up studies to determine the full landscape of targeting CD47-SIRPα axis in non-metastatic and metastatic tumors. Whether therapeutic targeting of the CD47-SIRPα axis plays a dominant role in prostate tumor progression, especially in the background of the cold nature of these tumors, remains to be fully explored. Further, combining CD47-targeted therapies with T-cell-based checkpoint blockade therapies could significantly enhance the effectiveness of established immune checkpoint blockade therapies and remains an exciting avenue in prostate cancer immunotherapy.

Materials and Methods

Ethics. All protocols used in this study involving animals strictly followed US NIH guidelines and were approved by the Johns Hopkins Medical Institutions Animal Care and Use Committee.

Animals

Experimental protocols involving live animals were performed in agreement with the protocols approved by the Institutions Animal Care and Use Committee (IACUC) at The Johns Hopkins University School of Medicine. Both male and female C57BL/6J (000664) and B6.129S7-Cd47tm1Fpl/J (003173), aged 6-8 weeks, were purchased from Jackson Laboratories (ME, USA). Animals were kept under standard housing conditions (68-76 °F, 30-70% relative humidity, 12-12 light-dark cycle) with free access to standard chow and water. The animals were monitored daily for general behavior and appearance by veterinary specialists.

Tumor models and cell lines

MB49, a mouse urothelial carcinoma cell line (SC148) derived from an adult C57BL/6 mouse by exposure of primary bladder epithelial cell explant to 7,12-7,12-dimethylbenz[a]anthracene (DMBA) for 24 h followed by a long-term culture, was purchased from Sigma. B6CaP $CD45^{-ve}$ cells were gifted by Dr. Brian Simons (Johns Hopkins). RM-1 (CRL-3310™) a mouse prostate carcinoma cell line of fibroblast-like morphology, was purchased from ATCC. MB49-RFP (SC065-R, GenTarget Inc., USA) were obtained from GenTarget Inc. RM1-RFP cells made by transduction of luciferase-RFP construct (LVP440-PBS, GenTarget Inc., USA) in RM1 cells. Cells were harvested following trypsinization, and cell viability was confirmed using Trypan blue dye. For syngeneic heterotopic MB49 urothelial tumor development, live MB49 cells (5.0×10^4 cells per 100 ml of 1x PBS per mouse) were implanted on the right flank in C57BL/6J female mice. For the development of syngeneic heterotopic prostate carcinoma tumors, B6CaP $CD45^{-ve}$ cells were thawed, washed with 1x PBS, and implanted subcutaneously (5.0×10^6 cells per 100 ml 1x PBS

per mouse) on the right flank of C57BL/6J male mice for passaging of the cells in mice. Once the tumors reached 1000 mm^3, they were harvested and implanted after CD45 negative enrichment. Tumor growth was monitored every second day to observe the increase in the tumor burden at the time of treatment initiation. Tumors were measured by electronic caliper, and tumor volume was calculated using the following equation: tumor volume = length x width x height x 0.5326. The maximum allowed tumor, the volume of ~2 cm in any dimension, was based on the guidelines of the institutional IACUC for a single implanted tumor that was visible without imaging.

Tumor Digestion, flow cytometry, and sorting

Mouse tumors were surgically resected, mechanically minced, and digested using Miltenyi's mouse tumor dissociation kit (130-096-730) according to the manufacturer's protocol using gentleMACS™ Octo dissociator (130-096-427). After tumor digestion, cells were filtered through a 100 mm cell strainer (TC70-MT-2, Stellar Scientific). For flow cytometry, single-cell suspensions were washed with 1x PBS and then incubated with ACK lysing buffer (118-156-721 Quality Biologicals).

In-vivo treatment with anti-CD47 or anti-SIRPa

Palpable (100-300 mm^3) tumor-bearing mice were randomized into four groups and treated with either anti-CD47 (MIAP410, BP0283, BioXCell), anti-SIRPα (P84, BE0322, BioXCell) or respective isotype control antibodies (MOPC-21, BE0083, BioXCell, and HRPN, BE0088, BioXCell). For CD47 blockade or concomitant isotype control, MIAP410 or MOPC-21 was administered weekly after randomization 300 µg per mouse intraperitoneally [220]. For SIRPa blockade or concurrent isotype control, P84 or BE0088 was administered thrice weekly after randomization at 200 µg per mouse intraperitoneally [206].

Human tissue resection from pathology

RCC patient tissues (Tumor, non-tumor adjacent, and PBMC) were obtained during rapid autopsy and were subjected to single-cell homogenization and consequent flow-cytometry.

Flow cytometry

Single-cell suspensions were stained with antibodies after viability staining and FcR blocking (BD bioscience, 564765). The following antibodies or dyes were purchased for cell surface or intracellular staining. The staining was followed according to the manufacturer's protocol. For intracellular staining, eBioscience™ Foxp3 / Transcription Factor Staining Buffer Set (00-5523-00, ThermoFisher scientific) was used and was performed as per the manufacturer's protocol. Following that, cells were washed and immunophenotyped using BD FACSCelesta, BD FACS symphony, or Cytek Aurora, and data were analyzed using FlowJo (Version 9 or 10). Supplementary table X contains the list of mouse and human antibodies used in this study.

Phagocytosis assay

The in vitro phagocytosis assay was carried out using flow cytometry. Briefly, in vitro cultured macrophages and PC3 (prostate adenocarcinoma cells, CRL-1435™, ATCC) labeled with 2.5 µM CellTrace™ Violet (CTV, C34557, ThermoFisher Scientific) according to the manufacturer's description. PBMC-derived differentiated macrophages were subsequently co-cultured with neuraminidase (Neuraminidase from *Vibrio cholerae,* 11080725001, Sigma*)* pretreated (overnight) PC3 prostate carcinoma cells at a 1:2 ratio (macrophages: PC3 cancer cells) and incubated for 2 h at 37 °C in 6 well plates. CD47 (1ug/ml) (B6H12, 14-0479-82, ThermoFisher Scientific) and SIRPa (5ug/ml) (KWAR23, NG-1, BioXcell) were added during co-culture. Cells were repeatedly washed to remove non-phagocytosed cells, detached, and were then stained with a viability dye, anti-CD45, and anti-SIRPa antibodies for flow cytometry-based evaluation.

qPCR for CD47 and SIRPα

Total RNA was extracted using RNeasy plus mini kit (Qiagen, 74136) and quantified by Nanodrop (ThermoFisher). For cDNA synthesis, High-Capacity cDNA Reverse Transcription Kit (Applied Biosystem, 4368814) was used. Quantitative real-time PCR was performed on QuantStudio 3

(Applied Biosystems) with Taqman Gene Expression MasterMix and Taqman probes (details in table 5). RPL19 was used as the internal control. All samples were triplicated.

Figures

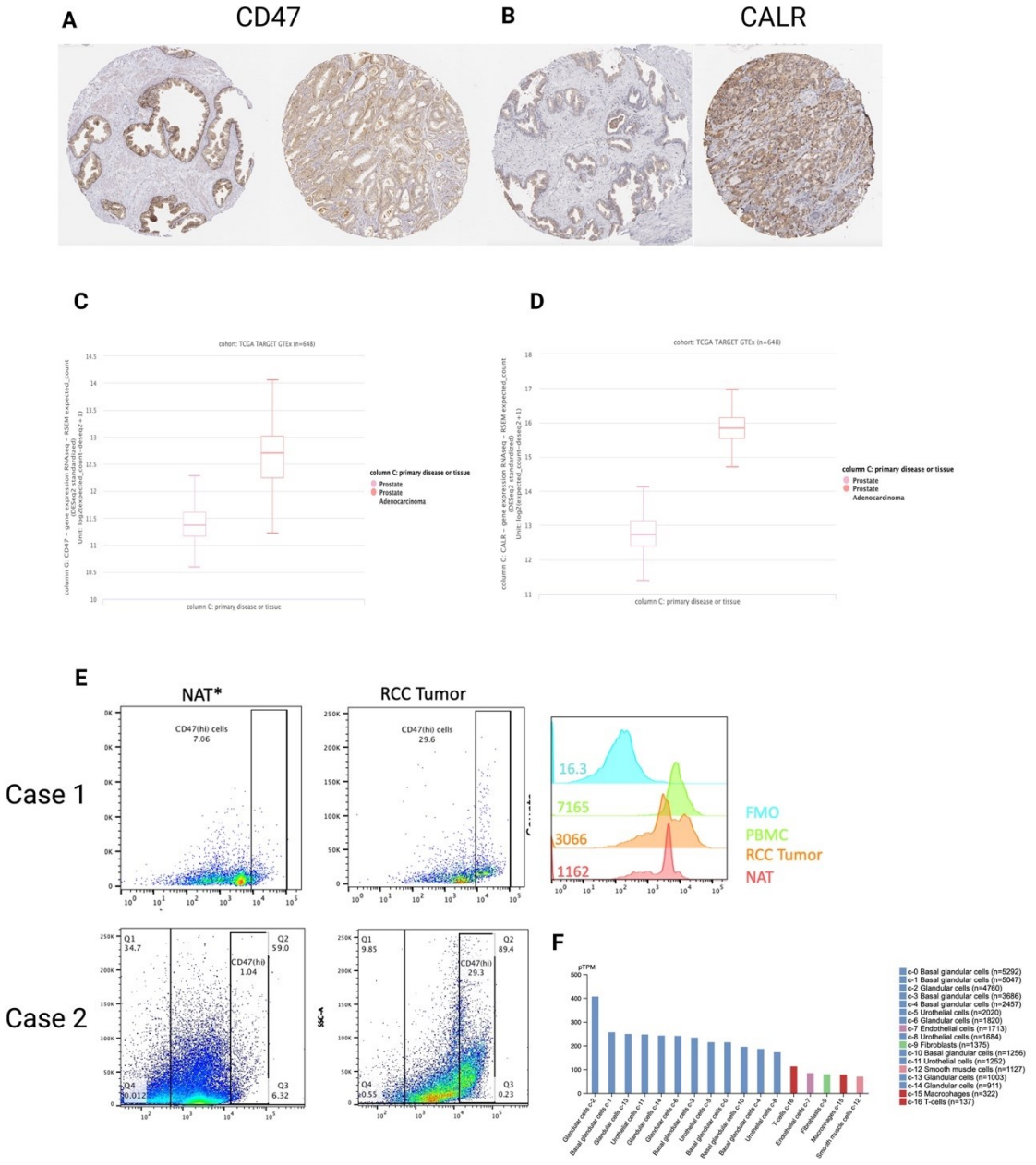

Figure 22. Increased Expression of CD47 and Calreticulin in urologic tumor samples. (A) Differential expression of CD47 in tumor samples vs. normal in prostate cancer patient samples. **(B)** Differential expression of CALR in tumor samples vs. normal in prostate cancer patient samples, **(C and D)** mRNA levels of CD47 and CALR in prostate adenocarcinoma patient-derived tumors vs. normal (n=648). **(E)** Expression levels of CD47 in freshly resected tumor or non-tumor

adjacent tissues in RCC patient samples, and **(F)** CD47 expressing cell types in normal prostate tissue

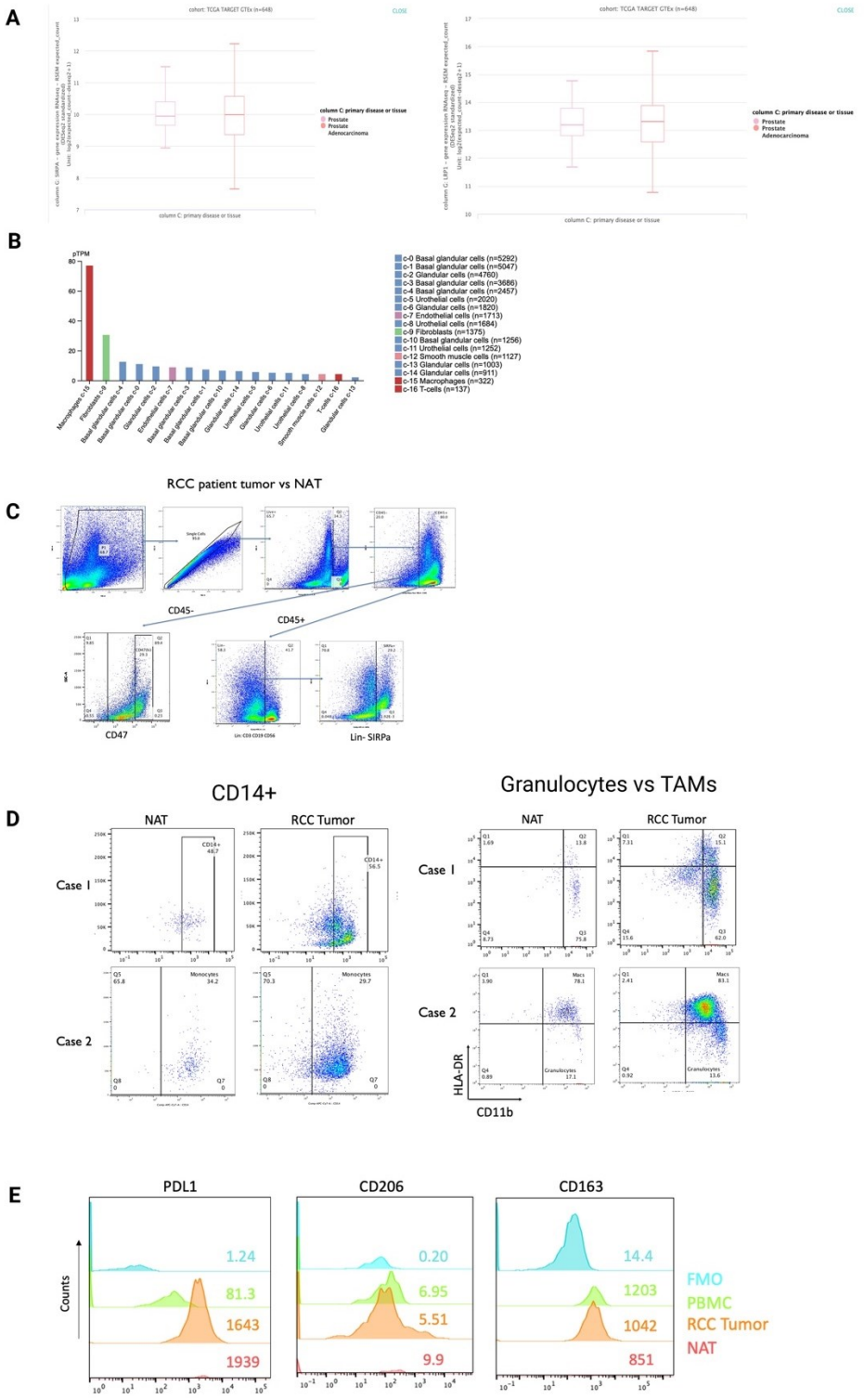

Figure 23. Expression of SIRPα and LRP1 in urologic tumor samples. (A) Differential mRNA

expression of SIRPα and LRP1 in prostate adenocarcinoma patient tumors vs. normal (n=648). **(B)** SIRPα mRNA expressing cells in normal prostate tissue. **(C)** Gating strategy for quantification of CD47 and SIRPα expressing cells. **(D)** SIRPα positive cells in innate cells in RCC patient tumors vs. normal adjacent tissue and **(E)** Immunosuppressive markers in SIRPα+ TAMs.

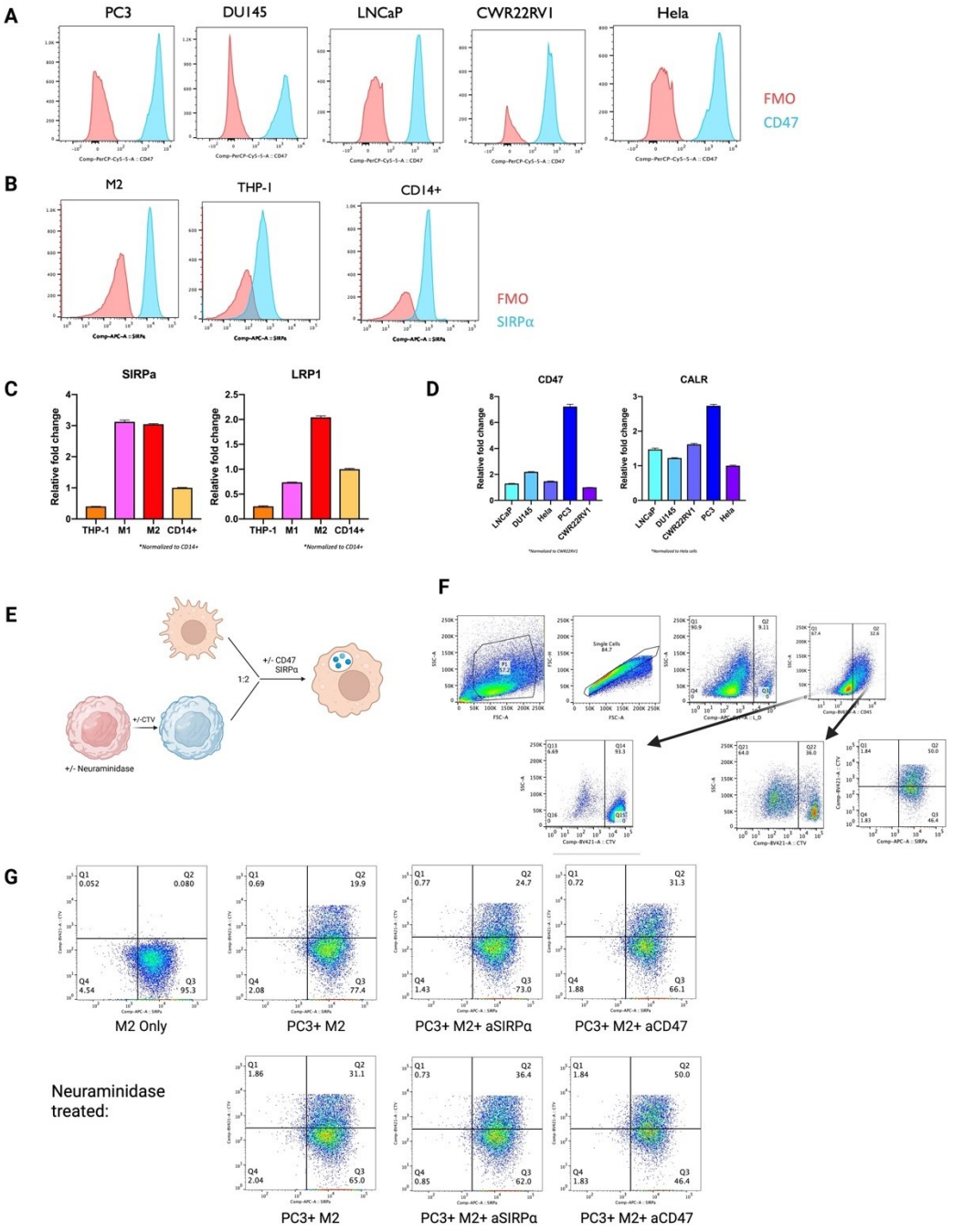

Figure 24. Increased phagocytosis of PCa cells on targeting don't eat me and eat me signaling. **(A)** Expression of ligand CD47 in prostate carcinoma cells lines (bone metastatic line-PC3, brain metastatic line- DU145, androgen-sensitive line-LnCaP, Androgen independent-CWR22Rv1 and Hela. **(B)** Expression of receptor SIRPα in PBMC derived M2 polarized

macrophages, THP-1 cells and CD14+ cells derived from PBMCs. **(C)** Schematic representation of phagocytosis assay, and **(D)** Flow gating for the strategy for phagocytosis assay and (E) % CTV+ SIRPα+ phagocytic macrophages. Data are presented as mean values ± S.E.M. Statistical analyses done with either t-test (*P < 0.05, **P < 0.01, ***P < 0.001, ****P < 0.0001).

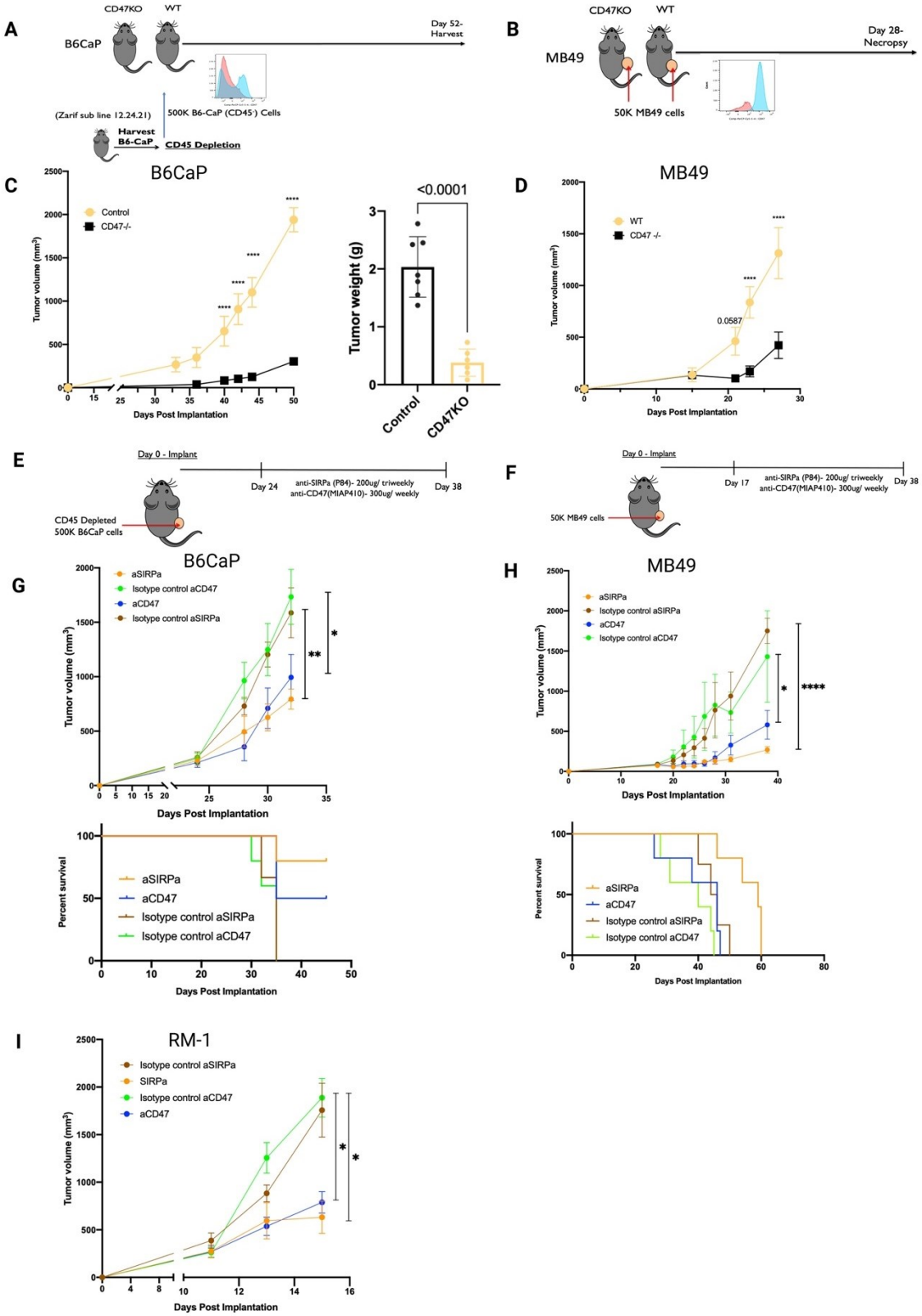
A
CD47KO
WT
B6CaP
Day 52-
Harvest
(Zarif sub line 12.24.21)
500K B6-CaP (CD45-) Cells
Harvest
B6-CaP
CD45 Depletion
B
CD47KO
WT
MB49
Day 28-
Necropsy
50K MB49 cells
C
B6CaP
Control
CD47-/-
Tumor volume (mm³)
Days Post Implantation
<0.0001
Tumor weight (g)
Control
CD47KO
D
MB49
WT
CD47 -/-
0.0587
Tumor volume (mm³)
Days Post Implantation
E
Day 0 - Implant
Day 24
anti-SIRPa (P84)- 200ug/ triweekly
anti-CD47(MIAP410)- 300ug/ weekly
Day 38
CD45 Depleted
500K B6CaP cells
F
Day 0 - Implant
Day 17
anti-SIRPa (P84)- 200ug/ triweekly
anti-CD47(MIAP410)- 300ug/ weekly
Day 38
50K MB49 cells
G
B6CaP
aSIRPa
Isotype control aCD47
aCD47
Isotype control aSIRPa
Tumor volume (mm³)
Days Post Implantation
Percent survival
aSIRPa
aCD47
Isotype control aSIRPa
Isotype control aCD47
Days Post Implantation
H
MB49
aSIRPa
Isotype control aSIRPa
aCD47
Isotype control aCD47
Tumor volume (mm³)
Days Post Implantation
Percent survival
aSIRPa
aCD47
Isotype control aSIRPa
Isotype control aCD47
Days Post Implantation
I
RM-1
Isotype control aSIRPa
SIRPa
Isotype control aCD47
aCD47
Tumor volume (mm³)
Days Post Implantation

Figure 25. CD47-SIRPα targeting in urologic tumors promotes anti-tumor efficacy. (**A and B**) Schematic of GEM CD47KO and WT tumor implantation of B6CaP and MB49 and CD47 expression in CD45- B6CaP cells or MB49 cells before implantation. (**C and D**) Tumor growth kinetics in B6CaP and MB49 respectively (n=5-10/ group). (**E and F**) Schematic of treatment with anti-CD47 and anti-SIRPα antibodies. (**G and H**) Tumor growth kinetics (tumor volumes and survival curves) of B6CaP and MB49 bearing tumors treated with anti-CD47 and anti-SIRPα or respective isotype controls (n= 4-6/ group), and (**I**) Tumor growth kinetics by volume in RM-1 bearing tumors with anti-CD47 and anti-SIRPα antibodies or respective isotype controls. (n =5 or 6/group). Data are presented as mean values ± S.E.M. Statistical analyses done with either t-test or two-way ANOVA using Bonferroni's multiple comparisons (*P < 0.05, **P < 0.01, ***P < 0.001, ****P < 0.0001). Log-rank (Mantel-Cox) tests were performed for survival analysis.

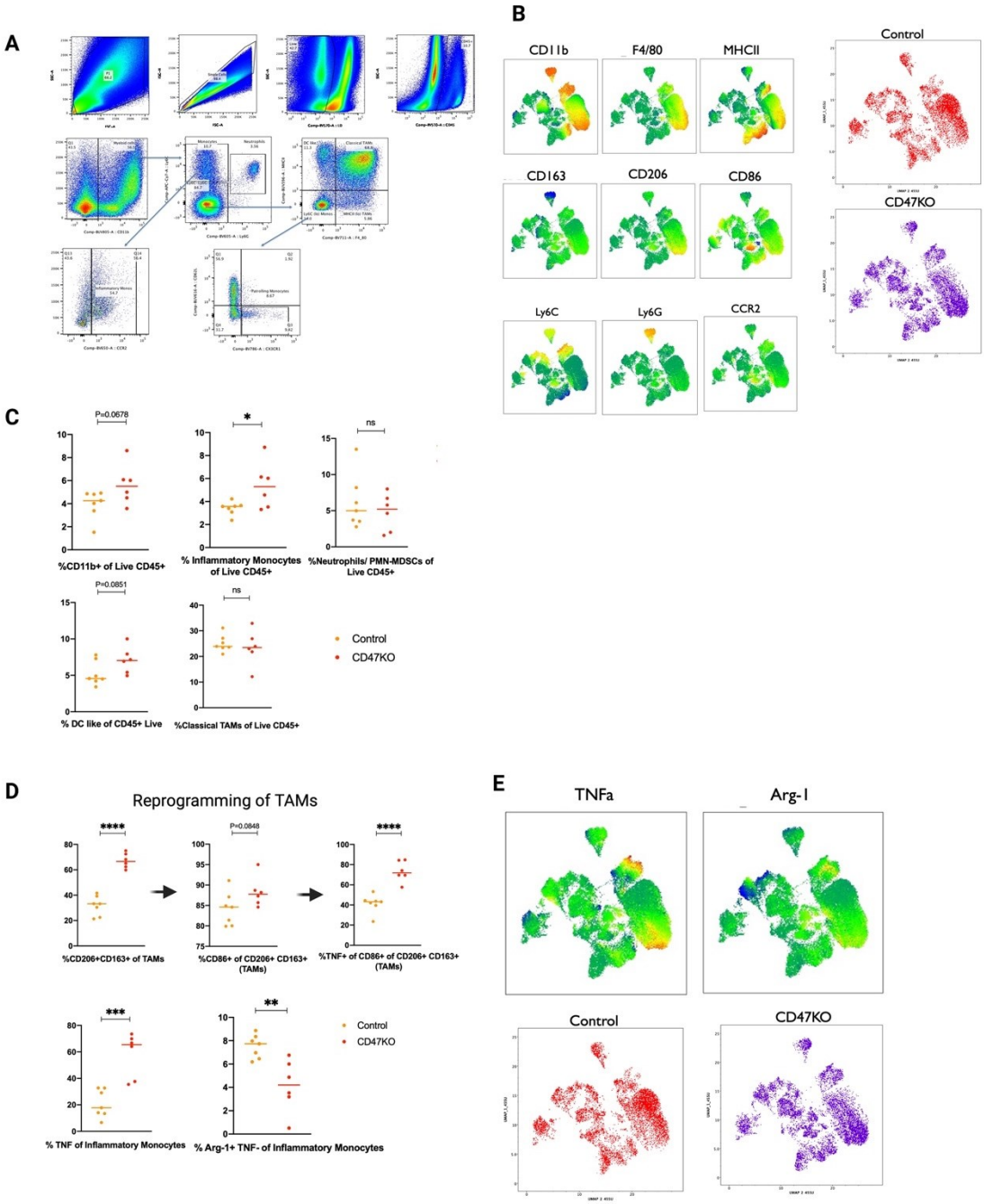

Figure 26. Myeloid cell reprogramming upon CD47KO in B6CaP tumor-bearing mice. (A) Representative flow cytometry gating of myeloid cells in B6CaP TME. **(B)** UMAP of myeloid populations in B6CaP tumors. **(C)** Schematic representation of phagocytosis assay. **(D)** Flow gating for the strategy for phagocytosis assay, and **(E)** % CTV+ SIRPα+ phagocytic macrophages

Data are presented as mean values ± S.E.M. Statistical analyses done with either t-test (*P < 0.05, **P < 0.01, ***P < 0.001, ****P < 0.0001).

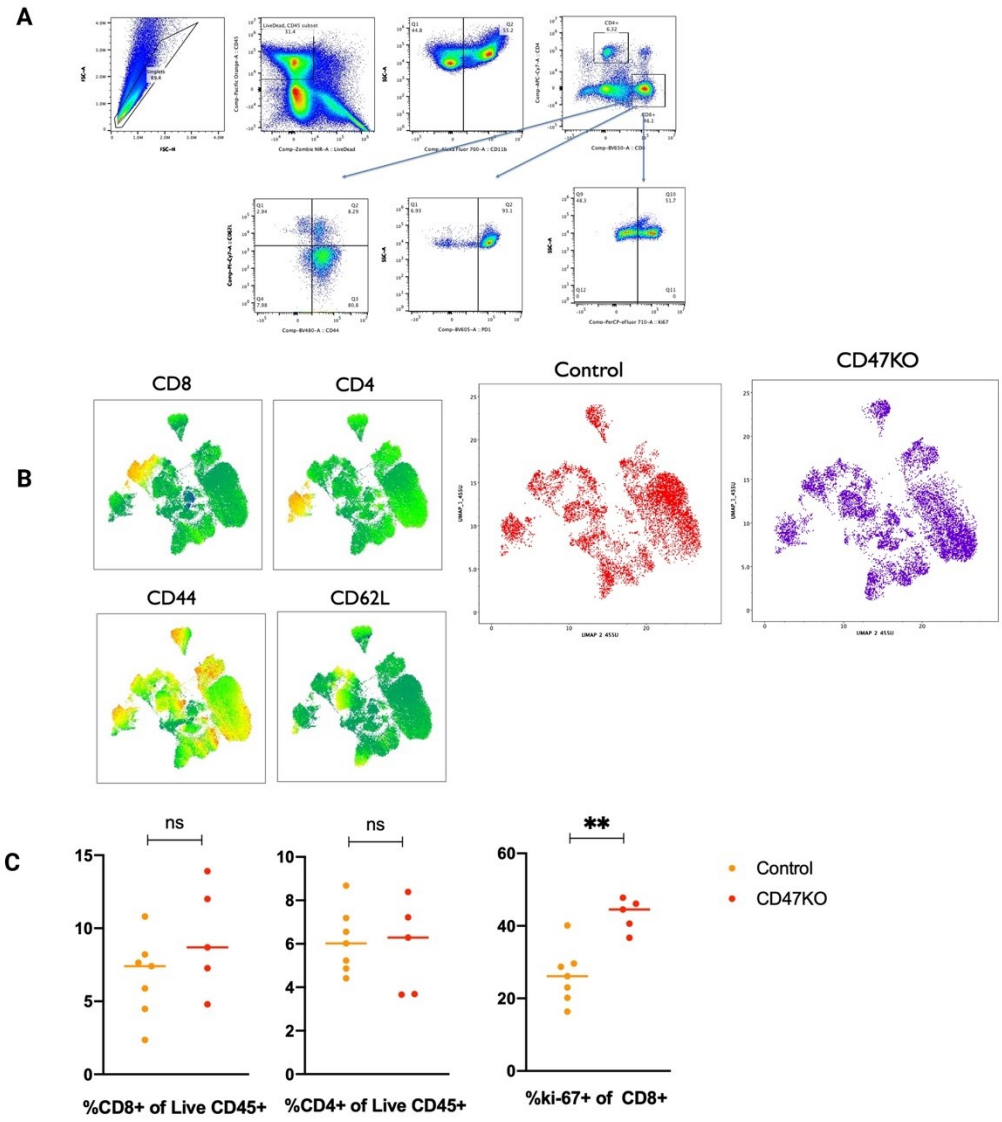

Figure 27. Increased CD8 T cell proliferation in CD47-KO TME. (A) Flow gating strategy of T cells in the B6CaP TME of WT and CD47 KO. **(B)** UMAP of expression levels of different T cell markers and between control relative to CD47KO, and **(C)** Percentage of CD4, CD8 and ki-67+ CD8 T cells in TME. Data are presented as mean values ± S.E.M. Statistical analyses done with either t-test (*P < 0.05, **P < 0.01, ***P < 0.001, ****P < 0.0001).

Table 5. Details of TaqMan probes.

Target	Assay ID	Dye
RPL19	Hs02338565_gH	VIC
CD47	Hs00179953_m1	FAM
SIRPa	Hs00757426_s1	FAM
CALR	Hs00189032_m1	FAM
LRP1	Hs00233856_m1	FAM

Table 6. *In vitro* phagocytosis assay flow cytometry antibody list (anti-human).

Marker	Fluorophore	Vendor	Cat
CD45	BV650	Biolegend	304044
SIRPα	APC	ThermoFisher	17-1729-42
CD47	PerCP/Cyanine5.5	Biolegend	323110
Calreticulin	AF700 (labeled with kit)	Abcam	ab22683
CTV	BV421	ThermoFisher	C34557
L/D	eFluor™ 780	Invitrogen	65-0865-14
CD86	BV786	Biolegend	305442
MHCII	PE-Texas Red	ThermoFisher	MHLDR17

Table 7. List of flow cytometry antibodies.

Marker	Fluorophore	Vendor	Cat #
CD206	PE CF594	BD	141732
CD86	Pe/Cy5	Biolegend	105016
CD62L	PECy7	BD	560516
CD11b	AF700	Biolegend	101222
CD4	APC Cy7	BD	565650
Ly6G	efluor 450	ThermoFisher	48-5931-82
CD44	BV480	BD	566200
TCRb	BV510	BD	563221
CD45	Pacific Orange	Invitrogen	MCD4530
Ly6c	BV570	Biolegend	128030
PD1	BV605	Biolegend	135220
CD8	BV650	Biolegend	100742
MHCII	BV711	Biolegend	107643
CD11c	BV750	Biolegend	117357
F4/80	BV785	Biolegend	123141
CD163	PE	ThermoFisher	12-1631-82
FOXP3	PerCpCy5.5	ThermoFisher	45-5773-82
Ki67	PerCp-eFluor710	ThermoFisher	46-5698-82
CD45	V510	Biolegend	103138
CD11b	UV805	BD	741934
F4/80	V711	BD	565612
MHCII	UV395	BD	743876
CX3CRI	V786	Biolegend	149029
CD206	PE-Cy7	Biolegend	141720

CD163	PE Dazzle	Biolegend	155316
CD86	APCR700	BD	565479
Ly6C	APC-fire 750	Biolegend	128046
Ly6G	V605	Biolegend	127639
CCR2	BV650	Biolegend	150613
L/D	V575	BD	565694
CD3	BUV496	BD	612955
CD4	BUV661	BD	612974
CD8	BUV563	BD	748535
CD44	BUV737	BD	612799
CD62L	BUV615	BD	752311
TNF	BB700	BD	566510
Arginase	PE	ThermoFisher	12-3697-82

References

1. Wang, I., et al., *Prostate cancer immunotherapy: a review of recent advancements with novel treatment methods and efficacy.* Am J Clin Exp Urol, 2022. **10**(4): p. 210-233.
2. Siegel, R.L., et al., *Cancer statistics, 2022.* CA Cancer J Clin, 2022. **72**(1): p. 7-33.
3. Loeb, S. and W.J. Catalona, *The Prostate Health Index: a new test for the detection of prostate cancer.* Ther Adv Urol, 2014. **6**(2): p. 74-7.
4. Sfanos, K.S., et al., *Phenotypic analysis of prostate-infiltrating lymphocytes reveals TH17 and Treg skewing.* Clin Cancer Res, 2008. **14**(11): p. 3254-61.
5. Hu, S., et al., *Infiltrating T cells promote prostate cancer metastasis via modulation of FGF11-->miRNA-541-->androgen receptor (AR)-->MMP9 signaling.* Mol Oncol, 2015. **9**(1): p. 44-57.
6. Ness, N., et al., *Infiltration of CD8+ lymphocytes is an independent prognostic factor of biochemical failure-free survival in prostate cancer.* Prostate, 2014. **74**(14): p. 1452-61.
7. Yuri, P., et al., *Increased tumor-associated macrophages in the prostate cancer microenvironment predicted patients' survival and responses to androgen deprivation therapies in Indonesian patients cohort.* Prostate Int, 2020. **8**(2): p. 62-69.
8. Peiffer, L.B., et al., *Composition of gastrointestinal microbiota in association with treatment response in individuals with metastatic castrate resistant prostate cancer progressing on enzalutamide and initiating treatment with anti-PD-1 (pembrolizumab).* Neoplasia, 2022. **32**: p. 100822.
9. Bonaventura, P., et al., *Cold Tumors: A Therapeutic Challenge for Immunotherapy.* Front Immunol, 2019. **10**: p. 168.
10. Motzer, R.J., et al., *Nivolumab versus Everolimus in Advanced Renal-Cell Carcinoma.* N Engl J Med, 2015. **373**(19): p. 1803-13.
11. Fay, E.K. and J.N. Graff, *Immunotherapy in Prostate Cancer.* Cancers (Basel), 2020. **12**(7).
12. Drake, C.G., et al., *Androgen ablation mitigates tolerance to a prostate/prostate cancer-restricted antigen.* Cancer Cell, 2005. **7**(3): p. 239-49.
13. Song, H., et al., *Single-cell analysis of human primary prostate cancer reveals the heterogeneity of tumor-associated epithelial cell states.* Nat Commun, 2022. **13**(1): p. 141.
14. Calagua, C., et al., *A Subset of Localized Prostate Cancer Displays an Immunogenic Phenotype Associated with Losses of Key Tumor Suppressor Genes.* Clin Cancer Res, 2021. **27**(17): p. 4836-4847.
15. Bilusic, M., R.A. Madan, and J.L. Gulley, *Immunotherapy of Prostate Cancer: Facts and Hopes.* Clin Cancer Res, 2017. **23**(22): p. 6764-6770.
16. Zhang, C., M. Yang, and A.C. Ericsson, *Function of Macrophages in Disease: Current Understanding on Molecular Mechanisms.* Front Immunol, 2021. **12**: p. 620510.
17. Iwasaki, A. and R. Medzhitov, *Regulation of adaptive immunity by the innate immune system.* Science, 2010. **327**(5963): p. 291-5.
18. Mantovani, A., et al., *Macrophage plasticity and polarization in tissue repair and remodelling.* J Pathol, 2013. **229**(2): p. 176-85.
19. Murray, P.J., *Macrophage Polarization.* Annu Rev Physiol, 2017. **79**: p. 541-566.
20. Atri, C., F.Z. Guerfali, and D. Laouini, *Role of Human Macrophage Polarization in Inflammation during Infectious Diseases.* Int J Mol Sci, 2018. **19**(6).
21. Martinez, F.O. and S. Gordon, *The M1 and M2 paradigm of macrophage activation: time for reassessment.* F1000Prime Rep, 2014. **6**: p. 13.
22. Davies, L.C., et al., *Tissue-resident macrophages.* Nat Immunol, 2013. **14**(10): p. 986-95.
23. Mackaness, G.B., *Cellular resistance to infection.* J Exp Med, 1962. **116**(3): p. 381-406.

24. Mantovani, A., et al., *Macrophage polarization: tumor-associated macrophages as a paradigm for polarized M2 mononuclear phagocytes.* Trends Immunol, 2002. **23**(11): p. 549-55.
25. Liu, J., et al., *New insights into M1/M2 macrophages: key modulators in cancer progression.* Cancer Cell Int, 2021. **21**(1): p. 389.
26. Wang, N., H. Liang, and K. Zen, *Molecular mechanisms that influence the macrophage m1-m2 polarization balance.* Front Immunol, 2014. **5**: p. 614.
27. Keen, G.A., *Human cytomegalovirus infection.* S Afr Med J, 1985. **68**(3): p. 159-61.
28. Shapouri-Moghaddam, A., et al., *Macrophage plasticity, polarization, and function in health and disease.* J Cell Physiol, 2018. **233**(9): p. 6425-6440.
29. Kayagaki, N., et al., *Noncanonical inflammasome activation by intracellular LPS independent of TLR4.* Science, 2013. **341**(6151): p. 1246-9.
30. Roh, J.S. and D.H. Sohn, *Damage-Associated Molecular Patterns in Inflammatory Diseases.* Immune Netw, 2018. **18**(4): p. e27.
31. Krausgruber, T., et al., *IRF5 promotes inflammatory macrophage polarization and TH1-TH17 responses.* Nat Immunol, 2011. **12**(3): p. 231-8.
32. Lehtonen, A., et al., *Gene expression profiling during differentiation of human monocytes to macrophages or dendritic cells.* J Leukoc Biol, 2007. **82**(3): p. 710-20.
33. Murray, P.J. and T.A. Wynn, *Protective and pathogenic functions of macrophage subsets.* Nat Rev Immunol, 2011. **11**(11): p. 723-37.
34. Corpas, I. and I. de Andres, *Morphine effects in brainstem-transected cats: I. EEG and 'sleep-wakefulness' in the isolated forebrain.* Behav Brain Res, 1991. **44**(1): p. 11-9.
35. Mantovani, A., et al., *The chemokine system in diverse forms of macrophage activation and polarization.* Trends Immunol, 2004. **25**(12): p. 677-86.
36. Martinez, F.O., L. Helming, and S. Gordon, *Alternative activation of macrophages: an immunologic functional perspective.* Annu Rev Immunol, 2009. **27**: p. 451-83.
37. van Furth, R. and Z.A. Cohn, *The origin and kinetics of mononuclear phagocytes.* J Exp Med, 1968. **128**(3): p. 415-35.
38. van Furth, R., et al., *The mononuclear phagocyte system: a new classification of macrophages, monocytes, and their precursor cells.* Bull World Health Organ, 1972. **46**(6): p. 845-52.
39. Deshmane, S.L., et al., *Monocyte chemoattractant protein-1 (MCP-1): an overview.* J Interferon Cytokine Res, 2009. **29**(6): p. 313-26.
40. Shi, C. and E.G. Pamer, *Monocyte recruitment during infection and inflammation.* Nat Rev Immunol, 2011. **11**(11): p. 762-74.
41. Gordon, S. and A. Pluddemann, *Tissue macrophages: heterogeneity and functions.* BMC Biol, 2017. **15**(1): p. 53.
42. Ginhoux, F., et al., *Fate mapping analysis reveals that adult microglia derive from primitive macrophages.* Science, 2010. **330**(6005): p. 841-5.
43. Akitoshi, Y., et al., *Effect of cyclohexanone derivatives on percutaneous absorption of ketoprofen and indomethacin.* Drug Des Deliv, 1988. **2**(3): p. 239-45.
44. Bleriot, C., S. Chakarov, and F. Ginhoux, *Determinants of Resident Tissue Macrophage Identity and Function.* Immunity, 2020. **52**(6): p. 957-970.
45. Schulz, C., et al., *A lineage of myeloid cells independent of Myb and hematopoietic stem cells.* Science, 2012. **336**(6077): p. 86-90.
46. Gordon, S. and F.O. Martinez, *Alternative activation of macrophages: mechanism and functions.* Immunity, 2010. **32**(5): p. 593-604.
47. Ushach, I. and A. Zlotnik, *Biological role of granulocyte macrophage colony-stimulating factor (GM-CSF) and macrophage colony-stimulating factor (M-CSF) on cells of the myeloid lineage.* J Leukoc Biol, 2016. **100**(3): p. 481-9.

48. Jenkins, S.J., et al., *IL-4 directly signals tissue-resident macrophages to proliferate beyond homeostatic levels controlled by CSF-1.* J Exp Med, 2013. **210**(11): p. 2477-91.
49. Anderson, N.M. and M.C. Simon, *The tumor microenvironment.* Curr Biol, 2020. **30**(16): p. R921-R925.
50. Cendrowicz, E., et al., *The Role of Macrophages in Cancer Development and Therapy.* Cancers (Basel), 2021. **13**(8).
51. Wu, K., et al., *Redefining Tumor-Associated Macrophage Subpopulations and Functions in the Tumor Microenvironment.* Front Immunol, 2020. **11**: p. 1731.
52. Auffray, C., M.H. Sieweke, and F. Geissmann, *Blood monocytes: development, heterogeneity, and relationship with dendritic cells.* Annu Rev Immunol, 2009. **27**: p. 669-92.
53. Pyonteck, S.M., et al., *CSF-1R inhibition alters macrophage polarization and blocks glioma progression.* Nat Med, 2013. **19**(10): p. 1264-72.
54. Hourani, T., et al., *Tumor Associated Macrophages: Origin, Recruitment, Phenotypic Diversity, and Targeting.* Front Oncol, 2021. **11**: p. 788365.
55. Zhu, Y., et al., *Tissue-Resident Macrophages in Pancreatic Ductal Adenocarcinoma Originate from Embryonic Hematopoiesis and Promote Tumor Progression.* Immunity, 2017. **47**(2): p. 323-338 e6.
56. Loyher, P.L., et al., *Macrophages of distinct origins contribute to tumor development in the lung.* J Exp Med, 2018. **215**(10): p. 2536-2553.
57. Ma, R.Y., A. Black, and B.Z. Qian, *Macrophage diversity in cancer revisited in the era of single-cell omics.* Trends Immunol, 2022. **43**(7): p. 546-563.
58. Zhang, L., et al., *Single-Cell Analyses Inform Mechanisms of Myeloid-Targeted Therapies in Colon Cancer.* Cell, 2020. **181**(2): p. 442-459 e29.
59. Gubin, M.M., et al., *High-Dimensional Analysis Delineates Myeloid and Lymphoid Compartment Remodeling during Successful Immune-Checkpoint Cancer Therapy.* Cell, 2018. **175**(4): p. 1014-1030 e19.
60. Mulder, K., et al., *Cross-tissue single-cell landscape of human monocytes and macrophages in health and disease.* Immunity, 2021. **54**(8): p. 1883-1900 e5.
61. Di Conza, G., et al., *Tumor-induced reshuffling of lipid composition on the endoplasmic reticulum membrane sustains macrophage survival and pro-tumorigenic activity.* Nat Immunol, 2021. **22**(11): p. 1403-1415.
62. Cheng, S., et al., *A pan-cancer single-cell transcriptional atlas of tumor infiltrating myeloid cells.* Cell, 2021. **184**(3): p. 792-809 e23.
63. Yin, H., et al., *A Dynamic Transcriptome Map of Different Tissue Microenvironment Cells Identified During Gastric Cancer Development Using Single-Cell RNA Sequencing.* Front Immunol, 2021. **12**: p. 728169.
64. Alleva, D.G. and K.D. Elgert, *Promotion of macrophage-stimulated autoreactive T cell proliferation by interleukin-10: counteraction of macrophage suppressor activity during tumor growth.* Immunobiology, 1995. **192**(3-4): p. 155-71.
65. Munn, D.H. and A.L. Mellor, *Indoleamine 2,3 dioxygenase and metabolic control of immune responses.* Trends Immunol, 2013. **34**(3): p. 137-43.
66. Rodriguez-Garcia, M., et al., *Expression of PD-L1 and PD-L2 on human macrophages is up-regulated by HIV-1 and differentially modulated by IL-10.* J Leukoc Biol, 2011. **89**(4): p. 507-15.
67. Kryczek, I., et al., *Cutting edge: induction of B7-H4 on APCs through IL-10: novel suppressive mode for regulatory T cells.* J Immunol, 2006. **177**(1): p. 40-4.
68. Pello, O.M., et al., *Role of c-MYC in alternative activation of human macrophages and tumor-associated macrophage biology.* Blood, 2012. **119**(2): p. 411-21.
69. Casey, S.C., et al., *MYC regulates the antitumor immune response through CD47 and PD-L1.* Science, 2016. **352**(6282): p. 227-31.

70. Coffelt, S.B., et al., *IL-17-producing gammadelta T cells and neutrophils conspire to promote breast cancer metastasis.* Nature, 2015. **522**(7556): p. 345-348.
71. Mantovani, A., et al., *Macrophages as tools and targets in cancer therapy.* Nat Rev Drug Discov, 2022. **21**(11): p. 799-820.
72. Cassetta, L. and J.W. Pollard, *Targeting macrophages: therapeutic approaches in cancer.* Nat Rev Drug Discov, 2018. **17**(12): p. 887-904.
73. Locati, M., G. Curtale, and A. Mantovani, *Diversity, Mechanisms, and Significance of Macrophage Plasticity.* Annu Rev Pathol, 2020. **15**: p. 123-147.
74. Li, M., et al., *A role for CCL2 in both tumor progression and immunosurveillance.* Oncoimmunology, 2013. **2**(7): p. e25474.
75. Lin, E.Y., et al., *Colony-stimulating factor 1 promotes progression of mammary tumors to malignancy.* J Exp Med, 2001. **193**(6): p. 727-40.
76. Cassier, P.A., et al., *CSF1R inhibition with emactuzumab in locally advanced diffuse-type tenosynovial giant cell tumours of the soft tissue: a dose-escalation and dose-expansion phase 1 study.* Lancet Oncol, 2015. **16**(8): p. 949-56.
77. Tap, W.D., et al., *Structure-Guided Blockade of CSF1R Kinase in Tenosynovial Giant-Cell Tumor.* N Engl J Med, 2015. **373**(5): p. 428-37.
78. von Tresckow, B., et al., *An Open-Label, Multicenter, Phase I/II Study of JNJ-40346527, a CSF-1R Inhibitor, in Patients with Relapsed or Refractory Hodgkin Lymphoma.* Clin Cancer Res, 2015. **21**(8): p. 1843-50.
79. Anfray, C., et al., *Current Strategies to Target Tumor-Associated-Macrophages to Improve Anti-Tumor Immune Responses.* Cells, 2019. **9**(1).
80. Germano, G., et al., *Role of macrophage targeting in the antitumor activity of trabectedin.* Cancer Cell, 2013. **23**(2): p. 249-62.
81. Amarante-Mendes, G.P. and T.S. Griffith, *Therapeutic applications of TRAIL receptor agonists in cancer and beyond.* Pharmacol Ther, 2015. **155**: p. 117-31.
82. Vonderheide, R.H., *CD40 Agonist Antibodies in Cancer Immunotherapy.* Annu Rev Med, 2020. **71**: p. 47-58.
83. Cassetta, L. and J.W. Pollard, *A timeline of tumour-associated macrophage biology.* Nat Rev Cancer, 2023.
84. Zhang, J., et al., *Leukocyte immunoglobulin-like receptors in human diseases: an overview of their distribution, function, and potential application for immunotherapies.* J Leukoc Biol, 2017. **102**(2): p. 351-360.
85. Kaneda, M.M., et al., *PI3Kgamma is a molecular switch that controls immune suppression.* Nature, 2016. **539**(7629): p. 437-442.
86. Ryan J. Sullivan, D.S.H., Anthony W. Tolcher, Amita Patnaik, Geoffrey Shapiro, Bartosz Chmielowski, Antoni Ribas, Les H. Brail, Jennifer Roberts, Lucy Lee, Brenda O'Connell, Jeffrey Lorne Kutok, Suresh Mahabhashyam, Claudio Dansky Ullmann, Michael A. Postow, Jedd D. Wolchok, *Initial results from first-in-human study of IPI-549, a tumor macrophage-targeting agent, combined with nivolumab in advanced solid tumors.* Journal of Clinical Oncology 2018. **Volume 36**(Issue 15_suppl).
87. Mantovani, A., et al., *Tumour-associated macrophages as treatment targets in oncology.* Nat Rev Clin Oncol, 2017. **14**(7): p. 399-416.
88. Mehla, K. and P.K. Singh, *Metabolic Regulation of Macrophage Polarization in Cancer.* Trends Cancer, 2019. **5**(12): p. 822-834.
89. Colegio, O.R., et al., *Functional polarization of tumour-associated macrophages by tumour-derived lactic acid.* Nature, 2014. **513**(7519): p. 559-63.
90. Zhao, Q., et al., *2-Deoxy-d-Glucose Treatment Decreases Anti-inflammatory M2 Macrophage Polarization in Mice with Tumor and Allergic Airway Inflammation.* Front Immunol, 2017. **8**: p. 637.

91. Bonavita, E., et al., *Antagonistic Inflammatory Phenotypes Dictate Tumor Fate and Response to Immune Checkpoint Blockade.* Immunity, 2020. **53**(6): p. 1215-1229 e8.
92. Porta, C., et al., *Tumor-Derived Prostaglandin E2 Promotes p50 NF-kappaB-Dependent Differentiation of Monocytic MDSCs.* Cancer Res, 2020. **80**(13): p. 2874-2888.
93. Prendergast, G.C., et al., *Discovery of IDO1 Inhibitors: From Bench to Bedside.* Cancer Res, 2017. **77**(24): p. 6795-6811.
94. Tang, K., et al., *Indoleamine 2,3-dioxygenase 1 (IDO1) inhibitors in clinical trials for cancer immunotherapy.* J Hematol Oncol, 2021. **14**(1): p. 68.
95. Labadie, B.W., R. Bao, and J.J. Luke, *Reimagining IDO Pathway Inhibition in Cancer Immunotherapy via Downstream Focus on the Tryptophan-Kynurenine-Aryl Hydrocarbon Axis.* Clin Cancer Res, 2019. **25**(5): p. 1462-1471.
96. Long, G.V., et al., *Epacadostat plus pembrolizumab versus placebo plus pembrolizumab in patients with unresectable or metastatic melanoma (ECHO-301/KEYNOTE-252): a phase 3, randomised, double-blind study.* Lancet Oncol, 2019. **20**(8): p. 1083-1097.
97. Wise, D.R. and C.B. Thompson, *Glutamine addiction: a new therapeutic target in cancer.* Trends Biochem Sci, 2010. **35**(8): p. 427-33.
98. Li, T., C. Copeland, and A. Le, *Glutamine Metabolism in Cancer.* Adv Exp Med Biol, 2021. **1311**: p. 17-38.
99. Cluntun, A.A., et al., *Glutamine Metabolism in Cancer: Understanding the Heterogeneity.* Trends Cancer, 2017. **3**(3): p. 169-180.
100. Choi, Y.K. and K.G. Park, *Targeting Glutamine Metabolism for Cancer Treatment.* Biomol Ther (Seoul), 2018. **26**(1): p. 19-28.
101. Palmieri, E.M., et al., *Pharmacologic or Genetic Targeting of Glutamine Synthetase Skews Macrophages toward an M1-like Phenotype and Inhibits Tumor Metastasis.* Cell Rep, 2017. **20**(7): p. 1654-1666.
102. Jha, A.K., et al., *Network integration of parallel metabolic and transcriptional data reveals metabolic modules that regulate macrophage polarization.* Immunity, 2015. **42**(3): p. 419-30.
103. Elgogary, A., et al., *Combination therapy with BPTES nanoparticles and metformin targets the metabolic heterogeneity of pancreatic cancer.* Proc Natl Acad Sci U S A, 2016. **113**(36): p. E5328-36.
104. Robinson, M.M., et al., *Novel mechanism of inhibition of rat kidney-type glutaminase by bis-2-(5-phenylacetamido-1,2,4-thiadiazol-2-yl)ethyl sulfide (BPTES).* Biochem J, 2007. **406**(3): p. 407-14.
105. Gross, M.I., et al., *Antitumor activity of the glutaminase inhibitor CB-839 in triple-negative breast cancer.* Mol Cancer Ther, 2014. **13**(4): p. 890-901.
106. Yue, M., et al., *Oncogenic MYC Activates a Feedforward Regulatory Loop Promoting Essential Amino Acid Metabolism and Tumorigenesis.* Cell Rep, 2017. **21**(13): p. 3819-3832.
107. van Geldermalsen, M., et al., *ASCT2/SLC1A5 controls glutamine uptake and tumour growth in triple-negative basal-like breast cancer.* Oncogene, 2016. **35**(24): p. 3201-8.
108. Hassanein, M., et al., *SLC1A5 mediates glutamine transport required for lung cancer cell growth and survival.* Clin Cancer Res, 2013. **19**(3): p. 560-70.
109. Lukey, M.J., K.F. Wilson, and R.A. Cerione, *Therapeutic strategies impacting cancer cell glutamine metabolism.* Future Med Chem, 2013. **5**(14): p. 1685-700.
110. Ahluwalia, G.S., et al., *Metabolism and action of amino acid analog anti-cancer agents.* Pharmacol Ther, 1990. **46**(2): p. 243-71.
111. Lukey, M.J., W.P. Katt, and R.A. Cerione, *Targeting amino acid metabolism for cancer therapy.* Drug Discov Today, 2017. **22**(5): p. 796-804.
112. Oh, M.H., et al., *Targeting glutamine metabolism enhances tumor-specific immunity by modulating suppressive myeloid cells.* J Clin Invest, 2020. **130**(7): p. 3865-3884.

113. Rais, R., et al., *Discovery of DRP-104, a tumor-targeted metabolic inhibitor prodrug.* Sci Adv, 2022. **8**(46): p. eabq5925.
114. Halama, A. and K. Suhre, *Advancing Cancer Treatment by Targeting Glutamine Metabolism-A Roadmap.* Cancers (Basel), 2022. **14**(3).
115. Schmidt, D.R., et al., *Metabolomics in cancer research and emerging applications in clinical oncology.* CA Cancer J Clin, 2021. **71**(4): p. 333-358.
116. Hanahan, D. and R.A. Weinberg, *Hallmarks of cancer: the next generation.* Cell, 2011. **144**(5): p. 646-74.
117. Pavlova, N.N. and C.B. Thompson, *The Emerging Hallmarks of Cancer Metabolism.* Cell Metab, 2016. **23**(1): p. 27-47.
118. DeBerardinis, R.J. and N.S. Chandel, *Fundamentals of cancer metabolism.* Sci Adv, 2016. **2**(5): p. e1600200.
119. Yang, L., S. Venneti, and D. Nagrath, *Glutaminolysis: A Hallmark of Cancer Metabolism.* Annu Rev Biomed Eng, 2017. **19**: p. 163-194.
120. Vitale, I., et al., *Macrophages and Metabolism in the Tumor Microenvironment.* Cell Metab, 2019. **30**(1): p. 36-50.
121. Biswas, S.K., P. Allavena, and A. Mantovani, *Tumor-associated macrophages: functional diversity, clinical significance, and open questions.* Semin Immunopathol, 2013. **35**(5): p. 585-600.
122. Choi, J., et al., *Glioblastoma cells induce differential glutamatergic gene expressions in human tumor-associated microglia/macrophages and monocyte-derived macrophages.* Cancer Biol Ther, 2015. **16**(8): p. 1205-13.
123. Liu, P.S., et al., *alpha-ketoglutarate orchestrates macrophage activation through metabolic and epigenetic reprogramming.* Nat Immunol, 2017. **18**(9): p. 985-994.
124. Kim, G.W., et al., *Glutamine Synthetase as a Therapeutic Target for Cancer Treatment.* Int J Mol Sci, 2021. **22**(4).
125. Beier, A.K., et al., *Metabolic changes during prostate cancer development and progression.* J Cancer Res Clin Oncol, 2022.
126. Pan, T., et al., *Elevated expression of glutaminase confers glucose utilization via glutaminolysis in prostate cancer.* Biochem Biophys Res Commun, 2015. **456**(1): p. 452-8.
127. Lemberg, K.M., et al., *We're Not "DON" Yet: Optimal Dosing and Prodrug Delivery of 6-Diazo-5-oxo-L-norleucine.* Mol Cancer Ther, 2018. **17**(9): p. 1824-1832.
128. Carducci, M.A., et al., *Phenylbutyrate induces apoptosis in human prostate cancer and is more potent than phenylacetate.* Clin Cancer Res, 1996. **2**(2): p. 379-87.
129. Shen, Y.A., et al., *Inhibition of glutaminolysis in combination with other therapies to improve cancer treatment.* Curr Opin Chem Biol, 2021. **62**: p. 64-81.
130. Yamashita, A.S., et al., *The glutamine antagonist prodrug JHU-083 slows malignant glioma growth and disrupts mTOR signaling.* Neurooncol Adv, 2021. **3**(1): p. vdaa149.
131. Simons, B.W., et al., *A mouse model of prostate cancer bone metastasis in a syngeneic immunocompetent host.* Oncotarget, 2019. **10**(64): p. 6845-6854.
132. Bergen, V., et al., *Generalizing RNA velocity to transient cell states through dynamical modeling.* Nat Biotechnol, 2020. **38**(12): p. 1408-1414.
133. Radtke, D., et al., *Th2 single-cell heterogeneity and clonal distribution at distant sites in helminth-infected mice.* Elife, 2022. **11**.
134. Hoeffel, G., et al., *Adult Langerhans cells derive predominantly from embryonic fetal liver monocytes with a minor contribution of yolk sac-derived macrophages.* J Exp Med, 2012. **209**(6): p. 1167-81.
135. Zarif, J.C., et al., *A phased strategy to differentiate human CD14+monocytes into classically and alternatively activated macrophages and dendritic cells.* Biotechniques, 2016. **61**(1): p. 33-41.

136. Vorselen, D., et al., *Phagocytic 'teeth' and myosin-II 'jaw' power target constriction during phagocytosis.* Elife, 2021. **10**.
137. Bott, A.J., et al., *Glutamine Anabolism Plays a Critical Role in Pancreatic Cancer by Coupling Carbon and Nitrogen Metabolism.* Cell Rep, 2019. **29**(5): p. 1287-1298 e6.
138. Collins, S.L., et al., *mTORC1 Signaling Regulates Proinflammatory Macrophage Function and Metabolism.* J Immunol, 2021. **207**(3): p. 913-922.
139. Geeraerts, X., et al., *Macrophages are metabolically heterogeneous within the tumor microenvironment.* Cell Rep, 2021. **37**(13): p. 110171.
140. Sheldon, R.D., et al., *Interrogating in vivo T-cell metabolism in mice using stable isotope labeling metabolomics and rapid cell sorting.* Nat Protoc, 2021. **16**(9): p. 4494-4521.
141. Leone, R.D., et al., *Glutamine blockade induces divergent metabolic programs to overcome tumor immune evasion.* Science, 2019. **366**(6468): p. 1013-1021.
142. Mills, E.L., et al., *Succinate Dehydrogenase Supports Metabolic Repurposing of Mitochondria to Drive Inflammatory Macrophages.* Cell, 2016. **167**(2): p. 457-470 e13.
143. Yoo, H.C., et al., *Glutamine reliance in cell metabolism.* Exp Mol Med, 2020. **52**(9): p. 1496-1516.
144. Feng, Y., et al., *The Role of TAMs in Tumor Microenvironment and New Research Progress.* Stem Cells Int, 2022. **2022**: p. 5775696.
145. Ozbek, B., et al., *Multiplex immunohistochemical phenotyping of T cells in primary prostate cancer.* Prostate, 2022. **82**(6): p. 706-722.
146. Zarif, J.C., et al., *Mannose Receptor-positive Macrophage Infiltration Correlates with Prostate Cancer Onset and Metastatic Castration-resistant Disease.* Eur Urol Oncol, 2019. **2**(4): p. 429-436.
147. Mukha, A., et al., *GLS-driven glutamine catabolism contributes to prostate cancer radiosensitivity by regulating the redox state, stemness and ATG5-mediated autophagy.* Theranostics, 2021. **11**(16): p. 7844-7868.
148. Sfanos, K.S., et al., *Human prostate-infiltrating CD8+ T lymphocytes are oligoclonal and PD-1+.* Prostate, 2009. **69**(15): p. 1694-703.
149. Sarode, P., et al., *Reprogramming of tumor-associated macrophages by targeting beta-catenin/FOSL2/ARID5A signaling: A potential treatment of lung cancer.* Sci Adv, 2020. **6**(23): p. eaaz6105.
150. Li, J., et al., *Macrophage mitochondrial fission improves cancer cell phagocytosis induced by therapeutic antibodies and is impaired by glutamine competition.* Nat Cancer, 2022. **3**(4): p. 453-470.
151. Barger, S.R., et al., *Membrane-cytoskeletal crosstalk mediated by myosin-I regulates adhesion turnover during phagocytosis.* Nat Commun, 2019. **10**(1): p. 1249.
152. Reinfeld, B.I., et al., *Cell-programmed nutrient partitioning in the tumour microenvironment.* Nature, 2021. **593**(7858): p. 282-288.
153. Goswami, S., et al., *Myeloid cell-targeted therapies for solid tumours.* Nat Rev Immunol, 2023. **23**(2): p. 106-120.
154. Muller, A.J., et al., *Inhibiting IDO pathways to treat cancer: lessons from the ECHO-301 trial and beyond.* Semin Immunopathol, 2019. **41**(1): p. 41-48.
155. Alt, J., et al., *Glutamine Antagonist GA-607 Causes a Dramatic Accumulation of FGAR which can be used to Monitor Target Engagement.* Curr Drug Metab, 2021. **22**(9): p. 735-745.
156. Schcolnik-Cabrera, A., et al., *Pharmacological inhibition of tumor anabolism and host catabolism as a cancer therapy.* Sci Rep, 2021. **11**(1): p. 5222.
157. Kfoury, Y., et al., *Human prostate cancer bone metastases have an actionable immunosuppressive microenvironment.* Cancer Cell, 2021. **39**(11): p. 1464-1478 e8.
158. Hao, Y., et al., *Integrated analysis of multimodal single-cell data.* Cell, 2021. **184**(13): p. 3573-3587 e29.

159. Barkas, N., et al., *Joint analysis of heterogeneous single-cell RNA-seq dataset collections.* Nat Methods, 2019. **16**(8): p. 695-698.
160. Lemberg, K.M., et al., *The Novel Glutamine Antagonist Prodrug JHU395 Has Antitumor Activity in Malignant Peripheral Nerve Sheath Tumor.* Mol Cancer Ther, 2020. **19**(2): p. 397-408.
161. Kennedy, L.B. and A.K.S. Salama, *A review of cancer immunotherapy toxicity.* CA Cancer J Clin, 2020. **70**(2): p. 86-104.
162. Mahoney, K.M., P.D. Rennert, and G.J. Freeman, *Combination cancer immunotherapy and new immunomodulatory targets.* Nat Rev Drug Discov, 2015. **14**(8): p. 561-84.
163. Oldenborg, P.A., et al., *Role of CD47 as a marker of self on red blood cells.* Science, 2000. **288**(5473): p. 2051-4.
164. Cockram, T.O.J., et al., *The Phagocytic Code Regulating Phagocytosis of Mammalian Cells.* Front Immunol, 2021. **12**: p. 629979.
165. Feng, M., et al., *Phagocytosis checkpoints as new targets for cancer immunotherapy.* Nat Rev Cancer, 2019. **19**(10): p. 568-586.
166. Kharitonenkov, A., et al., *A family of proteins that inhibit signalling through tyrosine kinase receptors.* Nature, 1997. **386**(6621): p. 181-6.
167. Liu, Y., et al., *Emerging phagocytosis checkpoints in cancer immunotherapy.* Signal Transduct Target Ther, 2023. **8**(1): p. 104.
168. Majeti, R., et al., *CD47 is an adverse prognostic factor and therapeutic antibody target on human acute myeloid leukemia stem cells.* Cell, 2009. **138**(2): p. 286-99.
169. Brooke, G., et al., *Human lymphocytes interact directly with CD47 through a novel member of the signal regulatory protein (SIRP) family.* J Immunol, 2004. **173**(4): p. 2562-70.
170. Han, X., et al., *CD47, a ligand for the macrophage fusion receptor, participates in macrophage multinucleation.* J Biol Chem, 2000. **275**(48): p. 37984-92.
171. Dietrich, J., et al., *Cutting edge: signal-regulatory protein beta 1 is a DAP12-associated activating receptor expressed in myeloid cells.* J Immunol, 2000. **164**(1): p. 9-12.
172. Ghimire, K., et al., *CD47 Promotes Age-Associated Deterioration in Angiogenesis, Blood Flow and Glucose Homeostasis.* Cells, 2020. **9**(7).
173. Betancur, P.A., et al., *A CD47-associated super-enhancer links pro-inflammatory signalling to CD47 upregulation in breast cancer.* Nat Commun, 2017. **8**: p. 14802.
174. Carter, L., et al., *PD-1:PD-L inhibitory pathway affects both CD4(+) and CD8(+) T cells and is overcome by IL-2.* Eur J Immunol, 2002. **32**(3): p. 634-43.
175. Jia, L., Q. Zhang, and R. Zhang, *PD-1/PD-L1 pathway blockade works as an effective and practical therapy for cancer immunotherapy.* Cancer Biol Med, 2018. **15**(2): p. 116-123.
176. Gordon, S.R., et al., *PD-1 expression by tumour-associated macrophages inhibits phagocytosis and tumour immunity.* Nature, 2017. **545**(7655): p. 495-499.
177. Boussiotis, V.A., *Molecular and Biochemical Aspects of the PD-1 Checkpoint Pathway.* N Engl J Med, 2016. **375**(18): p. 1767-1778.
178. Yi, M., et al., *Regulation of PD-L1 expression in the tumor microenvironment.* J Hematol Oncol, 2021. **14**(1): p. 10.
179. La Gruta, N.L., et al., *Understanding the drivers of MHC restriction of T cell receptors.* Nat Rev Immunol, 2018. **18**(7): p. 467-478.
180. Barkal, A.A., et al., *Engagement of MHC class I by the inhibitory receptor LILRB1 suppresses macrophages and is a target of cancer immunotherapy.* Nat Immunol, 2018. **19**(1): p. 76-84.
181. Varghese, R., et al., *Comparative analysis of mammalian stanniocalcin genes.* Endocrinology, 1998. **139**(11): p. 4714-25.

182. Lin, H., et al., *Stanniocalcin 1 is a phagocytosis checkpoint driving tumor immune resistance.* Cancer Cell, 2021. **39**(4): p. 480-493 e6.
183. Freile, J.A., et al., *CD24 Is a Potential Immunotherapeutic Target for Mantle Cell Lymphoma.* Biomedicines, 2022. **10**(5).
184. Barkal, A.A., et al., *CD24 signalling through macrophage Siglec-10 is a target for cancer immunotherapy.* Nature, 2019. **572**(7769): p. 392-396.
185. Chao, M.P., et al., *Calreticulin is the dominant pro-phagocytic signal on multiple human cancers and is counterbalanced by CD47.* Sci Transl Med, 2010. **2**(63): p. 63ra94.
186. Basu, S., et al., *CD91 is a common receptor for heat shock proteins gp96, hsp90, hsp70, and calreticulin.* Immunity, 2001. **14**(3): p. 303-13.
187. Obeid, M., et al., *Calreticulin exposure dictates the immunogenicity of cancer cell death.* Nat Med, 2007. **13**(1): p. 54-61.
188. Feng, M., et al., *Programmed cell removal by calreticulin in tissue homeostasis and cancer.* Nat Commun, 2018. **9**(1): p. 3194.
189. Shachar, I., et al., *SLAMF receptors on normal and malignant B cells.* Clin Immunol, 2019. **204**: p. 23-30.
190. Chen, J., et al., *SLAMF7 is critical for phagocytosis of haematopoietic tumour cells via Mac-1 integrin.* Nature, 2017. **544**(7651): p. 493-497.
191. Ben Mkaddem, S., M. Benhamou, and R.C. Monteiro, *Understanding Fc Receptor Involvement in Inflammatory Diseases: From Mechanisms to New Therapeutic Tools.* Front Immunol, 2019. **10**: p. 811.
192. Bruhns, P., *Properties of mouse and human IgG receptors and their contribution to disease models.* Blood, 2012. **119**(24): p. 5640-9.
193. Zhang, M., et al., *Anti-CD47 Treatment Stimulates Phagocytosis of Glioblastoma by M1 and M2 Polarized Macrophages and Promotes M1 Polarized Macrophages In Vivo.* PLoS One, 2016. **11**(4): p. e0153550.
194. Weiskopf, K., et al., *CD47-blocking immunotherapies stimulate macrophage-mediated destruction of small-cell lung cancer.* J Clin Invest, 2016. **126**(7): p. 2610-20.
195. Zhang, H., et al., *HIF-1 regulates CD47 expression in breast cancer cells to promote evasion of phagocytosis and maintenance of cancer stem cells.* Proc Natl Acad Sci U S A, 2015. **112**(45): p. E6215-23.
196. Ring, N.G., et al., *Anti-SIRPalpha antibody immunotherapy enhances neutrophil and macrophage antitumor activity.* Proc Natl Acad Sci U S A, 2017. **114**(49): p. E10578-E10585.
197. Matlung, H.L., et al., *Neutrophils Kill Antibody-Opsonized Cancer Cells by Trogoptosis.* Cell Rep, 2018. **23**(13): p. 3946-3959 e6.
198. Huang, T., et al., *Thrombospondin-1 is a multifaceted player in tumor progression.* Oncotarget, 2017. **8**(48): p. 84546-84558.
199. Kamijo, H., et al., *Thrombospondin-1 promotes tumor progression in cutaneous T-cell lymphoma via CD47.* Leukemia, 2020. **34**(3): p. 845-856.
200. Nath, P.R., et al., *Natural Killer Cell Recruitment and Activation Are Regulated by CD47 Expression in the Tumor Microenvironment.* Cancer Immunol Res, 2019. **7**(9): p. 1547-1561.
201. Deuse, T., et al., *The SIRPalpha-CD47 immune checkpoint in NK cells.* J Exp Med, 2021. **218**(3).
202. Liu, X., et al., *CD47 blockade triggers T cell-mediated destruction of immunogenic tumors.* Nat Med, 2015. **21**(10): p. 1209-15.
203. Amy Chen, O.H., Abraham P Fong, Katherine L. Ruffner, Alison J. Forgie, Janet Sim, Sophia S Randolph, Hong Wan, Jaume Pons, Tracy C Kuo, *ALX148 Enhances the Depth and Durability of Response to Multiple AML Therapies.* Blood, 2020.

204. Li, T. and Z.J. Chen, *The cGAS-cGAMP-STING pathway connects DNA damage to inflammation, senescence, and cancer.* J Exp Med, 2018. **215**(5): p. 1287-1299.
205. Wu, L., et al., *Anti-CD47 treatment enhances anti-tumor T-cell immunity and improves immunosuppressive environment in head and neck squamous cell carcinoma.* Oncoimmunology, 2018. **7**(4): p. e1397248.
206. Gauttier, V., et al., *Selective SIRPalpha blockade reverses tumor T cell exclusion and overcomes cancer immunotherapy resistance.* J Clin Invest, 2020. **130**(11): p. 6109-6123.
207. Dizman, N. and E.I. Buchbinder, *Cancer Therapy Targeting CD47/SIRPalpha.* Cancers (Basel), 2021. **13**(24).
208. Veillette, A. and J. Chen, *SIRPalpha-CD47 Immune Checkpoint Blockade in Anticancer Therapy.* Trends Immunol, 2018. **39**(3): p. 173-184.
209. Krish Patel, M., Radhakrishnan Ramchandren, MD, Michael Maris, MD, Alexander M. Lesokhin, MD, Gottfried R. von Keudell, MD PhD, Bruce D. Cheson, MD, Jeff Zonder, MD, Erlene K. Seymour, MD, Tina Catalano, MSc, Gloria H. Y. Lin, PhD, Bob Uger, PhD, Penka S. Petrova, PhD, Kathleen Roberge, ANP, MSc, Yaping Shou, MDPhD, Swami P. Iyer, MD, *Investigational CD47-Blocker TTI-622 Shows Single-Agent Activity in Patients with Advanced Relapsed or Refractory Lymphoma: Update from the Ongoing First-in-Human Dose Escalation Study.* Blood, 2020.
210. Voets, E., et al., *Functional characterization of the selective pan-allele anti-SIRPalpha antibody ADU-1805 that blocks the SIRPalpha-CD47 innate immune checkpoint.* J Immunother Cancer, 2019. **7**(1): p. 340.
211. Liu, X., et al., *Dual Targeting of Innate and Adaptive Checkpoints on Tumor Cells Limits Immune Evasion.* Cell Rep, 2018. **24**(8): p. 2101-2111.
212. Nath, P.R., et al., *Loss of CD47 alters CD8+ T cell activation in vitro and immunodynamics in mice.* Oncoimmunology, 2022. **11**(1): p. 2111909.
213. Sockolosky, J.T., et al., *Durable antitumor responses to CD47 blockade require adaptive immune stimulation.* Proc Natl Acad Sci U S A, 2016. **113**(19): p. E2646-54.
214. Khandelwal, S., N. van Rooijen, and R.K. Saxena, *Reduced expression of CD47 during murine red blood cell (RBC) senescence and its role in RBC clearance from the circulation.* Transfusion, 2007. **47**(9): p. 1725-32.
215. Labadie, B.W., A.V. Balar, and J.J. Luke, *Immune Checkpoint Inhibitors for Genitourinary Cancers: Treatment Indications, Investigational Approaches and Biomarkers.* Cancers (Basel), 2021. **13**(21).
216. Martori, C., et al., *Macrophages as a Therapeutic Target in Metastatic Prostate Cancer: A Way to Overcome Immunotherapy Resistance?* Cancers (Basel), 2022. **14**(2).
217. Willingham, S.B., et al., *The CD47-signal regulatory protein alpha (SIRPa) interaction is a therapeutic target for human solid tumors.* Proc Natl Acad Sci U S A, 2012. **109**(17): p. 6662-7.
218. Morrissey, M.A., N. Kern, and R.D. Vale, *CD47 Ligation Repositions the Inhibitory Receptor SIRPA to Suppress Integrin Activation and Phagocytosis.* Immunity, 2020. **53**(2): p. 290-302 e6.
219. Yanagita, T., et al., *Anti-SIRPalpha antibodies as a potential new tool for cancer immunotherapy.* JCI Insight, 2017. **2**(1): p. e89140.
220. Tsao, L.C., et al., *CD47 blockade augmentation of trastuzumab antitumor efficacy dependent on antibody-dependent cellular phagocytosis.* JCI Insight, 2019. **4**(24).
221. Tseng, D., et al., *Anti-CD47 antibody-mediated phagocytosis of cancer by macrophages primes an effective antitumor T-cell response.* Proc Natl Acad Sci U S A, 2013. **110**(27): p. 11103-8.

222. Nonomura, N., et al., *Infiltration of tumour-associated macrophages in prostate biopsy specimens is predictive of disease progression after hormonal therapy for prostate cancer.* BJU Int, 2011. **107**(12): p. 1918-22.
223. Jiang, Z., et al., *Targeting CD47 for cancer immunotherapy.* J Hematol Oncol, 2021. **14**(1): p. 180.
224. Semiz, H.S., et al., *CD47 (don't eat me signal) expression levels and its relationship with clinicopathologic features in early-stage prostate carcinoma.* Prostate, 2022. **82**(16): p. 1564-1571.
225. Park, H.R., et al., *Blockade of CD47 enhances the antitumor effect of macrophages in renal cell carcinoma through trogocytosis.* Sci Rep, 2022. **12**(1): p. 12546.

Curriculum Vitae

MONALI PRAHARAJ, PhD, M.S.,
The Johns Hopkins University School of Medicine
Email: mprahar1@jhu.edu

EDUCATION HISTORY

Ph.D. expected 2018-23 Program in Pathobiology Johns Hopkins School of Medicine (JHMI)

Mentors: Jelani Zarif, PhD and Drew Pardoll, MD-PhD

M.S. 2016-18 Molecular Microbiology and Immunology Johns Hopkins School of Public

Health (JHSPH)

B.Tech. 2010-14 Biotechnology
Dr. DY Patil University

PROFESSIONAL EXPERIENCE

Rotation Student	**April 2019- Dec' 2019**	**Bishai Laboratory,** Tuberculosis research Center, JHMI
Rotation Student	**Dec' 2018- March 2019**	**Powell Laboratory,** Bloomberg Kimmel Institute for Cancer Immunotherapy, JHMI
Rotation Student	**Sept' 2018- Nov' 2018**	**Miller laboratory,** Department of Dermatology, JHMI
Graduate Certificate in Vaccine Science & Policy	**2016-18**	**Johns Hopkins School of Public Health**
Rotation Student	**Nov' 2016-Jan' 2017**	**Casadevall lab,** Fungal pathogenesis lab, JHSPH
Junior Research Assistant	**Nov' 2015-June 2016**	**MGM OMICS Research** Centre, Navi Mumbai, India
Project Technical Assistant	**March 2015-May 2015**	**Cell and Tissue Engineering lab,** IIT, India
Junior Research Fellow	**July 2014-January 2015**	**Genomics and Systems Biology** lab, IIT, Mumbai, India

SCHOLARSHIP, FELLOWSHIP OR EXTERNAL FUNDING

Thesis work funding and fellowship- NCI K22CA237623; Allegheny Health Network; Bloomberg Philanthropies

AWARDS

2022 **Excellence in Basic Research, Pathology Young Investigator's Day 2022.**
Johns Hopkins Pathology Dept

2022 **Doreen J. Putrah Cancer Research Foundation Scholar-in-Training Awardee**
American association of Cancer Research 22'

2019 **Awarded outstanding poster award 19'**
Annual Pathobiology graduate program retreat, JHMI

2016 **Qualified National Level Joint Graduate Entrance Examination**
National Centre for Biological Sciences, India

SERVICE AND LEADERSHIP ROLES

Vaccine Team member ESS editor, 2019 Novel Coronavirus Research Compendium, April 2020

- Helped the vaccine team rapidly curate emerging research on SARS-CoV-2 and COVID-19 to make research for public health action readily summarized and accessible

Teaching Assistant, Grant Writing, Department of Pathobiology, JHSOM
March-May 2021

- Graded PhD student written grants, organized and assisted speakers during the course and held TA hours to help students

Teaching Assistant, Basic Mechanism of Diseases, Department of Pathobiology, JHSOM
Aug'-Sept' 2019

- Held the introductory lecture on Respiratory Anatomy and Physiology and graded PhD student quizzes

Elected Forum Student Coordinator, MMI, JHSPH
Jan' 2017-May 2017

- Organized the student forum and coordinator with speakers and faculty evaluators for MMI department

PUBLICATIONS

- **Praharaj M**, Shen F, Zhao L, Nirschl T, Sena L, Singh A, Theodros D, Wang X, Williams R, Thompson E, Tam A, Yegnasubramanian S, Leone R, Al J, Rais R, Slusher B, Pardoll D, Powell J, Zarif J (2023). Glutamine blockade via prodrug JHU083 reprograms immunosuppressive tumor associated macrophages and myeloid cells and drives tumor immunity in urologic cancers. (*Manuscript in preparation*)
- Singh, A.K., Wang, R., Lombardo, K.A., **Praharaj, M**., Bullen, C.K., Um, P., Davis, S., Komm, O., Illei, P.B., Ordonez, A.A. and Bahr, M., 2022. Dynamic single-cell RNA sequencing reveals BCG vaccination curtails SARS-CoV-2 induced disease severity and lung inflammation. bioRxiv.
- Singh, A.K., **Praharaj, M.**, Lombardo, K.A., Yoshida, T., Matoso, A., Baras, A.S., Zhao, L., Srikrishna, G., Huang, J., Prasad, P. and Powell, J.D., 2022. Re-engineered BCG overexpressing cyclic di-AMP augments trained immunity and exhibits improved efficacy against bladder cancer. *Nature communications*, *13*(1), p.878.
- Liu, J., K. Lombardo, A. Singh, S. Karakus, **M. Praharaj**, A. Burnett, and T. Bivalacqua. "Tumor Necrosis Factor-α (TNF-α) and Rho-Associated Kinase 2 (ROCK2) Inhibitors Improve Erectile Function in a Bilateral Cavernous Nerve Injury Rat Model." The Journal of Sexual Medicine 19, no. 4 (2022): S25.
- Ruiz-Bedoya, C.A., Mota, F., Ordonez, A.A., Foss, C.A., Singh, A.K., **Praharaj, M.**, et al., 2021. 124I-Iodo-DPA-713 Positron Emission Tomography in a Hamster Model of SARS-CoV-2 Infection. *Molecular Imaging and Biology*, pp.1-9
- Choudhary, E., Bullen, C.K., Goel, R., Singh, A.K., **Praharaj, M**., Thakur, P., Dhiman, R., Bishai, W.R. and Agarwal, N., 2020. Relative and quantitative phosphoproteome analysis of macrophages in response to infection by virulent and avirulent mycobacteria reveals a distinct role of the cytosolic RNA Sensor RIG-I in Mycobacterium tuberculosis pathogenesis. Journal of proteome research, 19(6), pp.2316-2336.
- Dey, R.J. Dey, B., **Praharaj, M.,** Bishai, W. Bacillus Calmette-Guerin overexpressing an endogenous stimulator of interferon genes agonist provides enhanced protection against pulmonary tuberculosis. *J Infect Disease*. 2020 Mar 16; 221(7): 1049-1056.

POSTERS

- **Praharaj M**, Shen F, Nirschl T, et al 1119 Glutamine antagonist prodrug JHU083 reprograms immunosuppressive tumor-associated macrophages to drives tumor immunity in urologic cancers. Journal for Immunotherapy of Cancer. SITC 2022;10.
- **Praharaj, M.,** Shen, F., et al., 2022. Glutamine blockade via prodrug JHU083 reprograms immunosuppressive tumor associated macrophages (TAMs) and drives tumor immunity in urologic cancers. *Cancer Research*, *82*(12_Supplement), pp.2115-2115, AACR 2022
- Singh, A.K., Lombardo, K., **Praharaj, M.,** Liu, J., Becker, R., Harris, K., Kates, M., McConkey, D., Matoso, A., Bishai, W.R. and Bivalacqua, T.J., 2022. Varying Treatment outcomes of small molecule STING Agonist ADU-S100 in intratumoral and intravesical treatment regimens in syngeneic murine MB49 and in the N-methyl-N-nitrosourea (MNU) rat Model of urothelial carcinoma. Cancer Research, 82(12_Supplement), pp.3511-3511.
- Singh, A., **Praharaj, M.,** Lombardo, K., Zhao, L., Huang, J., Kates, M., McConkey, D., Bishai, W. and Bivalacqua, T., 2022. MP06-11 Magnitude Of Sting Signaling Determines Antitumor Outcomes, And Cd8+ T Cell Memory By BCG-Sting In Urothelial Tumors. The Journal of Urology, 207(Supplement 5), p.e81.
- Lombardo, K., **Praharaj, M.**, Matoso, A., Bishai, W., Bivalacqua, T. and Singh, A., 2022. 1385 Divergent therapeutic outcomes of STING agonist ADU-S100 in intratumoral and intravesical treatment regimens in syngeneic murine MB49 and in the N-methyl-N-nitrosourea (MNU) rat model of urothelial carcinoma.
- Singh, A.K., **Praharaj, M**., Lombardo, K.A., Yoshida, T., Matoso, A., Baras, A.S., Zhao, L., Prasad, P., Srikrishna, G., Powell, J.D. and Kates, M., 2020, December. Recombinant BCG overexpressing STING agonist elicits trained immunity and improved antitumor efficacy in non-muscle invasive bladder cancer. In Urologic Oncology: Seminars and Original Investigations (Vol. 38, No. 12, p. 899). Elsevier.
- **Monali Praharaj**, Alok Kumar Singh, William Bishai. STING Agonist Overexpressing Bacillus Calmette-Guerin (BCG), a Potent Inducer of Trained Immunity in Human Monocytes. Annual Pathobiology Retreat. Johns Hopkins School of Medicine. Sept 2019. Baltimore, MD

PATENT

- Recombinant therapeutic interventions for cancer. US16/638,943. JHU Internal number P14295. Priority date April 17, 2018. https://patents.google.com/patent/US20210024940A1/ Continuation in Part to US16/638,943. Submitted Feb 13, 2020. JHU Internal number P14295-CIP.